UNIVERSIDADE TÉCNICA DE LISBOA

INSTITUTO SUPERIOR TÉCNICO

Conversion and Operation of CAST as a massive axion detector

Nuno Alexandre Rio Duarte Elias
(Licenciado)

Dissertação para obtenção do Grau de Doutor
em Engenharia Física Tecnológica

Orientador:	Doutor Tapio Olavi Niinikoski
Co-Orientador:	Doutora Maria Paula Frazão Bordalo e Sá

Júri

Presidente:	Presidente do Conselho Científico do IST
Vogais:	Doutor Tapio Olavi Niinikoski
	Doutor Martyn Davenport
	Doutor João Manuel Coelho dos Santos Varela
	Doutora Maria Paula Frazão Bordalo e Sá
	Doutor Sérgio Eduardo de Campos Costa Ramos

Março 2010

Resumo

O axião foi postulado a partir de uma solução elegante proposta por R. Peccei e H. Quinn para resolver o problema CP forte da Cromodinâmica Quântica.

A experiência CAST investiga a existência de axiões produzidos no núcleo do Sol, usando um íman supercondutor, protótipo do LHC, para espoletar a sua conversão em raios-X detectáveis.

Durante a sua primeira fase, com a região sob campo magnético mantida em vácuo, CAST examinou com alta sensibilidade massas do axião até 0.02 eV/c^2, acima do qual a coerência na conversão é perdida.

Esta tese reflecte o trabalho que permite à experiência CAST estender a sua pesquisa até massas de 1 eV/c^2. A coerência perdida é restaurada inserido gás dentro dos tubos do íman, permitindo ao fotão emergente da conversão adquirir uma massa efectiva. A massa do axião pode então ser rastreada ajustando de uma forma precisa a densidade do gás.

A conversão da experiência exigiu um estudo aprofundado, seguido da concepção e construção de um sistema para lidar com um isótopo de hélio extremamente raro, o ^3He. Este representa um importante desafio tecnológico e uma importante vantagem, permitindo à experiência CAST estender a sua pesquisa a um novo e inexplorado território proposto pelos modelos teóricos.

Palavras-chave: CAST, axião, ^4He, ^3He, sistema de gás.

Abstract

The axion was postulated after an elegant solution proposed by R. Peccei and H. Quinn to solve the strong CP problem of Quantum Chromodynamics.

The CAST experiment searches for axions created in the core of the Sun. It uses an LHC superconducting prototype magnet to trigger the axion conversion into detectable X-ray photons.

During its First Phase, with the magnetic field region kept under vacuum, CAST searched with high sensitivity for axion masses up to 0.02 eV/c^2, for higher values the conversion coherence is lost.

This thesis reflects the work that allows CAST to extend its search up to axion masses of 1 eV/c^2. To restore the lost coherence a buffer gas is introduced in the magnet cold bores, such that the photon arising from the Primakoff conversion acquires an effective mass. The axion mass can be effectively scanned by fine tuning the gas density.

The conversion of the experiment required the study, design and construction of a complex gas handling system to deal with a rare helium isotope, ^3He. It represents an important technological challenge and a major advantage, allowing the CAST experiment to extend its search into a new unexplored territory that is favoured by theoretical models.

Keywords: CAST, Axion, ^4He, ^3He, gas system.

Acknowledgments

The work in this thesis would not have been possible without the contribution of several exceptional people to whom I would like to express my great gratitude.

When I decided to embark in this adventure, I contacted Doctor Tapio Niinikoski, his renowned experience and enviable research subjects, matched with my motivation. Thank you for your great supervision and guidance.

On the Portuguese side, Prof. Doctor Paula Bordalo answered my request and from day one showed great compassion and sympathy throughout her supervision. Thank you, for making me understand the difficulties of the sometimes very complex, Portuguese system.

The CAST experiment is settled in very strong foundations: Prof. Konstantin Zioutas and Dr. Martyn Davenport are two charismatic people to whom I need to express my most profound gratitude. Thank you for driving the experiment forward and thank you for all the choices you gave me. The time we spent together awakes great memories and profound feelings.

My sincere thanks to Prof. Doctor Sérgio Ramos, for his great help, which became an essential piece.

My great gratitude goes to the people in the Cryolab: Laetitia, AgosTino, Laurent, Sebastien, Jean-Louis and Gaelle, for making all the technicalities look easy, and also to Marco, Adam and Alexandre, for making me become a fan of controls & operations.

Great help was provided by J-M Bojon and J-M Laurent for their vacuum expertise and Laura for all the help provided in the area, thank you for your hard work.

This work would not have been possible without the CERN Doctoral Studentship with all necessary means for carrying out my research and to LIP for taking me as one of their own.

I made great friends in this journey, Thomas, Jaime, Julia, Biljana, Theodoros, Annika, Berkol, Georgios, Javier, Serkant, Silvia, Igor, Theopisti and all other CASTers, without you it would have been only for the love of Science. Thank you also, Giulia and Peder for your friendship and great moments spent together.

To my family for being always with me.

To Helena, for her affection.

Table of Contents

1 Introduction

The Standard Model (SM) of particle physics remains so far the most well accepted theory for being able to provide solutions to most of the questions. It is unable, however, to solve the so-called strong CP-problem of Quantum Chromodynamics (QCD). In QCD, the SM theory for strong interactions, it is expected the strong force to break the Charge conjugation and Parity transformation (CP-symmetry), however this feature has not yet been observed.

One plausible solution for the strong CP-problem was formulated by the renowned physicists Roberto Peccei and Helen Quinn in the year 1977. With their novel approach, they consistently managed to understand the supposed CP conservation by introducing an extra symmetry, the Peccei Quinn (PQ) symmetry.

When the new PQ-symmetry is spontaneously broken, for a scale f_a, a new particle should arise as shown by Frank Wilczek and Steven Weinberg, thus relaxing the CP violation parameter to zero. This new particle would be a Nambu-Goldstone boson, a light and neutral pseudo-scalar particle for which was given the name *axion*.

The axion, due to its expected properties, could have played an important role in the history of the Universe. If they exist, they may have been produced shortly after the Big Bang and could contribute significantly to the cold dark matter of the Universe, or else could be created in the core of stars up to the present time.

The interest in axions has become remarkable. Various constrains have been derived from astrophysics and cosmology thus limiting the parameter space for axions. More importantly a growing number of direct laboratory experiments have attempted to discover or constrain its existence even further.

The race is on, with various experiments looking at different or overlapping regions of the axion parameter space. Most of these are using the Primakoff effect, expecting axions to convert into detectable photons in the presence of a strong transverse magnetic field. CAST at CERN is one of these, and it is the most sensitive of those using this concept. Such an apparatus, called 'helioscope', is also operated by a team of the Tokyo University.

The CERN Solar Axion Telescope (CAST) is looking at hypothetical axions coming from our closest available celestial source, the Sun. In the hot and dense plasma in the core of the Sun, the best conditions for the production of axions can be found. Here, a photon produced in the solar core might couple through Primakoff effect with the virtual photon of the enormous electromagnetic fields of the solar plasma, giving origin to an axion. This axion would reach the surface of the Earth and be converted into a detectable X-ray photon inside the strong transverse magnetic field of CAST.

The CAST experiment uses a decommissioned prototype magnet from the LHC to trigger the axion conversion into X-ray photons. This twin aperture superconducting dipole magnet operates at a temperature of 1.8 K and provides a magnetic field of 9 T over a length of 9.26 m in its two cold bore tubes.

The magnet is pointed to the Sun for two periods in the day, around the Sunrise and the Sunset, lasting a total of 3 hours. The converted X-ray photons can be detected by sensitive X-ray detectors placed at the two ends of the magnet, terminated by the Magnet Return Box (MRB) and the Magnet Feed box (MFB).

Installed on the MRB side, a conventional Time Projection Chamber (TPC) searches for the axion signature during the Sunset tracking, this detector covers both of the magnet apertures.

On the opposite MFB side, are placed two separate detectors searching for axion conversion during the Sunrise tracking. Each of them cover one aperture. One of these is a MICROMEsh Gaseous Structure (MICROMEGAS), while the second is an X-ray telescope, consisting of an X-ray focusing optics with a Charge Coupled Device (CCD).

In the Primakoff effect, the probability of converting an axion to a photon in the static transverse field depends on maintaining the phase coherence between the axion and a virtual photon during their travel through the high-field region in vacuum. A massless axion travels at the speed of light, and therefore keeps perfectly in step with the virtual photon, which leads to a maximum probability.

For a massive axion having an energy in the range from 2 keV to about 8 keV, the mass must lie below 0.02 eV/c^2 in order to maintain the phase coherence. In its Phase I operation featuring vacuum in the conversion region, CAST was therefore sensitive only to axions whose masses lie below 0.02 eV/c^2, above which the sensitivity degrades rapidly.

In order to extend the mass reach of the experiment, buffer gas must be introduced in the conversion region. The propagation velocity of the photon is slowed down due to the index of refraction of this medium. The gas density can be adjusted so that the velocities match and the phase coherence is maintained for axions in a well controlled mass interval. By scanning the buffer gas density, a range of masses can be thus scanned above 0.02 eV/c^2. This is the technique used in CAST Phase II operation with helium as buffer gas.

Since the magnet operates at 1.8 K, cooled by superfluid helium, the two stable isotopes of helium can be used. The natural isotope of helium ^{4}He was used up to its saturation pressure of 16.4 mbar allowing a possible search up to 0.4 eV/c^2.

To go even further, one has to operate with ^{3}He, an artificially produced and expensive lighter isotope of helium. It has a higher saturation pressure of 135.6 mbar which allows a possible extension of the sensitivity up to masses of 1.2 eV/c^2, thus closing the window up to the cosmological limit.

The First Phase of CAST, with two successful years of data taking in 2003 and 2004, resulted in an upper limit on the axion-to-photon coupling of $g_{a\gamma} = 8.8\times10^{-11}$ GeV^{-1} (95 % C.L) for axion masses below 0.02 eV.

In order to embark in the Second Phase of the experiment, important studies and experimental changes have to be carried out, thus representing an important technological challenge and effort.

This thesis is devoted to the audacity of converting the CAST experiment into its Second Phase, by designing and constructing the buffer gas handling system which allows the experiment to enter territory without precedents in the axion search community.

In Section 2 we focus in the CAST experiment, starting with the axion production in the Sun and the existing experimental setup and its results.

Following this, in Section 3 attention is presented the necessity of a having buffer gas as an axion conversion medium in order to extend the search to massive axions. Here we introduce physics requirements on the buffer gas density and study possible constraints.

Section 4 describes the most important design constraints together with a discussion on possible solutions and some results.

In Section 5 the concept for the provisional ^{4}He gas system is presented together with the results of the physics runs that lasted throughout the years 2005 and 2006.

The final ^{3}He gas system is described in detail in Section 6, where the solutions for integration with the existing CAST setup are presented together with its installation. Moreover, importance is given to the control and supervision of the system, where solutions were found to meet with the important complexity.

Finally in Section 7 will conclude the work and summarize the results.

2 The Axion and CAST

Axions can be produced in the core of stars, such as our Sun. Helioscopes such as the CERN Axion Solar Telescope (CAST) use the Sun as the source of axions with the goal to discover or set limits on the existence of this, so far, hypothetical particle.

In this section we discuss the main parameters for the axion production and possible detection within CAST. It is introduced the main constituents of the CERN Axion Solar Telescope experiment.

The experimental setup was designed to detect and study axions created in the core of the Sun, to make that a reality a powerful magnet is kept aligned with the Sun during long periods and, when the coherence condition is satisfied, the incoming axion is expected to convert into an X-ray photon. To efficiently detect the resulting photons, different X-ray detectors are positioned at the extremities of the magnet.

The CAST experiment which is located at the LHC[1] Point 8 of CERN[2] is a Helioscope type experiment, meaning that the axion-to-photon conversion by Primakoff effect is done by aligning a strong transverse magnetic field with the source of axions, in this case the Sun.

CAST uses a decommissioned LHC prototype A1 superconducting dipole magnet, which is kept aligned with the Sun during two periods of the day, the Sunrise and the Sunset, by means of a tracking system.

The magnet with a length of 9.26 m and a nominal field of 9 T is cooled by a dedicated cryogenics plant (more details in section 2.4) that keeps the magnet at the nominal operating temperature of 1.8 K. The magnet is traversed by two parallel straight bores (axion conversion region) with a cross sectional area A=14.5 cm^2.

In order to upgrade CAST for the search of massive axions (Second Phase) the axion conversion region (filled with buffer gas) has to be separated from the detectors (under vacuum) by means of high transmission thin cold windows, allowing the converted photon to reach the detectors, but also ensuring a stable confinement of the buffer gas for a given pressure.

To collect the resulting photons and to maximize the discovery potential, optimized low-background detectors tuned for the interesting X-ray range are mounted at each extremity of the magnet.

[1] - Large Hadron Collider, a 27 km particle accelerator, located 100 m underground, which will produce head on collisions of protons up to energies of 14 TeV. /public.web.cern.ch/Public/en/LHC/LHC-en.html

[2] - Conseil Europeen pour la Recherche Nucleaire is the European Organisation for Nuclear Research, one of the world's largest and most respected centers for scientific research. /www.cern.ch

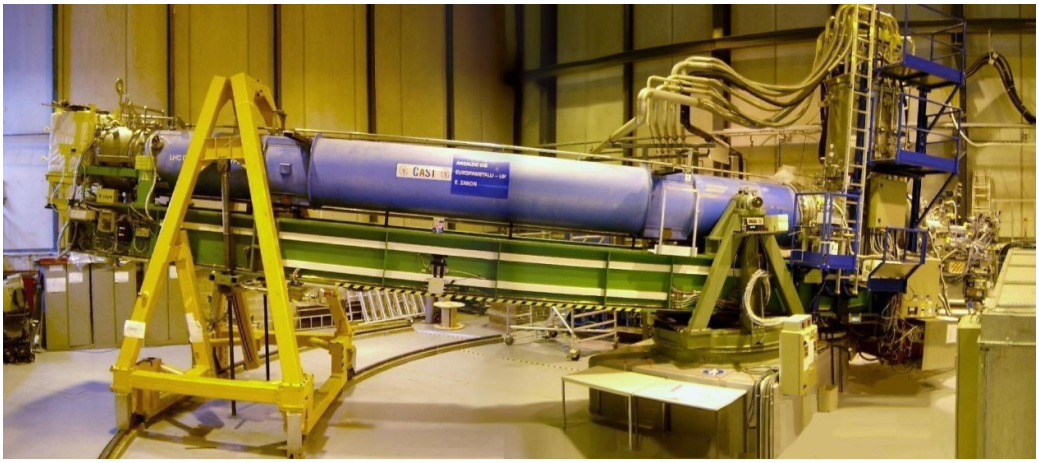

Figure 2-1: Experimental setup of the CERN Axion Solar Telescope. The magnet placed inside the cryostat (blue) is installed on top of the supporting structure (green), which is supported on the right hand side by a pivoting turntable (olive green) allowing horizontal movement. On the other extremity the magnet is carried by two lifting screws on a girder (yellow), which allows for the vertical movement. The yellow girder travels on top of circular rails visible on the floor of the experimental hall enabling the magnet to perform a horizontal rotation. The combination of the vertical and horizontal movement results in a tracking motion, allowing the magnet to be aligned with the Sun's trajectory. The axion conversion into photons is due to occur inside the magnet cold bores and the resulting photons can therefore be detected by sensitive detectors placed at each extremity of the magnet. A cryogenics plant is responsible for keeping the magnet at the nominal operating temperature. The cryogenics flexible lines and electrical cables for powering the magnet are visible on the right side of the picture

2.1 The Sun as a source of Axions

The mechanism for production of axions, assumes that axions can be produced in the core of stars due to fluctuating electrical fields due to charged particles in the plasma. The Primakoff mechanism [1][2] (in Appendix A an overview of general axion physics is given), shown in Figure 2-2, foresees the conversion of blackbody photons in the fluctuating electrical fields into axions, $\gamma + Z_e \rightarrow Z_e + a$.

Figure 2-2: The Primakoff mechanism in the Sun (left) and the inverse process in a laboratory transverse magnetic field (right).

The Solar Model

For experimental purposes, the flux of axions reaching the Earth has to be taken in consideration and thus the flux of produced axions in the Sun has to be evaluated.

The transition rate of a photon of energy ω into an axion can be given by the following formula derived in [3], assuming non-relativistic plasma and integrating over all possible species of targets and over all angles, we get:

$$\Gamma_{\gamma\to a} = \frac{g_{a\gamma}^2 T_\odot \kappa_s^2}{32\pi}\cdot\frac{k}{\omega}\cdot\left\{\begin{array}{l}\dfrac{[(k+p)^2+\kappa_s^2][(k-p)^2+\kappa_s^2]}{4kp\kappa_s^2}\cdot \\ \cdot ln\left[\dfrac{(k+p)^2+\kappa_s^2}{(k-p)^2+\kappa_s^2}\right]-\dfrac{\left(k^2-p^2\right)^2}{4kp\kappa_s^2}\cdot ln\left[\dfrac{(k+p)^2}{(k-p)^2}\right]-1\end{array}\right\}. \quad (2.1)$$

Here $g_{a\gamma}$ is the axion to photon coupling constant, k and ω are the momentum and energy of the photon, p the axion momentum, $T_\odot$ is the plasma temperature of the Sun and κ_s the Debye-Huckel scale for the screening effects given by:

$$\kappa_s^2 = \frac{4\pi a}{T_\odot}\sum_j Z_j^2 N_j. \quad (2.2)$$

Being a the fine structure constant, N_j the number density of charged particles which are carrying the charge $Z_j e$.

The energy of the axion and photon are practically the same. The plasma frequency in the Sun (~0.3 keV) is small when compared to the photon energies, typically $3T_\odot \simeq 4\ \text{keV}$. Making $k = E_a$ and $p = \sqrt{E_a^2 - m_a^2}$, with E_a the axion energy and m_a the axion mass, the equation (2.1) becomes:

$$\Gamma_{\gamma\to a} = \frac{g_{a\gamma}^2 T_\odot \kappa_s^2}{32\pi} \cdot \left\{ \begin{array}{l} \dfrac{\left(m_a^2 - \kappa_s^2\right)^2 + 4E_a^2\kappa_s^2}{4pE_a\kappa_s^2} \cdot \\ \cdot ln\left[\dfrac{(E_a+p)^2+\kappa_s^2}{(E_a-p)^2+\kappa_s^2}\right] - \dfrac{m_a^4}{4pE_a\kappa_s^2} \cdot ln\left[\dfrac{(E_a+p)^2}{(E_a-p)^2}\right] - 1 \end{array} \right\}. \qquad (2.3)$$

To define the differential flux of axions arriving at Earth it is necessary to include in the transition rate the blackbody photon distribution of the Sun and integrate over a standard solar model as described by Bahcall et al.[4] and recently in BP2004 [5]. An approximated analytical formula has been derived by K.V Bibber et al.[6], and using the reviewed model becomes:

$$\frac{d\Phi(E_a)}{dE_a} = 6.02 \cdot 10^{10} \left(\frac{g_{a\gamma}}{10^{-10}\,\text{GeV}^{-1}}\right)^2 \frac{\left(E_a/\text{keV}\right)^{2.481}}{e^{E_a/1.205\text{keV}}} \left[\text{cm}^{-2}\text{s}^{-1}\text{keV}^{-1}\right]. \qquad (2.4)$$

The differential axion flux is plotted in Figure 2-3. It shows that a maximum flux is expected for an axion energy of ~3.0 keV and the average axion energy is 4.2 keV.

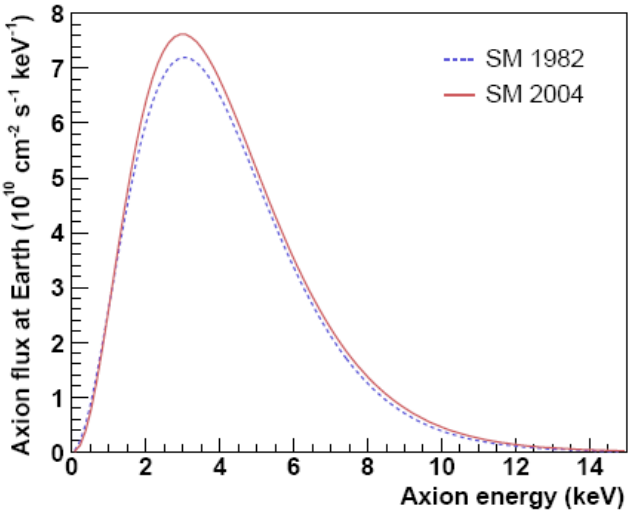

Figure 2-3: The differential axion flux with origin on the Sun at Earth. Standard Solar model in dashed blue and updated model in red. Figure courtesy of D. Kang.

The axion surface luminosity, updated using the modern solar model BP2004 gives the position dependence, on the solar disk, from where axions are expected to emerge [7]. On Figure 2-4 it is shown a graphical representation of the axion surface luminosity of the solar disk as a function of the radial coordinate $R / R_{\odot}$ and the axion energy. It is notorious that most of the expected axions come from the solar core (more than 80% of the total flux are expected to emerge from the central $0.2\, R_{\odot}$).

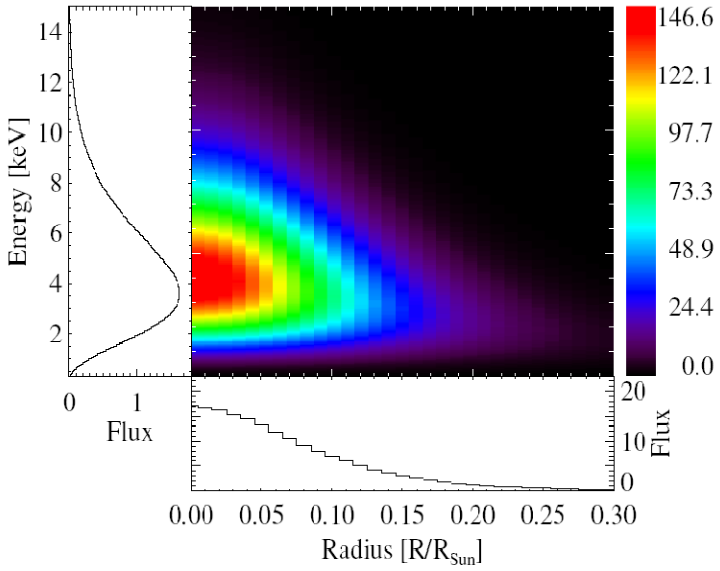

Figure 2-4 Graphical representation of the axion surface luminosity of the solar disk as a function of the axion energy and the radial coordinate of the solar disk. (Units are in $\left[\mathrm{cm}^{-2}\mathrm{s}^{-1}\mathrm{keV}^{-1}\right]$ per unit surface of the solar disk) [7].

Axion conversion in a magnetic field

In an axion Helioscope such as the CAST experiment, the reverse Primakoff mechanism can take place (see Figure 2-2). In the presence of a magnetic field, the incoming axion converts into a real photon by coupling with the virtual photon, the magnetic field should be transverse to the axion wave in order to match the axion spin (spin = 0), with the resulting photon (spin=1).

$$a + \gamma_{virtual} \leftrightarrow \gamma \tag{2.5}$$

The conversion can occur at any point of the field provided that the coherence condition is satisfied, that is to say that both axion and photon fields should be in phase over the full length of the magnetic field, for constructive interference to occur. The axion conversion probability having the conversion region under vacuum becomes [8]:

$$P_{a\to\gamma} = \left(\frac{B \cdot g_{a\gamma}}{q} \right)^2 \cdot \sin^2 (qL). \tag{2.6}$$

Here B is the magnetic field, L is the magnet length and q is the momentum transfer between the axion and the X-ray photon calculated as follows:

$$q = \frac{m_a^2}{2E_a}. \tag{2.7}$$

In order to maximize the axion conversion probability the coherence condition should be satisfied by having:

$$qL < \pi. \tag{2.8}$$

In a laboratory setup with the same characteristics as the CAST magnet, and considering the axion spectrum given by Equation 2.4 the coherence condition is satisfied only up to axion masses lower than 0.02 eV, when the magnet cold bores are under vacuum.

The CAST experiment has taken data in the years 2002 to 2004 with vacuum in the magnet bores (usually referred as First Phase of the experiment), and as demonstrated above, the axion mass search is limited by the fulfilment of the coherence condition stated above.

To extend the axion search for massive axions and overcome the physical constraint due to loss of coherence, a method proposed by K.V.Bibber will be explained in Section 3.

The expected number of converted photons N_γ, hitting the detector with an effective area S, over an observation time t can be calculated as following:

$$N_\gamma = \Phi_a \times P_{a\to\gamma} \times S \times t \propto g_{a\gamma}^4. \tag{2.9}$$

The CAST experiment wishes to cover the maximum available axion mass range in two different phases:

The First Phase, which finished in the end of 2004, where physics runs were taken with the magnet cold bores under vacuum, with this setup CAST was able to provide an upper limit of $g_{a\gamma} < 8.8 \cdot 10^{-11} \mathrm{GeV}^{-1}$ at 95% CL for axion masses up to 0.02 eV [9].

The Second Phase, covered by this thesis, supposes filling of the magnet cold bores with a buffer gas, allowing the sensitivity of the experiment to be extended up to much higher masses when compared with the previous phase. Further discussion will be given in the following sections.

2.2 The Magnet and the Cryogenics system

One of the key equipments in the CAST experiment is the superconducting magnet responsible for providing the necessary transverse magnetic field for the axion conversion. The magnet was originally built as a test prototype for the Large Hadron Collider and was adapted for CAST purposes [10].

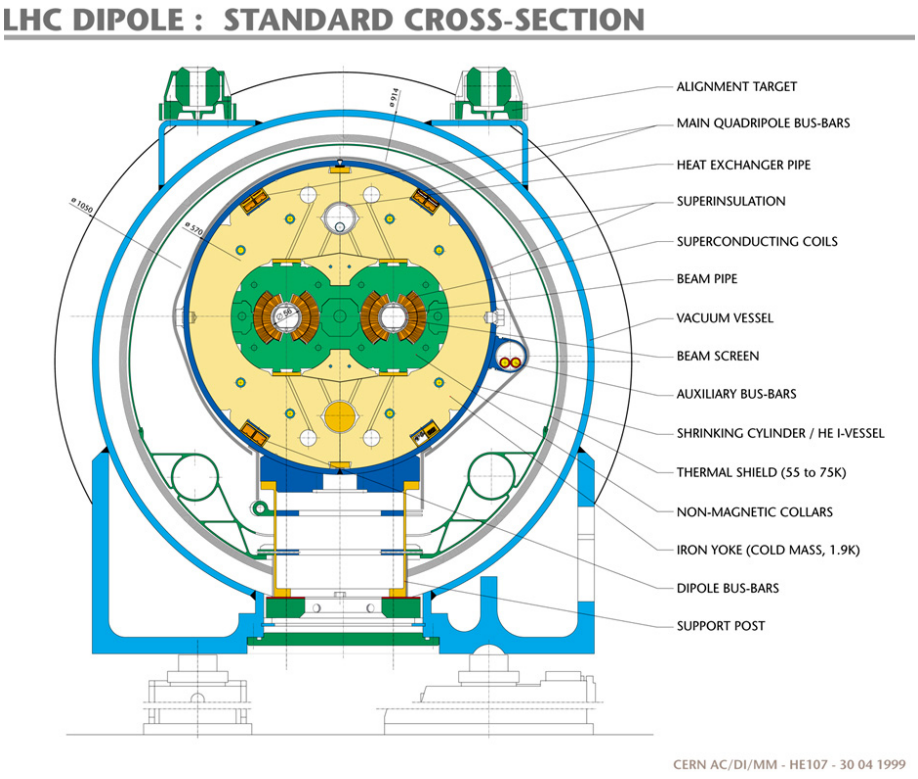

Figure 2-5: Cross section of a twin-aperture dipole superconducting magnet

The twin aperture superconducting dipole magnet is traversed by two parallel cold bores with an aperture of 43 mm diameter each, which are positioned 180 mm apart, inside a collaring structure embedded in the cold mass.

The superconducting wires made of Niobium-Titanium (Nb-Ti) have to be supplied with a current of 13300 A to produce a nominal field of 9 T over a length of 9.26 m. Figure 2-5 shows the magnet cross section and the main elements. The magnet is positioned inside a vacuum vessel (cryostat) and the heat loss by radiation is minimized using thermal radiation shield and multi layer insulation.

The cryostat is mounted on top of a mechanical structure that allows rotation on both horizontal and vertical planes. This is an essential mechanism for the alignment of the cold bores to follow the Sun trajectory during solar tracking.

2.3 The Detectors

In order to detect the converted X-ray photons, the CAST experiment uses several low-background detectors using different detection techniques for an optimized energy range between 1 and 10 keV.

The detectors are positioned at each extremity of the magnet. Depending on their location, the detectors will only collect X-ray photons from axions, either during Sunrise or Sunset.

To detect the axions converted during the Sunset, a Time Projection Chamber (TPC) covers both cold bore apertures (V1 and V2). On the other extremity, one of the cold bores apertures (V2) is covered by a Micro-mesh Gaseous Structure detector (Micromegas) and the remaining aperture (V1) is covered by a Charged Coupled Device (CCD) having in front an X-ray focusing optics to enhance the signal to noise ratio in the sensitive region.

During the period when the magnet is aligned with the Sun (that lasts 1.5 hours, for both the sunrise and sunset) the corresponding detector placed downstream of the conversion region is taking data, which adds up to 1.5 hours tracking time for each detector. The remaining time of the day is dedicated to all detectors to take background data and to perform calibrations.

The Time Projection Chamber

The TPC detector [11] is located at the eastern end of the CAST magnet, also defined as the MRB side (Magnet Return Box). It covers both magnet bores and is expected to collect the resulting photons after conversion during the Sunset solar tracking.

The design of this detector follows a well established and experimental proven concept of a conventional TPC, being constituted of a large volume filled with an ionizing gas where primary interactions takes place, which develop ionization electrons that drift towards a plane of wires, here the signal is amplified in an avalanche process, allowing a position sensitivity of the original event.

The detector volume consists of a chamber made of plexiglass with dimensions $10\times30\times10$ cm^3 (x,y,z directions being z parallel to the magnet axis). This chamber is filled with a gas mixture of 95% Argon (Ar) and 5% Methane (CH_4) maintained at atmospheric pressure.

The conversion efficiency for photons up to 6 keV is better than 99%, and decreases for higher energies becoming 50% for 11.5 keV. To prevent the contamination from atmospheric impurities, the gas continuously flows with a rate of 2 l/h.

The drift anode composed of a continuous aluminium layer is located at the front of the detector close to the magnet and is maintained at -7 kV, it has two apertures of 6 cm radius for the placement of warm windows transparent to X-ray that are able to hold 1 atm pressure difference, and aligned with both apertures of the magnet cold bores.

These windows are made of a thin aluminized mylar foil (3 μm or 5 μm) that is stretched and glued onto a metallic grid. The grid itself has a geometric transmission of 92% and the foil about 95% for X-rays with energies higher than 3 keV and decreases to lower energies. The inner side of the foil, coated with 40 nm aluminium also works as drift anode. The drift anode is separated from the sense wires of a maximum distance of 10 cm.

On the back of the chamber, the sense wires are organized in 3 planes: Two grounded planes of cathode wires perpendicular to the wider side of the chamber, containing 96 wires of 100 μm diameter each; One anode plane of wires at +1.8 kV, containing 48 wires of 20 μm diameter is positioned in the middle of the two cathode planes and parallel to the wider side of the chamber. The distance between the wires is 3 mm and the distance between the first two planes closest to the drift region is 3 mm,

and for the other two planes 6 mm. A representation of the detector is shown in Figure 2-6.

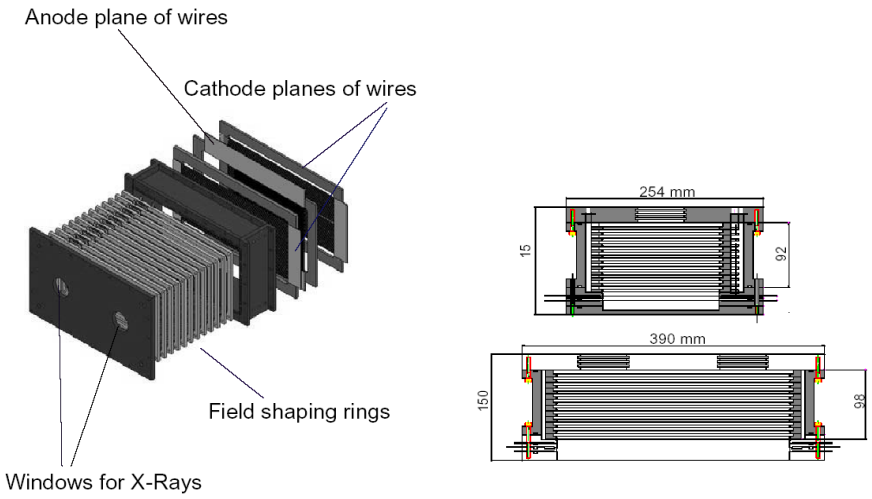

Figure 2-6: View of the TPC detector, in the exploded representation of the left, the different planes of anodes, cathodes and the field shaping rings are clearly visible. It is also possible to identify the two apertures where the circular windows are placed. On the right the top and side views are shown with and the main dimensions.

The avalanche process occurs close to the anode plane, due to the high electric field collecting the electrons, while the ions are gathered by the cathode planes. The anode and cathode planes are arranged in a perpendicular way which allows the determination of the spatial position of the event.

The TPC is positioned in the far end from the pivot point which allows the magnet rotation and thus makes long spatial translations during solar tracking.

In order to reduce the general level of background, but also to homogenize the position dependence within the experimental hall, several layers of material enclose the detector chamber (from inside to outside): copper (5 mm), lead (25 mm), cadmium (1 mm), polyethylene (225 mm) and a PVC bag allows pure nitrogen gas to flush the interior. On top of the shielding was placed a scintillating veto to reduce muon-induced events by anti-coincidence with the detector.

The gain of the detector is measured using a ^{55}Fe source and the pedestal levels and the variation of the flash-ADCs channels are measured using artificial trigger signals in the absence of real events. Every 6 hours a pedestal run and two calibration runs are

taken, by moving the calibration source from its normal parking position into the centre of the acceptance area of each window.

The MicroMeGaS Detector

The Micro-Mesh Gaseous Structure detector (MM) [12] is mounted on the west end of the magnet, also defined as MFB (Magnet Feed Box) and covers only one of the two cold bores apertures (V2), it is expected to collect the resulting photons after conversion during the Sunrise solar tracking.

The MM principle is similar to that of the TPC, but with a particular difference that it does not include a plane of wires, instead it includes a micro mesh to separate the two regions (conversion and amplification).

After passing through a vacuum buffer space, the incoming X-ray photon enters the conversion region filled with a flammable gas mixture of Argon (95%) and Isobutane (5%). Due to the applied electrical field, here it generates a photoelectron by photoelectric effect. The Figure 2-7 presents a scheme of the detector.

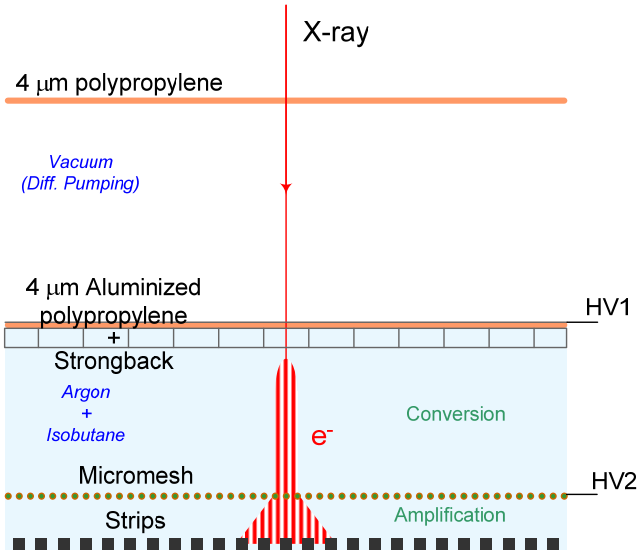

Figure 2-7: Schematic view of the Micromegas detector, the detector volume is enclosed by the X-ray warm window and the strips at the at the back of the detector, and is separated in two regions (conversion and amplification) by the micromesh.

The photoelectron travels a distance of 30 mm, between the aluminized warm window and the micromesh creating ionization electrons, the electrons drift in a electrical field of ~250 V/cm, until they are obliged to pass through small holes in the micromesh into the amplification region of only 50 μm deep, here the electrical field increases dramatically up to ~ 40 kV/cm which causes an avalanche, producing a electron cluster that is collected on the $x-y$ strips.

The MM detector frame is made of Plexiglas, having the electrodes attached to it. The micromesh is made of copper and has a thickness of 5 μm, it is perforated by 25 μm diameter holes in a staggered arrangement 50 μm apart. The readout consists in two sets of 192 strips arranged perpendicularly. Figure 2-8 shows a 3D representation of the various constituents of the detector.

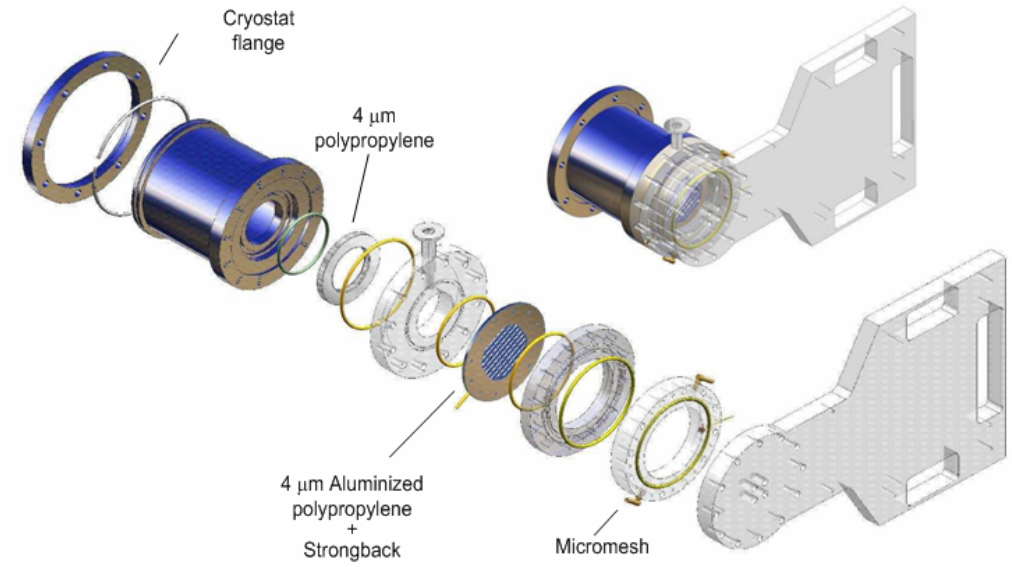

Figure 2-8: Exploded view of the MM detector. On blue is represented the interface with the existing flange on the magnet cryostat. The various components are clearly visible. On top right corner is represented the MM fully closed.

In front of the detector there is a volume defined by two high transmission X-ray windows with a thickness of 4μm (one of them is coated with aluminium and serves as cathode). This region is actively pumped reducing drastically the amount of detector gas leaking toward the magnet cold bores.

The calibration of the detector is done daily during non tracking times by shining a source of ^{55}Fe at the back of the detector. With the help of an automatic manipulator the

source is moved in front of four holes drilled in Plexiglas allowing the passage of the 5.9 keV X-rays.

The X-ray Telescope and the pn-CCD

Mounted on the remaining aperture (V1) of the MFB side is the CCD Detector [13], comprising the X-ray Telescope which focuses the resulting photons onto an X-ray CCD, this assembly is expected to collect the resulting photons after conversion during the Sunrise solar tracking.

The detection principle relies on an X-ray Telescope which focuses the X-ray flux onto a focal plane detector with high spatial resolution, allowing a enhanced signal-to-noise ratio on the detector spot and a simultaneous measurement of signal and background reducing systematic effects.

The X-ray Telescope concept is based on the Wolter I mirror optics, and is a spare module of the one used in the ABRIXAS space mission [14]. It consists of 27 nested, gold coated nickel shells, which are con-focally parabolic and hyperbolic arranged, to focus the X-ray flux at a distance of 1600 mm (see Figure 2-9).

The assembly of shells is divided in 6 sectors, and it is needed only one to completely overlap the cold bore aperture.

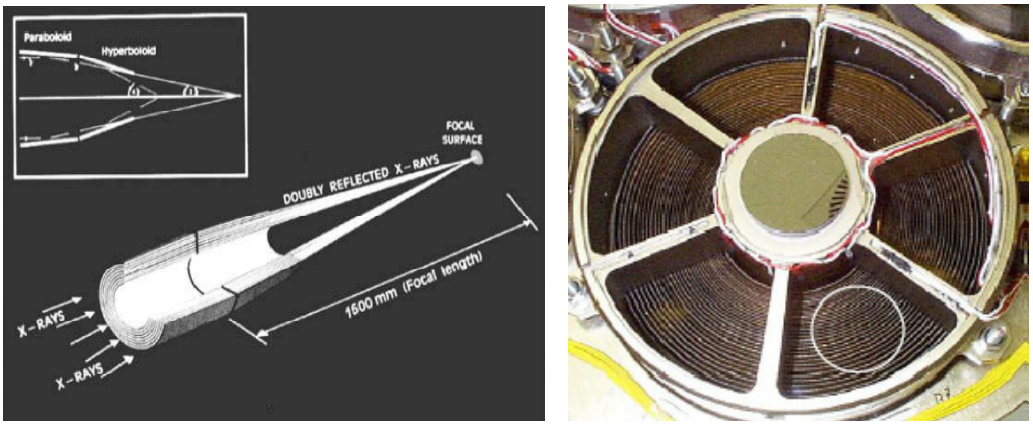

Figure 2-9: Left- Wolter I type telescope composed by parabolic and hyperbolic sets of shells, Right- Picture of the front view of the X-ray telescope which is divided in 6 sectors, the white circle represents the 43mm aperture of the magnet cold bores.

The assembly of shells has an outer diameter of 163 mm, 76 mm inner diameter and is about 300 mm wide. To maintain a good reflectivity of the shells, the X-ray Telescope is maintained under vacuum (better than 10^{-5} mbar), thus reducing the risk of contamination of the mirror surface.

The X-ray photons are focused onto the fully depleted pn-CCD detector prototype which was developed for the European XMM-Newton X-ray observatory.

The detector chip mounted inside a vacuum vessel and layers of shielding, is made by a set of 200×64 pixels, each of size 150×150 μm^2 (meaning a sensitive region of 3×1 cm^2) is much larger than the expected axion image[3] focused by the telescope having 19 pixels diameter.

The pn-CCD is cooled down to -130 ºC using a Stirling cooler which is thermally clamped with the detector cooling mask with copper braids (see Figure 2-10).

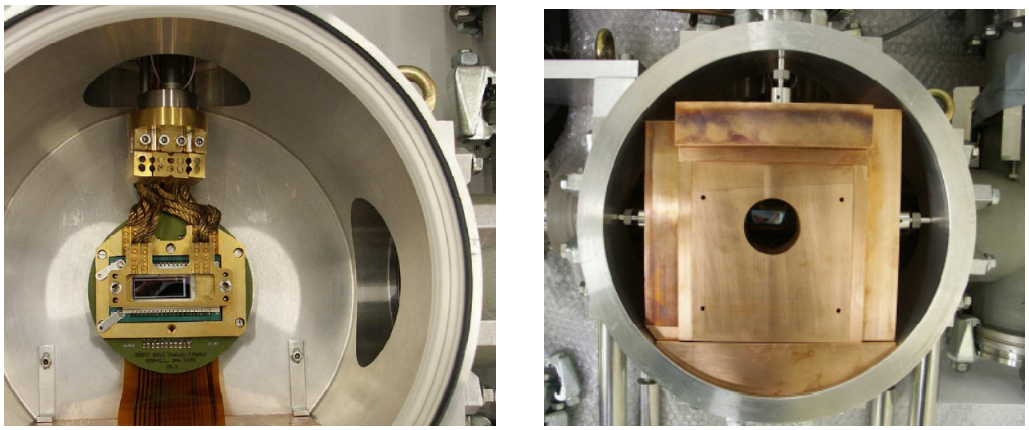

Figure 2-10: Left-The CCD chip and the cooling mask thermally clamped to the cold finger of the Stirling cooler with copper braids, Right-CCD detector housed in the shielding cage inside the vacuum chamber, aperture in the front for passage of focused X-rays.

In order to reduce the background the detector is shielded by (inside to outside): one layer of ancient lead with 2.2 cm thickness and one layer of low activity copper. Installed outside the vacuum vessel it is mounted an additional layer of 25 mm lead.

[3] - Focused image of the converted axion from the inner part of the Sun ($0.2R_{\odot}$)

To provide maximum performance, the optical axis of the X-ray Telescope is aligned with the magnet axis using a parallel laser beam, shining through the whole system, with a pointing accuracy better than 40 arcsec.

To monitor the long term stability of the alignment, an X-ray source emitting mainly 8 keV photons, is positioned in the opposite side of the magnet and has the possibility to be moved in and out the field of view of the telescope, allowing an X-ray image to be generated in CCD[4].

2.4 The Cryo plant

The smooth operation of the superconducting magnet is assured by a dedicated cryogenics plant (Cryo Plant) supplying superfluid helium (LHe^4) which maintains the magnet at a stable temperature of 1.8 K (a diagram of the cryogenics plant can be seen in Figure 2-11).

The Cryo Plant needed to support and maintain the operation of the magnet, was assembled by recovering and adapting parts from the former electron-positron collider (LEP2)[5] cryogenics (helium buffers and gas bags) and the dismounted DELPHI[6] experiment (helium liquefier, recovery and purification systems), plus a roots pumping group.

The cooling of the magnet is provided by a bath of pressurized superfluid helium at 1.8 K, using a hollow-finger heat exchanger. The heat exchanger is fed with liquid helium (LHe) taken from the bottom of a 4.5 K bath that is sub-cooled in a copper mesh heat exchanger before a Joule-Thomson expansion to saturation at 1.5 kPa.

The heat load from the magnet is transported along the superfluid bath to the exchanger and an electro-pneumatic actuated “respirator” valve place at the bottom of the 4.5 K bath, and allows filling of the liquid and pressure compensation of the superfluid helium.

[4] - Because the X-ray source is located at a shorter distance compared with that of the Sun, the X-rays are focused by the Telescope 30 cm behind the CCD, and therefore the observable x-ray image is larger than that of the expected from converted axions.

[5] - The Large Electron-positron Collider was one of the largest particle accelerators ever made. It was built at CERN and operated until the end of the year 2000. It accelerated electrons and positrons to a total energy of 45 GeV in its first phase, and later achieving an energy of 209 GeV.

[6] - Detector with Lepton, Photon and Hadron Identification (DELPHI) was a high precision particle detector used during the LEP runs.

To connect the rotating magnet with the Cryo Plant that is stationary, semi-flexible transfer lines run overhead and interconnect the Magnet Feed Box (MFB) with the pumping group and cold box.

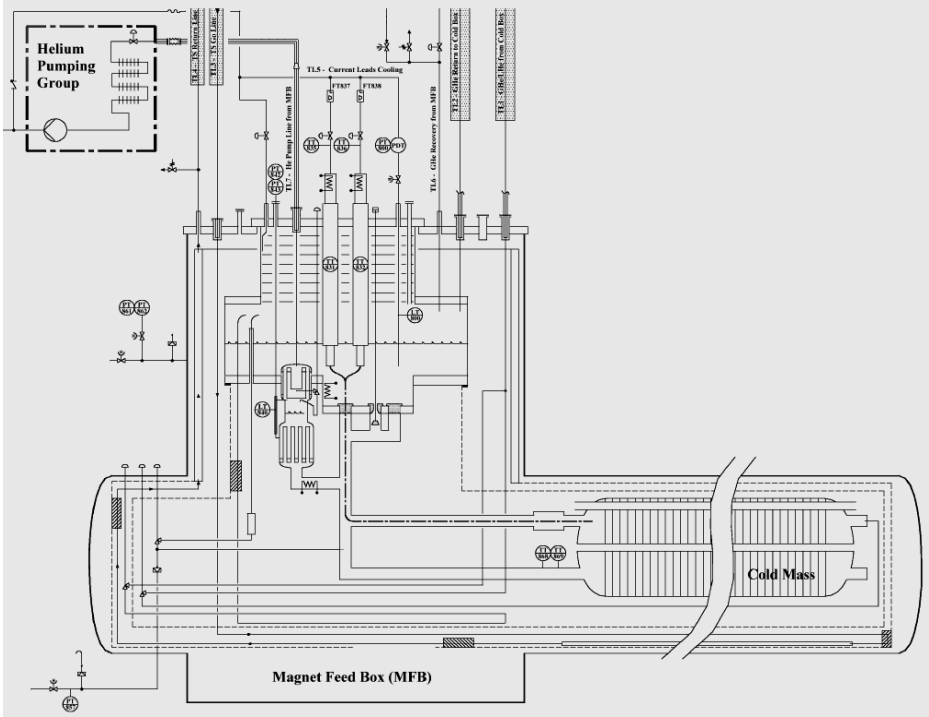

Figure 2-11: Process and instrumentation diagram of the cryogenics plant. The picture shows the different elements inside the magnet feed box (MFB) and the pipework that connect to the magnet cold mass, thermal shielding, 4.5 K bath and pumping group.

2.5 The Tracking System

For the alignment of the magnet with the Sun during the Solar tracking periods, the experiment relies on a tracking system that enables the rotation in two axis of the whole experiment structure weighting over 55 Ton with high precision.

The hardware part of this system, is constituted of the platform on which the magnet is mounted, and two support structures placed at each end of the magnet that allow both the support of the weight and the vertical and horizontal movement.

On the MRB extremity side the yellow girder moves on top of circular rails on the floor of the experimental hall and has two lifting screws that connect with the magnet structure. On the MFB side a rotating turntable serves as pivot point for the tracking movement.

Due to restrictions imposed by mechanical and cryogenic constraints, the vertical movement is limited to $\pm 8^{\circ}$, this is the reason of having two tracking periods both in the Sunrise and Sunset of 1.5 h each. As for the horizontal movement the $\pm 40^{\circ}$ rotation movement limited by the walls of the experiment is sufficient to cover all the positions of the magnet due to seasonal change[7].

The tracking movement is driven by two motors, (one for the vertical, the other for the horizontal movement), which are connected to angle and frequency encoders that are controlled by software.

To ensure personnel and hardware security, emergency stops allow the operator to stop the magnet movement. The movement to the extreme positions is secured by software limits and hardware switches that protect the moving equipment from touching non-moving parts and the magnet from exaggerated tilting or derailing.

The software that controls the movement of the magnet (see Figure 2-12) runs in the background a routine based on NOVAS[8], that calculates the Solar azimuthal and zenith angles based on the computer time, date and the location of the CAST experiment[9], and therein calculates the motor encoder values for the following minute, in order to have a precise alignment with the Sun core.

[7] - In the course of the year, due to the orbit of the Earth around the Sun, the tracking movement relative to the experimental zone is always changing.

[8] - Naval Observatory Vector Astronomy Subroutines.

[9] - 46°15'N, 6°5'E, 330 m above sea level.

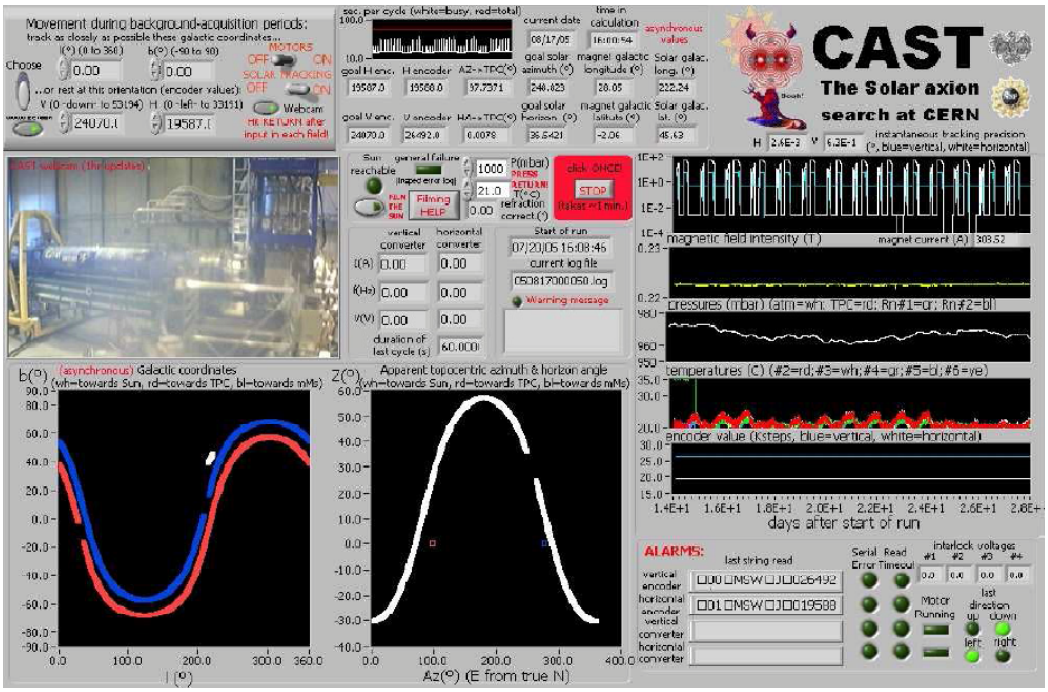

Figure 2-12: Snapshot of the Tracking System software, that displays the magnet movement in both galactic coordinates and apparent topocentric azimuth related to the horizontal angle. Atmospheric conditions such as temperature and pressure are also displayed.

To have a precise correspondence of the magnet position and the motor encoder values, an extensive measurement of the magnet position is done by CERN surveyors, which create a spatial map of the magnet coordinates translated into encoder units.

Two times per year, a cross-check measurement of the magnet alignment is done by aligning a CCD camera with the magnet axis and observing directly the Sun light that enters the experimental hall, through a window aperture made express for this purpose.

The result is a film from which the pointing accuracy, corrected with the refraction of light in the atmosphere, can be validated for each position in time.

Both these two methods show that the pointing accuracy of the magnet to the Sun is within the required precision of 0.017º.

2.6 The Vacuum System

During the First Phase of the experiment, the magnet cold bores were kept under vacuum, which was a requirement for the desired coherent conversion for axions into photons for axion masses below 0.02 eV/c^2.

A vacuum system was put into place to provide the required vacuum level in the magnet bores, but also to provide active pumping in various regions to avoid possible contamination of the system by a leak originated in any of the detector warm windows (MM or TPC) or a possible atmospheric leak.

Each one of the three detectors has its own pumping group and set of valves which ensure safe manipulations. Apart from the CCD detector that relies on a Programmable Logic Controller (PLC) to control and operate its system, the other two detectors rely on interlocks that are activated whenever pre-established vacuum limits are reached.

The vacuum system has suffered a great evolution to ensure further extraordinary manipulations, redundancy on failure of equipment and guarantee safety during all operations and for these reasons it has become a very complex system.

2.7 Data Monitoring

In order to monitor and record the different parameters of the experiment a so called 'Slow Control' system gathers the most relevant information, which is stored and can be consulted for future analysis.

The software written in Labview® (the user interface can be seen in Figure 2-13), displays information such as: temperatures and pressures, position of valves, loads and encoder values

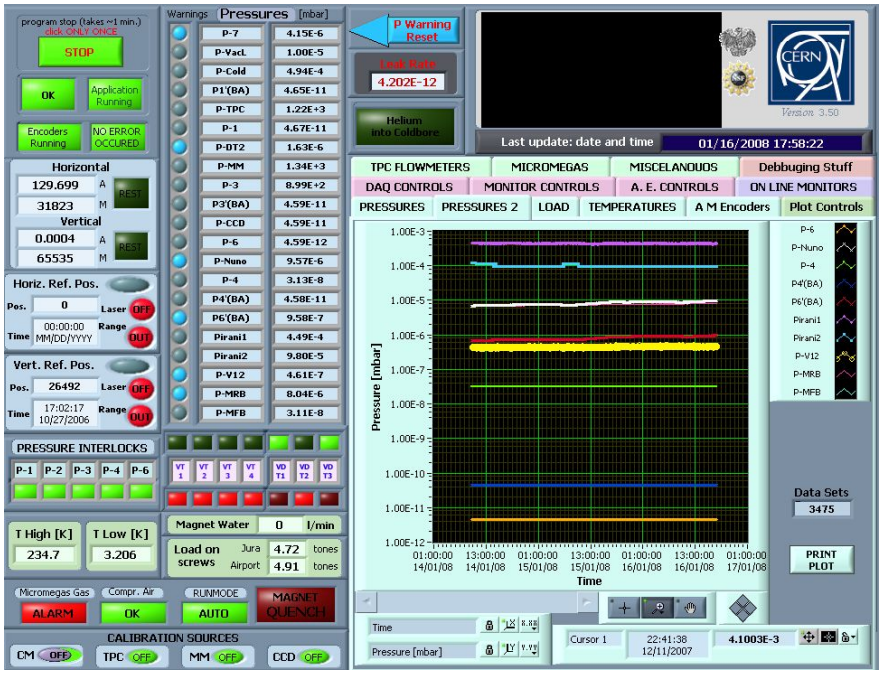

Figure 2-13: Snapshot of the Data Monitoring system (Slow Control)

Following the evolution of experiment, the number of instruments monitored is in constant upgrade and improvement. The Slow Control includes also the possibility of sending alarms when pre-established values are reached (such as pressures and valves). This allows the responsible persons to be informed of changes that can be vital for the normal operation of the experiment.

2.8 Results of CAST First Phase and prospects

The first CAST physics runs with the magnet cold bores under vacuum were made in the years 2003 and 2004. During this time all three CAST detectors have been collecting data. The total sun tracking data being collected for 300 hours and the background data for an order of magnitude longer. All three detectors were significantly improved from 2003 to 2004.

In the CCD detector, the X-ray telescope system was optimized, the pointing stability of the x–ray telescope was continuously monitored, and allowed to reduce the area in the detector where the axion signal is expected by a factor of 5.8. This results in essential improvement for the signal to noise ratio, since the same expected signal was concentrated in a much smaller area.

Moreover, by improving the shielding characteristics, the specific background level dropped by another factor of 1.5. The analysis procedure is thoroughly described in [9]. The axion-photon coupling $g_{a\gamma}$ results in an upper limit of $8.9 \cdot 10^{-11}$ GeV^{-1}, at the 95% CL.

The TPC detector, looking for sunset axions, was housed in a new shielding, consisting of a 5 mm thick copper box placed inside a 22 cm thick polypropylene housing made of successive shielding layers, 1 mm of Cadmium and 2.5 cm of Lead. The housing was permanently flushed with nitrogen, creating an overpressure, pushing away any radon contamination in the area of the detector. These measures produced a reduction in the of a factor of 4.3.

Detailed information on the TPC detector can be found in reference [11]. The upper limit on $g_{a\gamma}$ from the TPC data for 2004, is $1.29 \cdot 10^{-10}$ GeV^{-1}, at the 95% CL.

The Micromegas detector was placed on the west end of the magnet, looking for sunrise axions. The newly designed version of the detector operated smoothly during 2004 data taking and the analysis technique has been also improved, resulting in a background level, suppressed by a factor of 2.5 compared to the 2003 data set). These improvements allowed to set an upper limit to $g_{a\gamma}$ from the MM 2004 data of $1.27 \cdot 10^{-10}$ GeV^{-1}, at the 95% CL.

Taking into account all three detectors and the data sets of both years 2003 and 2004, we obtained for axion masses below 0.02 eV a final combined upper limit of $g_{a\gamma} < 8.8 \cdot 10^{-11}$ GeV^{-1} (with 95% CL). Figure 2-14 summarizes the combined upper limit of CAST in the axion phase space, where in the x-axis is the axion rest mass, and in the y-axis the coupling constant $g_{a\gamma}$.

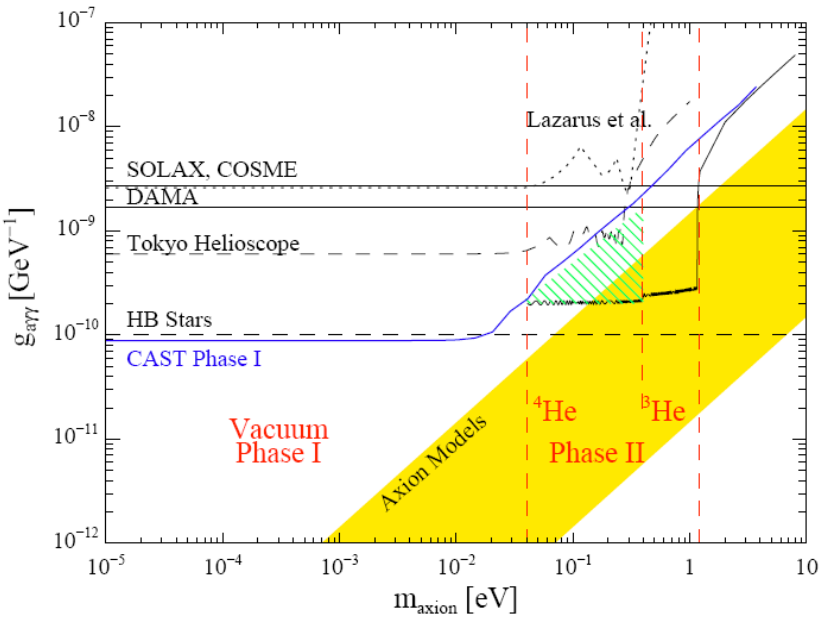

Figure 2-14: Exclusion plot of CAST First Phase, indicating as well the results for previous experiments and future prospects. Limits from astrophysical and cosmological arguments are also shown.

For the first time an experimental setup reaches a limit better than the one given from arguments based on the population of Horizontal Branch stars in globular clusters.

For axion masses higher than 0.02 eV, the axion to photon coherence condition is lost, since their oscillation length is reduced, thus the consequent increase for the excluded values of the coupling constant. In the previous figure the result of CAST is plotted together with the results from previous experiments, as well as the limits derived from astrophysical and cosmological arguments.

The following sections of this thesis focus on investigation that was done to overcome the coherence loss, describing the steps that were done for the implementation of a reliable system able to allow CAST to search for massive axions above the present limit.

3 Detection of Massive Axions

In Section 2 the methodology for detection within the CAST experiment was described and a brief introduction was given for solutions on how to extend the axion mass reach. In this section it will be given further attention to the latter, introducing the requirements and solutions adopted to maximize discovery potential within the limited time frame of the CAST experiment.

The influence of the gas dynamics will be approached and the results of numerical models are presented to estimate its effects.

3.1 Buffer gas as conversion media

As it was shown in section 2.8, after the physics runs that lasted up to the end of the year 2004 (CAST First Phase), the CAST Collaboration was able to publish a remarkable result, by setting an upper limit on the axion-photon coupling of $g_{a\gamma} < 8.8\times10^{-11}\mathrm{GeV}^{-1}$ at 95% CL for axion rest masses bellow 0.02 eV/c^2.

Whilst the coupling limit can be enhanced by having optimized low-background detectors and longer exposure time, the axion mass reach is bounded to the physics of the axion to photon conversion, which by having the magnet cold bores under vacuum, leads to a coherence loss for axion masses higher than 0.02 eV/c^2.

To overcome this constraint, a novel method proposed by K.V.Bibber et al. [1], allows the coherence to be restored for higher axion masses. The method consists in filling the magnet bores with a low-absorption buffer gas. This induces an effective photon mass (plasma frequency) which can be adjusted to equal the axion mass, by fine tuning the buffer gas density.

In these conditions the axion conversion probability has to be calculated in a new form, where the absorption of the gas is taken into consideration:

$$P_{a\to\gamma} = \left(\frac{B\cdot g_{a\gamma}}{2}\right)^2 \cdot \frac{1}{q^2 + \Gamma^2/4} \cdot \left[1 + e^{\Gamma L} - 2e^{-\Gamma L/2}\cdot cos(qL)\right], \tag{3.1}$$

with Γ representing the inverse photon absorption length in the medium.

The momentum transfer now acquires a new form:

$$q = \left|\frac{m_\gamma^2 - m_a^2}{2E_a}\right|. \tag{3.2}$$

where m_γ is the effective mass of the photon in the buffer gas.

Re-arranging equations (3.1) and (3.2) we arrive to the conclusion that the coherence condition $qL \le \pi$ is satisfied for a given axion mass within a small range.

$$\sqrt{m_\gamma^2 - \frac{2\pi E_a}{L}} < m_a < \sqrt{m_\gamma^2 + \frac{2\pi E_a}{L}}. \tag{3.3}$$

The above formula shows the challenge ahead, since in order to scan the axion mass one needs to do a corresponding scan of the buffer gas density which is limited by the

saturation pressure at the operating temperature of the medium, and for a given gas density the axion conversion is only coherent within a very narrow window of the axion mass.

The resulting photon effective mass m_γ, is correlated with the electron density n_e, of the gaseous medium by:

$$m_\gamma \approx \sqrt{\frac{4 \cdot \pi \cdot n_e}{2 \cdot m_e}} \tag{3.4}$$

where m_e is the electron mass.

The electron density n_e, can be written in the form:

$$n_e = \frac{2 \cdot p \cdot N_A}{R \cdot T}, \tag{3.5}$$

where p is the absolute pressure, N_A the Avogadro constant, T the temperature of the gas, and R is the Universal gas constant, 83.144 $\text{mbar} \cdot 1 \cdot \text{mol}^{-1} \cdot \text{K}^{-1}$.

A simplified formula relates the photon effective mass with the gas pressure p and temperature T (having Helium as gas medium):

$$m_\gamma \left[\text{eV}\right] \approx \sqrt{0.02 \frac{p\left[\text{mbar}\right]}{T\left[\text{K}\right]}}. \tag{3.6}$$

By having a buffer gas media with a particular density, the coherence can be fully restored, but for a narrow axion mass range (equation (3.3)), and therefore, in order to scan the axion mass a corresponding scan of the buffer gas density needs to be done.

Figure 3-1 makes a comparison between measurements made by keeping the magnet cold bores under vacuum and in the presence of a buffer gas (Helium) for a given observation time (33 days).

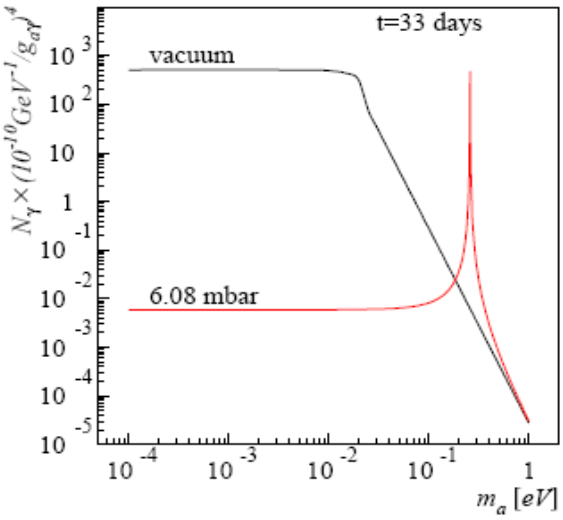

Figure 3-1: Comparison between measurements made with the magnet cold bores kept under vacuum and in the presence of a buffer gas. The number of photons has been calculated for an exposure time of 33 days and a coupling constant of 10^{-10} GeV^{-1}.

In the figure above it is shown the expected number of photons after conversion with respect to the axion mass for two different scenarios, either by having the cold bores under vacuum (First Phase), or by having a fixed gas density inside the magnet cold bores (e.g. helium at 6 mbar and 1.8 K).

It is shown that for the same exposure time and for a given gas density the coherence is restored and CAST sensitivity is re-established. This occurs for a very narrow range in axion rest masses, and therefore an accumulation of multiple density settings is needed for a full coverage of the available mass range.

3.2 The Choice of gas

The choice of a suitable gas to work as buffer volume in CAST Second Phase, depends in first instance on finding the appropriate chemical element that remain gaseous at the very low magnet operating temperature, bearing in mind the photon absorption length of the medium, so that the axion rest mass reach can be enhanced.

At the magnet nominal operating temperature (1.8 K) only two chemical elements remain gaseous, Helium-4 (^{4}He) and Helium-3 (^{3}He). The use of these elements on their

gas phase up to the saturation pressure would allow extending the axion mass reach to: 0.43 eV and 1.20 eV respectively.

An alternative solution would be to use 'anti-cryostats'. 'Anti-Cryostat' is a gas cell that could be introduced inside the magnet cold bores and operated at a higher temperature. The advantage of using an 'anti-cryostat', is that the temperature of the gas cell can be set to an higher value than that of the magnet cold bores, and therefore chemical elements with higher saturation temperature could be used, such as Hydrogen.

The use of Hydrogen in a gas cell maintained at a temperature of 30 K would allow for example to reach the axion mass limit of >2.0 eV, but with important disadvantages.

The 'anti-cryostat' solution would require the introduction of gas cells through all the magnet length, which apart from being a technical challenge to implement would also require its temperature to be maintained homogeneous through all its length, and since the new gas cell would need to be placed inside the existing magnet cold bores it would result in a reduction of the effective area for axion conversion.

Moreover, at 30 K the saturation pressure of Hydrogen is 8 bar, which would require very robust confining elements, and in case of a superconducting magnet resistive transition the absolute pressures that would be reached could get to alarming values for equipment and an important safety risk for the experiment.

On the contrary the introduction of the buffer gas directly in the magnet cold bores offers very efficient thermal anchoring, due to very high thermal conductivity of superfluid helium used for magnet cooling. In terms of safety the whole system could work at sub-atmospheric pressures requiring standard high vacuum materials.

In this scenario, to reach of the astrophysical limits and to enter the axion mass range favoured by theoretical modes, one would require the use of very expensive and rare gas (^{3}He) and the construction of a complex gas system for handling it.

After balancing all these pros and cons the CAST Collaboration took the decision of adopting the solution to have the buffer gas directly in the cold bores. This would allow a first learning stage with ^{4}He, which ultimately allows the preparation and design of the complex ^{3}He gas system. Furthermore LLNL[10] as a member of the CAST Collaboration has the means to provide the necessary amount of ^{3}He gas (as loan).

[10] LLNL stands for Lawrence Livermore National Laboratory in US, an applied science laboratory part of the National Nuclear Security Administration. It is responsible for ensuring that the US nuclear weapons remain safe, secure, and reliable through application of advances in science and engineering.

Gas Properties

Helium-4 (^{4}He) is a stable, non-reactive element. The nucleus of the atom consists of two protons and two neutrons. It is odourless, colourless and tasteless. Helium-4 is the second most abundant element in the Universe. This gas is being studied for many years as a consequence of its unique properties.

In its liquid phase ^{4}He presents two states, one of which the liquid is superfluid (i.e. zero viscosity). It is used in many applications, from spectroscopy to coolant in superconductive magnets.

Physical Constants Helium-4 [^{4}He]	
Molecular weight	4.003 g/mol
Boiling point	4.22 K
Critical point	5.19 K
Saturation Pressure (1.8 K)	16.405 mbar
Half life	Stable
Spin	zero

Table 3-1 – Summary of ^{4}He properties

Helium-3 (^{3}He) is a stable, non-reactive and lighter isotope of ordinary Helium (^{4}He). The atom nucleus has two protons and one neutron. It is odourless, colourless and tasteless. The natural abundance of ^{3}He in the Earth is 1.38×10^{-6}. This very rare gas is used in detectors, NMR tracers, spectroscopy, low temperature physics, lasers, dilution refrigerators, R&D laboratories and it is sought after for use in nuclear fusion research.

Physical Constants Helium-3 [^{3}He]	
Molecular weight	3.016 g/mol
Boiling point	3.19 K
Critical point	3.35 K
Saturation Pressure (1.8 K)	135.58 mbar
Half life	Stable
Spin	½

Table 3-2 – Summary of ^{3}He properties

3.3 Scanning the axion mass

In order to contemplate the available domain for the axion rest mass in a methodical and efficient manner, similarly the buffer gas density has to be precisely adjusted. In the next section it is described the methods to permit an efficient axion mass scan.

Density step size

In a steady regime the temperature of the gas inside the magnet cold bores is constant and equal to the superfluid helium used for the magnet cooling, therefore one can express the gas density as a function of its absolute pressure, hence the number of expected photons for a given time interval can be calculated for a fixed buffer gas pressure setting.

$$\rho = \frac{n \cdot M}{V} = \frac{p}{T} \cdot \frac{M}{R}. \tag{3.7}$$

Here M is molar mass of the buffer gas.

In Figure 3-2 it is compared the expected number of photons after conversion for three different scenarios: vacuum, 0.08 mbar and 0.16 mbar of ^{4}He at 1.8 K, for the same exposure time and effective area.

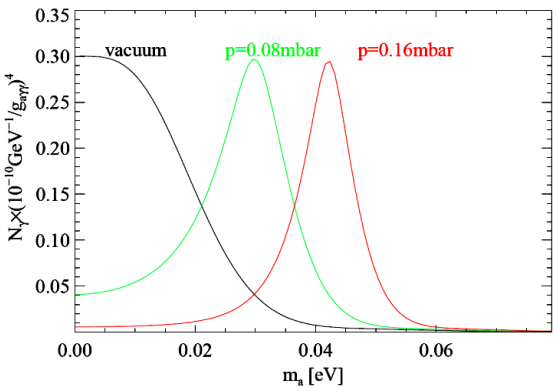

Figure 3-2: Comparison of the expected number of counts N_γ for three different scenarios: vacuum, 0.08 mbar and 0.16 mbar of ^{4}He at 1.8 K (assuming a coupling constant $g_{a\gamma}$ of 10^{-10} GeV^{-1} for energy range of 1 to 10 keV, with an exposure time of 1 hour and effective area of 14.5 cm^2).

For the vacuum case, the number of expected photons falls dramatically for high axion masses, but in the case of having a buffer gas with 0.08 mbar (at 1.8 K) it allows

to maximize the expected number of photons for an axion mass of ~0.03 eV and for 0.16 mbar the maximum expected number occurs at ~0.045 eV.

For a given density setting, the photon counts are expected to peak at a given axion rest mass with a characteristic distribution similar to that of the Figure 3-2, thus an axion signature can be determined by tuning the buffer gas density for that with highest number of photon counts and therefore the axion rest mass can be determined.

Due to the fact that the axion rest mass still remains an unknown, one of the goals of CAST is to cover all the available mass range with the same sensitivity, thus requiring the need to control the buffer gas density in the cold bore.

The method to optimize the discovery potential and to cover the available axion mass reach within the limited CAST operation time frame is by overlapping the axion mass distribution at FWHM[11] between two consecutive density settings.

In order to make it possible, the buffer gas density will need to be consecutively increased in metered steps. The optimized density step size at a given setting, taking in account the photon absorption in the medium is shown in Figure 3-3.

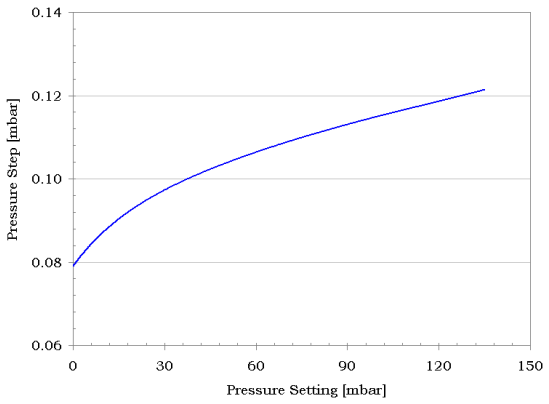

Figure 3-3: Optimized pressure step size as a function of the pressure setting value, courtesy B. Lakic

The density step size increases for higher axion masses, and varies between ~0.08 mbar and ~0.12 mbar for a maximum pressure of 120 mbar. This has as first

[11] Full With at Half Maximum (FWHM) is an expression used to designate waveforms; it represents the difference between two extreme values on a curve at which the wave reaches half its maximum value.

consequence that in order to optimize the axion mass coverage, the size of the density steps is not constant, but is continuously increasing in size.

3.4 Density Stability, Reproducibility, Homogeneity

The parameter that drives the physics of the axion-to-photon conversion in CAST Second Phase is the electron density inside the magnet cold bores subject of a high transversal magnetic field.

During a solar tracking period the magnet cold bores will be filled with a known amount of gas which will correspond to the desired electron density. It is thus required that the buffer gas density remain unaffected by any external conditions that might affect its stability.

Assuming that one could confine the buffer gas in a closed volume in the 1.8 K region then the electron density would be independent of temperature variations. Unfortunately there is no way to confine the gas only to this region and in practical terms one will have to deal with a system that is operating between the magnet temperature and the ambient temperature, Figure 3-4 represents in simplified way the different volumes contiguous with the cold bore of representing the gas system:

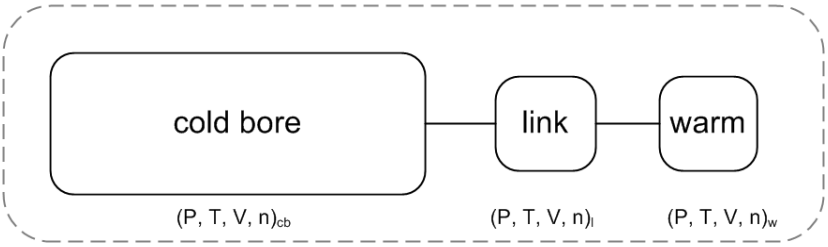

Figure 3-4: Diagram of the various volumes contiguous with the cold bore

The ‘cold bore’ region is defined as the volume inside the cold bores which is thermally stabilized by the superfluid liquid helium for the magnet cooling operating at a nominal value of 1.8 K; The ‘warm’ region is the section of the pipework which is outside the cryostat and therefore at ambient temperature; ‘link’ is the section of pipework between the cold bore and the warm section, which has a temperature distribution strongly dictated by the thermal conductivity of the pipe material. Both ‘link’ and ‘warm’ regions will be further called ‘dead’ regions since they are indifferent for the axion physics.

In any region of the system the behaviour of the gas can be described using this form of the equation of state for a perfect gas:

$$n_i = \frac{p_i \cdot V_i}{R \cdot T_i}\left[\text{mol}\right]. \tag{3.8}$$

For a temperature variation of in any of the regions, the gas density in the cold bore will be adjusted, since the equilibrium will be reached for an equal pressure through all the system.

In case of a magnet resistive transition (see section 4.2) a rapid temperature increase takes place in the cold bore, with a consequent pressure rise. In order to prevent that the pressure reaches alarming values with the possibility of breakage of the thin cold X-ray windows there are 2 possible approaches for gas system design, 'open' or 'closed' system:

In the 'open' system the 'dead' volumes are maximized and in case of a quench the pressure rise is limited by the large dimensions of the 'dead' volumes.

In the 'closed' system the 'dead' volumes are minimized and in case of quench the gas is extracted from the system to avoid high pressures.

It becomes necessary to evaluate the effects of temperature fluctuations on the gas density stability in the cold bore during normal operation and assess its result on a stability threshold.

Assuming δT_C as a fluctuation in cold bore temperature, the pressure will have a consequent variation δp , but the total amount of gas n_t remains constant (detailed formulation in Appendix B):

$$\begin{aligned} n_t = n_c + n_l + n_w = p \cdot \left(\frac{V_c}{R \cdot T_c} + \frac{V_l}{R \cdot T_l} + \frac{V_w}{R \cdot T_w} \right) = \\ = \left(p + \delta p \right) \cdot \left(\frac{V_c}{R \cdot \left(T_c + \delta T_c \right)} + \frac{V_l}{R \cdot T_l} + \frac{V_w}{R \cdot T_w} \right). \end{aligned} \tag{3.9}$$

The relative pressure change as a function of the cold bore temperature fluctuation is given by:

$$\frac{\delta p}{p} = \frac{n_c}{n_t} \cdot \frac{\delta T_c}{T_c}. \tag{3.10}$$

And finally the density variation in the cold bore by:

$$\frac{\delta\rho}{\rho} = \frac{n_l + n_w}{n_t} \cdot \frac{\delta T_c}{T_c}. \tag{3.11}$$

From the above result it is possible to see that density variations due to variations of the cold bore temperature are a function of the amount of gas in the 'dead' volumes, thus in order to improve the density stability to values lower than 10^{-4}, it becomes obvious that one should minimize the 'dead volumes', and subsequently the 'closed' system becomes preferable to the 'open' system.

Possible ways to minimize density fluctuations pass by a minimization of 'dead' volumes, which can be solved by an effective reduction of the pipe diameter, but with the drawback that in case of need for a fast gas extraction. Another solution passes by increasing the temperature in these regions, generating a detrimental heat load increase posing additional aggravation on the cryogenics cooling power.

At this stage it is possible to estimate the dimensions of the system (volumes involved) and define the normal operation point (temperature). With ^{3}He the maximum pressure setting will be 135 mbar, limited by the saturation pressure at 1.8 K and the molar mass for ^{3}He is 3.016 g/mol.

For the normal operation conditions with a pressure setting of 100 mbar:

Region	Temperature [K]	Volume [litres]	Nr of moles [mol]	Density [g/litre]
Warm	~293	0.80	3.30×10^{-3}	1.24×10^{-2}
Link	11.04 K[12]	0.62	6.71×10^{-2}	3.29×10^{-1} ([13])
Cold Bore	1.8	31.22	2.086×10^{1}	2.015
Total			2.093×10^{1}	-

Table 3-3: Temperature, volume and total number of moles present in the different regions of the system.

[12] Numerical modeling was made to evaluate the temperature distribution along the different regions, and will be presented in section 3.6. The model takes in consideration the thermal conductivity of SS316, found in [15]. The effective temperature comes from $T_{eq} = (P/n_l)(V_l/R)$, with $(n_l/P) = (1/R) \cdot \int_0^L V_{(x)}/T_{(x)} dx$.

[13] The density of the gas in the 'link' volume is dependent on the temperature; this value represents a effective density calculated from the total number of moles divided by the volume of 'link'.

Having a very restrictive density stability threshold of 10^{-4} at the extreme pressure setting (assumed 100 mbar), results in a stability precision equivalent to 10 μbar at 1.8 K.

The maximum allowable temperature fluctuation in the cold bore, can be calculated by re-arranging equation (3.11) it is possible to calculate.

$$\delta T_c = T_c \cdot \left(\frac{n_l + n_w}{n_t} \right) \cdot \left(\frac{\delta\rho}{\rho} \right). \tag{3.12}$$

This is valid for any pressure setting, since the ratio $\left(n_l + n_w\right)/n_t$ is approximately constant through the entire regime.

Substituting with the values for the normal operating conditions and $(\delta\rho/\rho) \approx 10^{-4}$, the maximum allowable temperature variation reaches the value of δT_c < 53.51 mK (with a consequent pressure variation is 2.963 mbar). The same calculation can be done for the regions 'warm' and 'link' and results in much less restrictive temperature fluctuations of 507 K and 0.355 K.

Another important requirement for CAST physics is reproducibility, meaning the capability to go back to the same density setting later in future.

In order to allow re-visiting a given density setting with high precision, the amount of gas sent into the magnet cold bores has to be precisely measured and the history of the accumulated amount recorded.

The measurement of the amount of gas transferred to the cold bore is calculated by accurately measuring the pressure decrease on the metering volumes that are maintained at constant temperature of 309.15 K by means of a thermostatic temperature controlled bath with temperature stability and accuracy better than ±0.01 K. Given the stability of ±2 K in the temperature of the pipework (with about 25 cm^3 volume) exposed to the ambient temperature (due to air conditioning accuracy), the effective stability of the temperature in a 10 litre metering volume is better than 37 ppm.

The measurement of a single full-scale (FS) pressure measurement in the metering volume is done with an accuracy of 30 ppm taking in account only the precision of the temperature controlled metrological MKS Baratron gauge, and the drift of its zero and span under ambient temperature variation. At 10% of FS the relative accuracy is 75 ppm, yielding 43 ppm accuracy for the measurement of Δp between 90% and 10% FS readings.

This and the effective temperature variation yield the reproducibility of 60.6 ppm for the amount of gas sent from the 10 litre metering volume into the magnet, for an amount of gas making a change of 1 mbar in the pressure of the buffer gas at 1.8 K.

By repeating the metering process N times we can reproduce an earlier setting of the amount of gas in the magnet bore. This process increases the variance of the gas mass at 1 mbar by $\sqrt{N}$ and yields the relative uncertainty in the mass $\delta n / n$ and uncertainty in the absolute equivalent pressure δp_{eq} calculated at 1.8 K.

p_{eq} (mbar)	N	Step size (mbar)	$\delta n / n$	δp_{eq} (mbar)
1	1	$8.00 \cdot 10^{-2}$	0.0061%	$6.06 \cdot 10^{-5}$
10	10	$8.73 \cdot 10^{-2}$	0.0192%	$1.92 \cdot 10^{-3}$
60	60	$1.06 \cdot 10^{-1}$	0.0469%	$2.82 \cdot 10^{-2}$
120	120	$1.19 \cdot 10^{-1}$	0.0664%	$7.97 \cdot 10^{-2}$

Table 3-4: Reproducibility in the terms of relative mass and absolute equivalent pressure, with which a previous setting of the buffer gas mass can be recalled, using a 10 liter metering volume.

From the above table it is possible to conclude that the pressure can be well reproduced when compared to the desired step size through the entire ^{3}He vapour pressure regime. At 10 mbar the reproducibility is about 2% of the pressure step size, at 60 mbar 47% and at 120 mbar about 67%. In order to assure a good coverage of a desired setting to be reproduced, it might be convenient to revisit the contiguous pressure setting allowing a good overlap of the axion mass distribution.

3.5 Finite Element Model

The use of finite element analysis (FEA) allows complex geometries to represent real geometry in a mathematical model consisting of a mesh of elements in multiple simplified discrete regions. Initial boundary conditions are set to define a given problem and equilibrium equations, complemented with applicable physical considerations and properties are applied to each element. A matrix of equations is constructed and solved in a fast computer processor.

To investigate the temperature distribution of the solid boundary with the gas a FEA was performed. It represents the region previously called ‘link’, which connects the superfluid liquid helium cooled cold bore with the X-ray window flange which is

thermalized at a higher temperature. This region has a complex geometry and high temperature gradients are present thus representing an interesting point for the effects on the gas density.

The tube material is stainless steel (SS) 316L, and since the metal thermal conductivity is at least two orders of magnitude higher that of the Helium (see Figure 3-5), as a first stage approximation it is only considered the heat transfer by conduction through the wall (solid model).

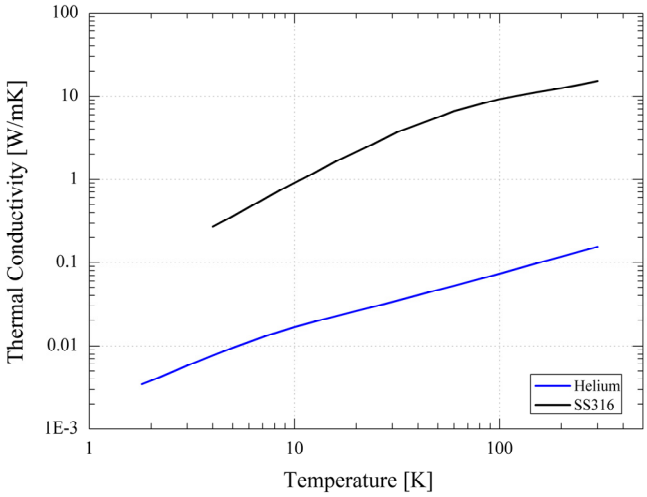

Figure 3-5: Thermal conductivity as a function of temperature for Stainless steel SS316L taken from Compendium of the properties of materials at low temperature, for ferrous alloys [15].

The first stage is to define the geometry of the problem and adapt the element size for an optimized accuracy of the solutions versus the computing time. Figure 3-6 shows the CAD[14] representation of the matrix element corresponding to the real geometry. The model represents only one of the extremities of the cold bores is constituted by more than 66000 finite elements.

[14] Computer Aided Design

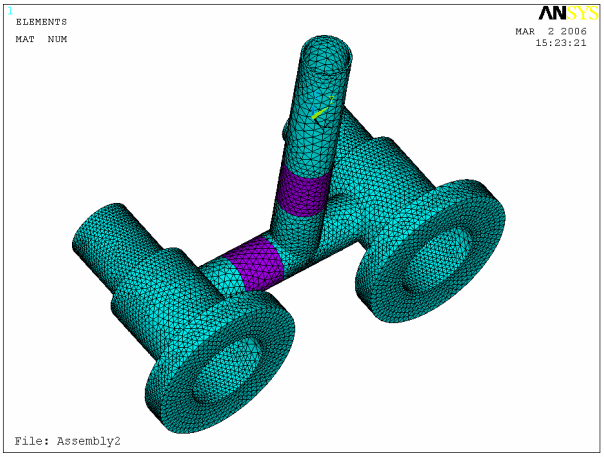

Figure 3-6: Finite element modelling of the cold bores domain outside the magnet and connecting to the ambient temperature region.

The next step is to apply the boundary conditions to the model. On the window flanges surface it is applied a fixed temperature value of 120 K and on the annular section of the cold bore tube which is wetted by the superfluid helium a fixed temperature value of 1.8 K is applied. On all other surfaces is applied an adiabatic wall condition. It is also assumed that there are no heat losses to the cryostat vacuum, and that radiation heat transfer is too small to be considered.

A convergent solution of the analysis is obtained, meaning that equilibrium is reached. The FEA software allows generating output result files or presenting the results in a graphical form which is presented in Figure 3-7.

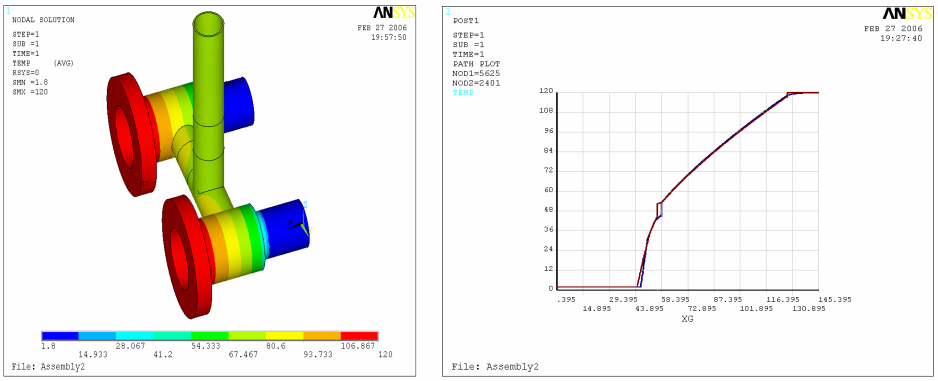

Figure 3-7: Results of the solid model simulation showing the temperature distribution of the domain (left) and the temperature distribution along the cold bore axis (right).

As a result of the solid simulation one can determine the temperature distribution along the pipework that connects the liquid helium cooled cold bore at 1.8 K to the X-ray

cold windows that can be thermally controlled to a temperature of e.g. 120 K. Although this result does not express gas behaviour it can be included as boundary condition in a more complete computational fluid dynamics (CFD) simulation.

3.6 Computational Fluid Dynamics Model

To compute the fluid dynamics behaviour of the gas, a powerful CFD software is used, Ansys CFX®. The geometric domain of the volume occupied by the gas is re-defined by a fine mesh composed by more than 160000 discrete tetrahedral finite elements as shown if Figure 3-8. The helium properties are modelled as an ideal gas fluid, where the dynamic viscosity and thermal conductivity behaviour is approximated by the Sutherland's formula.

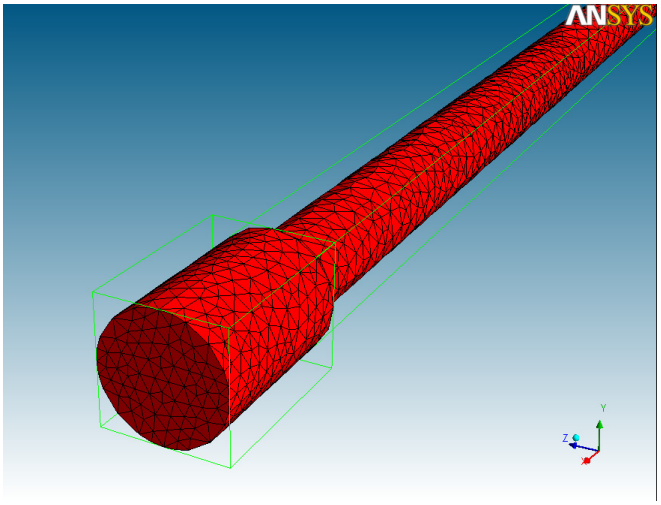

Figure 3-8: Mesh generated by the CFD software pre-processor representing the gas domain inside the magnet cold bores. The picture shows the detail of the MRB extremity.

The temperature profile given by the solid model is applied as boundary condition. In reality the coupling of the fluid with the surrounding surfaces will consequently make its temperature to change due to the necessary heat transfer for equilibrium to be reached, but that would require a more complex simulation where both solid and fluid model can interact with each other in a dynamic process for a steady state regime.

Therefore in the present simulation, the heat transfer given by a fixed temperature profile on the surface will lead to higher global heat exchange from the walls to the fluid than in the real case, and more important effects will be seen by the fluid.

In order to compute the effects of convectional heat transfer buoyancy is active, where gravity acceleration is included on a stationary domain. Heat transfer by radiation is not included and it is used a laminar turbulence model, due to the very small Reynolds number.

To compute the effect of the increasing gas density inside the cold bore throughout the experiment lifetime, several scenarios are analyzed to cope with computing time limitation, where the static pressure is adjusted for different scenarios.

In Figure 3-9 it is presented a graphical representation of one solution where both temperature distribution and density distribution magnitude is represented in a color map.

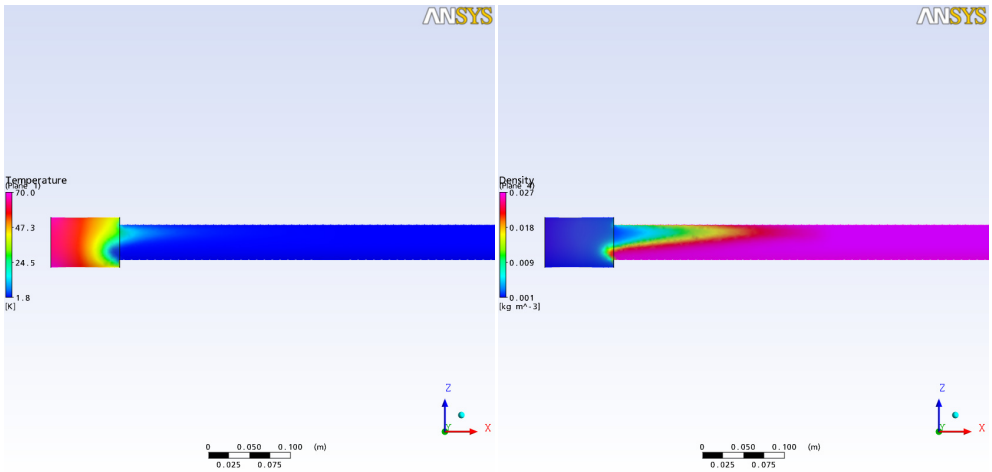

Figure 3-9: Colour map representing the temperature (left) and density (right) distribution on a vertical axis crossing the cold bore axis for one of the scenarios at a static pressure of 1mbar. The picture shows the detail on the MRB side.

The result shows the effect of the gas interaction with the warmer walls nearby the X-ray window region relative to the cold bore, creating a warmer and consequently low density region on the magnet extremities that propagates inside the cold bore.

4 Studies for the Second Phase upgrade

A buffer gas filling the conversion region of the CAST magnet is necessary in order to extend the axion mass search above 0.02 eV/c^2 with maximized sensitivity.

The requirement for a physical boundary between the buffer gas and the vacuum system demands for research, development and testing of novel elements able to assure leak-tightness at cryogenic temperatures, mechanical robustness and maximized X-ray transmission (section 4.1).

Undesired superconducting magnet resistive transition (quench) is a phenomenon that can occur in CAST. This leads to a rapid temperature rise and a consequent pressure increase of the buffer gas. The transient behaviour of the buffer gas thermodynamic properties during the quench is consequently one essential aspect to scrutinize, so that safety measures can be adopted to minimize the attained pressure during such an event (section 4.2).

The introduction of gaseous helium in the cold bores of an LHC magnet prototype is an experience without precedents, where interesting phenomena were measured, like the occurrence of spontaneous thermally driven acoustic oscillations which unfortunately are to be a characteristic of the original experimental setup.

A numerical model was constructed to understand which parameters play an important role and possible solutions for the elimination of the problem were proposed and constructed (section 4.3).

Due to the necessity of cold thin X-ray windows to isolate the buffer gas region from the vacuum system undesired behaviours were observed in the vacuum system. If no action is taken, residual gases on the vacuum system are cryo-pumped into the window foil, ultimately diminishing the X-ray transmission. Section 4.4, reports on the observance of evidence on this behalf and measurements done to evaluate the origin of the gases and discusses possible solutions to be implemented.

4.1 The cold thin X-ray windows

One of the most stringent elements on the upgrade of CAST, with the goal of having a buffer gas as conversion media, is the need to implement a physical interface between the buffer gas and vacuum system at each extremity of the cold bores, further called cold thin X-ray windows.

The main function of this element is to confine the buffer gas in the cold region of the magnet bores, so that a known and stable amount of gas can be maintained in the conversion region over long periods of time.

The development of the cold thin X-ray windows was done to optimize its characteristics in order to: minimize the loss of gas by diffusion, maximize the transmission of X-ray photons in the interesting energy range (2 keV to 10 keV) and be mechanical robust as to withstand the maximum attained differential pressure.

The philosophy adopted consists in the use of low-Z thin foils for an improved X-ray transmission. The choice of the material and its thickness arises from the hermeticity requirement and need keep the mechanical integrity of the foil when the maximum differential pressure is attained.

The hermeticity requirement is derived from the condition of having an accurate control of the gas amount inside cold bores.

The use of a very thin foil, can be used for X-ray transmission enhancement, however a compromise needs to be reached due to the disadvantage of increasing the diffusion of helium molecules through the material from the pressure side into the vacuum side.

A quantification of a maximum allowable gas loss over a running period of one year, lower that one density step size (see section 3.3), would result in a maximum allowed leak rate through each of the four windows to be smaller than $3.8 \cdot 10^{-6}$ mbar·l·s^{-1}. This value is normalized to ambient temperature, for easily comparison with helium leak-testing measurements using commercially available helium leak detectors, these allowing to achieve measurements down to the $1 \cdot 10^{-9}$ mbar·l·s^{-1}.

In nominal working conditions the pressure across the window foil cannot be surpassed to that of the saturation point of the gas (16.405 mbar for ^{4}He and 135.58 mbar for ^{3}He at 1.8 K), but whenever a magnet quench occurs (see section 4.2) a rapid temperature increase takes place, which causes the pressure of the gas to increase accordingly in an isochoric process, reaching a maximum increase of about twenty times the initial value in a few seconds, producing a maximum pressurization across the window of ~0.3 bar for ^{4}He and 2.7 bar for ^{3}He.

The implementation of active and passive measures will be included in the design of the final ^{3}He gas system, with the goal of limiting the maximum attained pressure across the windows to 1.2 bar, which remains a big challenge using micro-thickness foils at cryogenic temperatures.

The four cold thin X-ray windows are to be mounted between the existing ultra-high-vacuum CF63 flanges located at the ends of the magnet (Figure 4-1 illustrates the assembly and its dimensions) which separate the magnet cold bores from the vacuum system.

The leak tightness to the magnet cryostat is assured by the sealing made by the knife edges that penetrate a flat copper gasket by a shear action introduced at the moment of tightening.

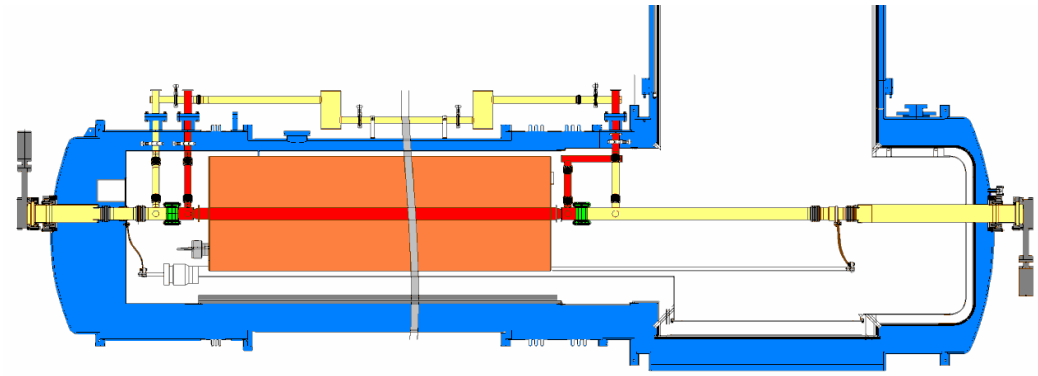

Figure 4-1: This drawing illustrates the position of the cold X-ray windows (marked in green) placed between the cold bore tubes (red) and the vacuum tubes leading to the detectors (yellow), the magnet (orange) is places inside the cryostat (blue), the left side of the picture is the MRB and right side the MFB of the magnet, for reasons of illustration not the complete length of the magnet is displayed.

Geometry

The geometry of the cold thin X-ray windows consists of a cylindrical stainless steel element (316LN) with CF63 flanges. The foil is glued on one of its sides to a strong-back structure which is machined by electro-erosion.

The strong-back forming a grid of squared cells each having a 5.2 mm side, with a width of 0.3 mm and 5 mm depth, is produced by electro-erosion done with a 0.25 mm wire to a precision of ± 0.01 mm. The surfaces are cleaned by a 4 hours immersion in a nitric acid water solution (50% HNO_3 + 3% HF + 47% H_2O), which smoothens the sharp edges, producing a rounding of ~5 μm. The final 2 min electro-polishing bath produces a final rounding of ~30 μm, leaving a ~240 μm wide flat surface to deposit the glue.

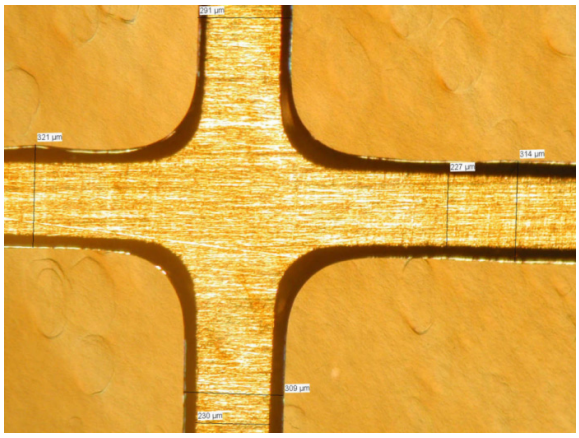

Figure 4-2: Picture of the detail of the polypropylene film glued onto the metallic strong back (x50 zoom). Notice the structure of the foil.

This treatment has the drawback of making the adherence of the glue more difficult and for that reason a light grinding is done to create micro-roughness that will be filled by the glue. The surface is finally cleaned with a degreasing agent to facilitate the adherence process.

The very delicate gluing process is done in a clean room and consists on covering the strong back surface with a very thin layer of Araldite 2018 (resin/hardener mixture), the foil is then pre-stressed as to avoid any wrinkles and lowered onto the struts with an applied contact pressure until the cure of the adhesive is finished.

To finalize, a top cover made of a stainless steel ring, is glued on the sides of the strong-back and the top peripheral border of the foil, this confers extra resistance against peeling and provides mechanical protection.

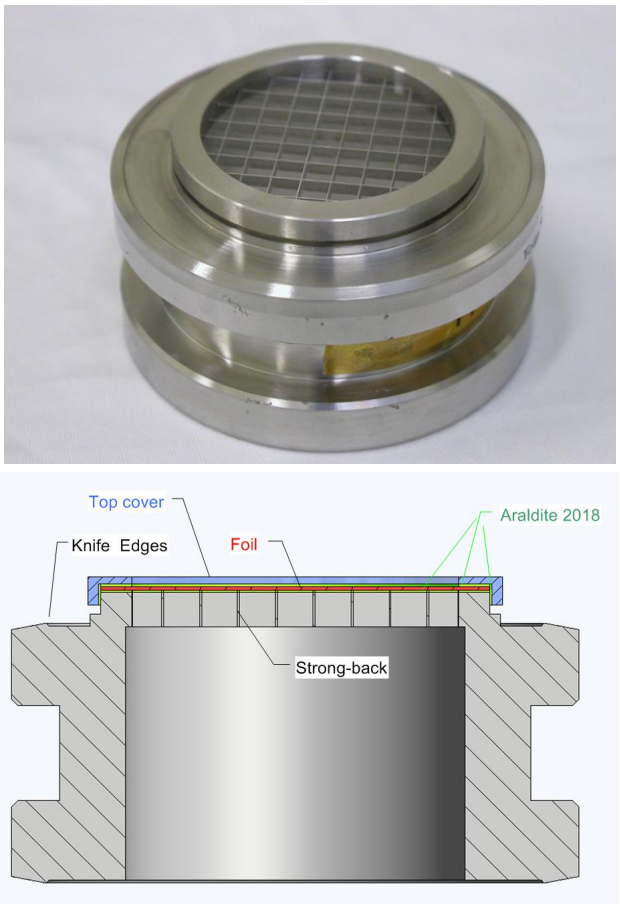

Figure 4-3: Window mounted on a CF63 flange; Top - Photograph showing the squared geometry of the cells and the top cover; Bottom - cross section indicating the different components.

Developments and tests

The optimization of the geometry relies in a series of tests to validate the final concept in all three fields: hermeticity, X-ray transmission and robustness. In terms of transmission the strong-back itself has a geometrical loss of ~10.6%, and was optimized by minimizing the projected area of the grid which is a compromise to concentration of stresses on the foil which can lead to plastic deformation and rupture, also its depth confers resistance against deformations caused by the acting pressure.

The choice of the foil material and its thickness was driven by the low X-ray transmission and on the other hand by its mechanical robustness.

The fraction of gamma rays T transmitted through a thickness x, can be calculated if the linear attenuation coefficient μ is known[15] for the interesting energy range using the formula $T = e^{-\mu x}$.

In Figure 4-4 Top) we compare the transmission of two different materials available in the market,. It is shown that for the interesting region of X-ray energy. A more robust foil made of polypropylene (C_3H_6, with 15 μm thickness presents approximately the same transmission to that of 5 μm thickness Mylar ($C_{10}H_8O_4$).

On Figure 4-4 Bottom) it is compared the transmission of polypropylene $(C_3H_6)_x$ of 15 μm thickness to that of the buffer gas through a 5 m path at different pressures. It is shown that for pressures above ~10 mbar the gas transmission has a prevailing role over the foil transmission.

[15] - The values were taken from the NIST and LLNL databases

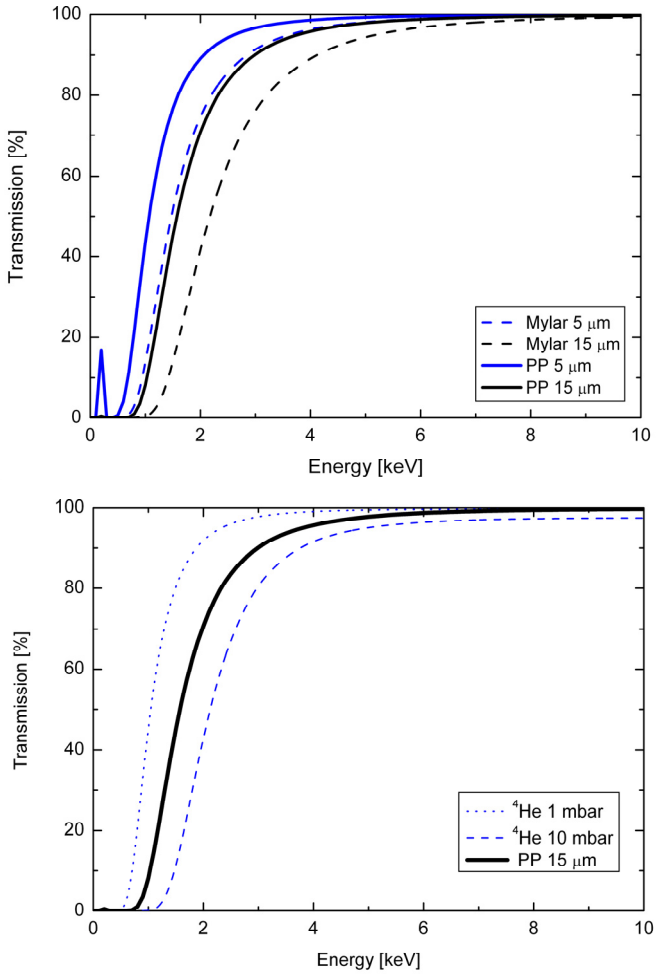

Figure 4-4: Top) X-ray transmission across foils of polypropylene and mylar with different thicknesses. Bottom) X-ray transmission comparison between a 15 μm thickness polypropylene foil and a 5 meter long path though helium at different pressures.

In order to measure the hermeticity of the foils a cryogenic test setup was mounted in the Cryolab [16] which allowed the prototype windows to be tested at different temperatures and pressures.

The testing facility (see Figure 4-5) allows a cryostat to be filled with liquid helium; the level of the liquid can be adjusted and the temperature of the bath below 4.2 K can be

[16] - CERN Central Cryogenics Laboratory

adjusted by active pumping. The cold thin X-ray window is mounted in between two CF hermetic flanges, and separates the gaseous helium supply line, from the pumping line connected to the leak detector.

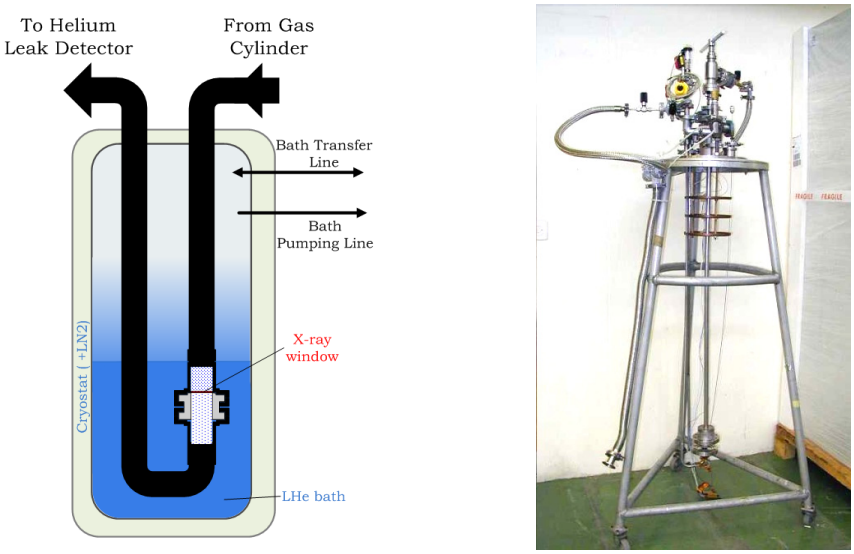

Figure 4-5: a) Schematics of the test bench, the window is pressurized with helium supplied from the cylinder, the temperature of the window is adjusted by the height adjustment relative to the bath surface; b) Picture of the setup that is lowered into the LHe bath and transfer lines, the widow is fixed in the bottom.

A mechanical system allows the window to be positioned at different heights relative to the liquid surface, thus enabling the temperature of the window to be adjusted, either by cooling with vapours or full emersion in the liquid. A heater connected to the window flange also allows the temperature to be adjusted by controlling the power dissipated. The pressure of the gas supply can be finely adjusted using a manostat and a set of dosing valves connected to the helium supply cylinder.

The leak rate of helium through the polypropylene film can be measured with a conventional helium detector. Theory says that gases permeate through uncoated plastics by diffusion at a rate that diminishes at low temperatures. The dependence of the flow rate of gas depends on the temperature according to [16]:

$$p\dot{V} / A = b \cdot D_0 \cdot e^{-(Ea/kT)} \cdot \Delta p / h, \qquad (4.1)$$

where p is the upstream pressure at which the volume flow rate $\dot{V}$ is measured (at standard temperature), A is the surface area of the film, b is the solubility of the gas in

the plastic, D_0 is the diffusion constant of the molecules of the gas in the material, E_a is the activation energy for diffusion, and h is the thickness of the film.

Results of the tests for the 15 μm polypropylene are presented in the following table resumes the tests made at different temperatures:

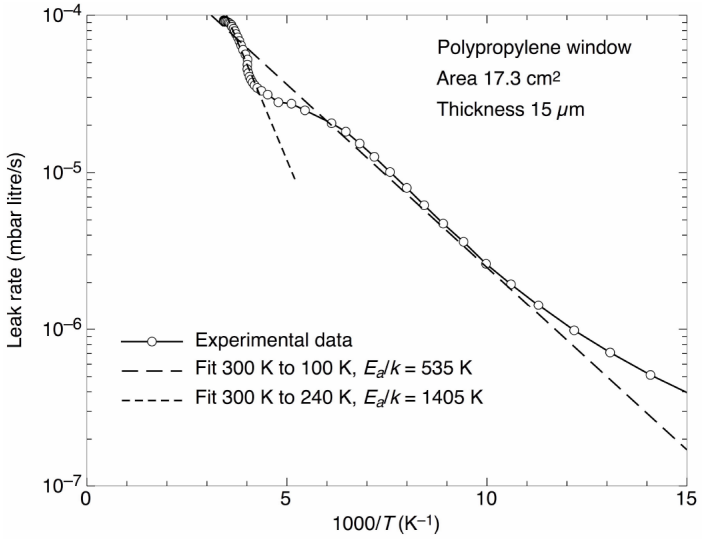

Figure 4-6: Measured helium leak rate (round markers), and fits of data to the diffusion model [17], with b·D_0 = 4.6·10–8 mbar·litre/(bar·cm2/cm)

Amongst 11 windows tested, 8 showed a behaviour similar to that presented in the above figure. Three of the windows had leaks a few orders of magnitude larger, which increased at low temperatures, which indicates possible presence of pinholes or cracks in the film.

In order to simulate the fast pressure rise during a magnet resistive transition, the windows were also tested for rapid pressurization.

These tests include room temperature and cryogenic temperatures pressure cycles. At each cycle the leak tightness of the window was monitored and a sudden pressure rise was applied, a displacement sensor located on the strong-back was able to measure the movement due to the pressure increase. Table 4-1 resumes the results achieved in those tests.

The tested window was pressurized up to 3.5 bar differential pressure without rupture or showing any degradation of its properties. This very encouraging result served to prove that the chosen thickness of the foil, geometry of the strong-back and the

materials used are in agreement with the stringent requirements for the use of buffer gas with a sufficiently large safety margin. Moreover this result served to be very useful input parameters in a mathematical model to confirm and optimize the geometry of the window.

Number of cycles	Pressure [bar]	Temperature [K]	Displacement [μm]
1	1.5	300	9.3
1	1.5	120	9.2
4	1.5	60	8.8
1	2.0	60	11.7
2	2.5	60	14.5
1	3.0	60	17.8
1	3.5	60	20.6

Table 4-1: Summary of the rapid pressurization tests

4.2 The Superconducting Magnet Resistive Transition

The resistive transition from the superconducting to the normal-conducting state is called quench. When a quench takes place, the stored magnetic energy is dissipated in the form of heat, causing an abrupt temperature rise.

A quench can potentially cause damage in superconducting elements by overheating or excessive voltages, moreover with the introduction of a buffer gas in the magnet cold bores the rapid temperature rise can lead to a fast pressurization putting at risk the integrity of sensitive elements and to the possibility for an undesirable loss of gas.

The quench phenomenon can occur when the so called ‘critical surface’ parameter space is reached and most of the times this can happen by external factors unrelated to the CAST experiment itself, to avoid any related damage a quench detection and protection system are implemented.

Due to the use of a superconducting magnet in the CAST experiment the risk of quench cannot be eliminated, and the introduction of a buffer gas in the enclosed volumes of the magnet cold bores raises an additional problem of a rapid pressure rise due to the temperature increase, with the risk of possible window leakage or breakage, damage of instrumentation or loss of precious ^{3}He gas.

In order to understand the quench phenomenon, and with the aim of limiting the gas pressure rise below reasonable safe pressure values, a series of tests and measurements took place in view of measuring the gas temperature transient).

The results of these tests served as input to model possible passive and active protection solutions to be implemented in the final ^{3}He gas system.

Niobium-Titanium (NbTi) is being used worldwide in the construction of powerful superconducting magnets. One example of its application is the most famous particle accelerators like the LHC.

Hard superconductors such as NbTi are characterized by a critical current density as a function of an applied magnetic field at a given temperature. The relation of these three quantities is known as the critical surface, shown in Figure 4-7. Due to flux creep the resistivity of hard superconductors does not completely vanish, and the critical current density J_c for a given set of T and B is usually defined by the criterion that electrical resistivity is $\rho = \rho_c = 10^{-14}\,\Omega\mathrm{m}$.

Niobium-Titanium has shown to be one of the best choices for the construction of the LHC magnets, one of the reasons was its ductility properties that allows an easy and effective fabrication process, although the upper critical field is only about 10 T (by cooling with superfluid helium) when compared to higher values that can be reached with Niobium3-Tin (Nb_3Sn) a much more brittle compound.

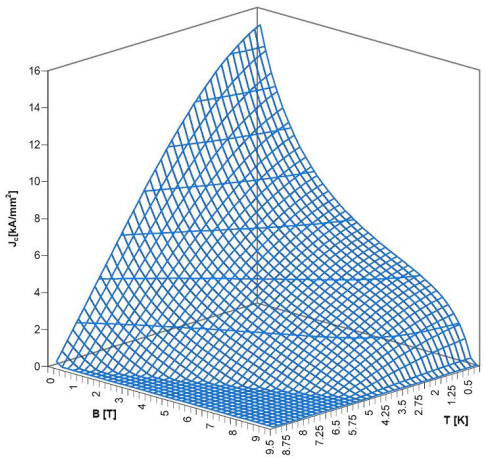

Figure 4-7: Critical Surface of NbTi with its three parameters, magnetic field, temperature and current density.

A 'real'[17] superconducting resistive transition (quench) can occur whenever one of the three parameters J_c, T_c or B_c crosses the critical surface, in this case the superconductor becomes normal conducting and if the cooling is not strong enough to recover back to the superconducting state the normal-conducting zone will spread out.

Since NbTi has high resistivity in the normal conducting state, the superconductors are stabilized with copper, this results that in case of a quench the current redistributes and bypasses the superconductor by flowing through the copper; this technique helps to reduce the risk of damage of the superconducting wire by reducing the heat generation. Multifilament wires embedded in a copper matrix, are twisted to minimize the strength of induced eddy currents, and each filament is of the order of a few microns to avoid flux jumping[18].

The LHC Rutherford cables [18] used in LHC is made of 20-40 multifilament wires which are folded forming a two-layer structure in a trapezoidal shape. The cable is permeable to superfluid helium so that there is an effective cooling of all wires. The insulation of the cable is done with polyimide films followed by a heat treatment of polymerization allowing the cable to be elastic both at room temperature and at nominal working temperature.

The unique properties of liquid helium below the λ - line (2.17 K) make it a perfect coolant, meaning that it can flow without friction (superfluid) and have a very high thermal conductivity. The phase diagram of Helium is displayed in Figure 4-8.

[17] - Most of the magnet quenches are caused by the quench protection system by firing the quench heaters, that permit a distributed and smooth warm up of the magnet when compared with a real quench where the resistive transition occurs in one weak point of the superconducting wire causing a overheating, a quench front and the possibility of permanent damage of the wires.

[18] - In the occurrence of a small heat dissipation in a superconducting wire of a given thickness will cause the temperature to rise and a consequent reduction of the critical current density, this increases the field inside the wire resulting in heat generation. Instability can be reached whenever the temperature reaches T_c. Depending on the wire thickness a slightest disturbance will cause the superconductor to expel the part of the captured magnetic field which is called flux jumping.

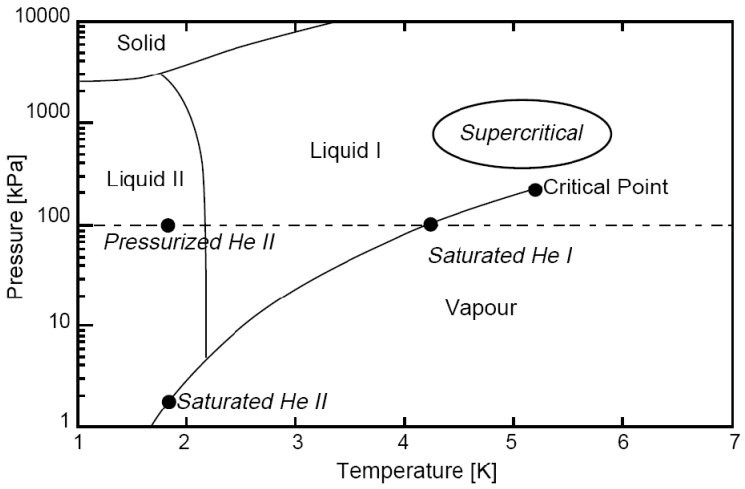

Figure 4-8: Phase Diagram of Helium-4, The superfluid phase (Liquid II) is reached when the temperature is lowered below the λ – point (~2.17 K), the solid phase only exist for pressures above ~30 bar, and at 1.8 K the gas phase no longer exists above 16.4 mbar.

The CAST magnet is cooled by a dedicated cryo-plant which keeps the magnet at a stable temperature of 1.8 K.

An historical record of the CAST magnet quenches, classified by their causes, is given in Table 4-2, for operation time from the year 2003 until the year 2006.

Year	Training	Natural	Cooling water of current supply	Current supply failure	Electromagnetic interference	Human error	Quench Protection Fault	Power failure (natural)	Power failure (emergency stop)	Unknown	Sum of quenches	Magnet operation (hours)
2003	1	2	0	3	1	1	3	2	1	2	16	2100
2004	2	0	3	0	0	1	0	0	1	3	10	3000
2005	1	0	0	0	0	0	0	0	1	0	2	500
2006	1	0	0	0	0	0	0	5	3	0	9	3500

Table 4-2: Number of unexpected quenches of the CAST magnet classified according to their causes. The quenches provoked during the tests of 2005 are not included.

It is shown that the main causes of quenches tend to be dominated by electrical power failures or auxiliary's failure, which are difficult to predict and control, for that reason a Quench detection and Protection system is required to ensure safety of the

superconducting elements and to avoid the experiment downtime for repair. The functions of this system are to detect a quench in the superconducting circuits and to deal with the stored magnetic energy.

The Quench Detection is done by having several voltage taps connected in relevant locations on the magnet coils. The voltage taps allow the monitoring of the voltage across each pole and aperture of the magnet. In order to detect a quench, the differential voltage signals are taken into account to eliminate the inductive part of the signal, whenever the value rises above the threshold (80 mV) for a given channel and for a period longer than the validation time (10 ms), an imminent quench is detected. When a quench is detected a 'quench-trigger' signal is sent to all relevant sub-systems, and the quench protection is engaged.

The quench protection prompts safety actions to be taken once the quench is detected, such as firing a set of quench heaters and a fast magnet power abort.

The quench heaters are composed of two steel strips connected in series and are placed all along the magnet length, in total there are eight quench heaters (four per aperture) placed between the magnet coils and the collars, these are heated by a capacitor bank which discharges after quench detection. The goal here is to make the superconducting magnet to become conductive as a whole, avoiding hot spots where the localized high temperatures and voltages can cause permanent damage.

The heat dissipation during a quench causes the magnet to rise temperature very rapidly; the superfluid helium used to cool the magnet is warmed up crossing the lambda point back to a normal fluid and further heating causes its boiling into gas. This phase transition happens very rapidly, and for safety purposes large amounts of gaseous helium are vented into the experimental hall, this spectacular event causes large bursts of cold gas to condensate the ambient air into white clouds, accompanied with loud noise.

Due to the rapid temperature increase of the magnet, also the buffer gas temperature will increase by heat exchange with the cold bores walls. If no action is taken, and as a consequence of the cold bores being a closed volume, the pressure of the buffer gas can rise very rapidly putting in danger the integrity of the cold X-ray windows, instrumentation, and a possible loss of gas can occur. For that reason the temperature transient of the gas in the cold bores should be measured so that protective measures can be implemented in order to limit the maximum pressure.

The following sections will shed some light on the research done and the solutions adopted.

Tests with blank windows

A provisional gas system was built with the aim of measuring the effects of a magnet quench in the temperature/pressure rise of the buffer gas. This system uses ^{4}He as buffer gas because of its gaseous properties at 1.8 K and its easy availability. Since this is the first time ever that ^{4}He is sent into the magnet cold bores, the adopted philosophy is to use blank cold windows instead of the final cold thin X-ray windows (under development). These blank windows are fully massive, meaning that the interface gas-vacuum is done by a robust 5mm thick 304L stainless steel wall.

To allow the necessary operations, a relatively simple gas handling system was put in place (see Figure 4-9).

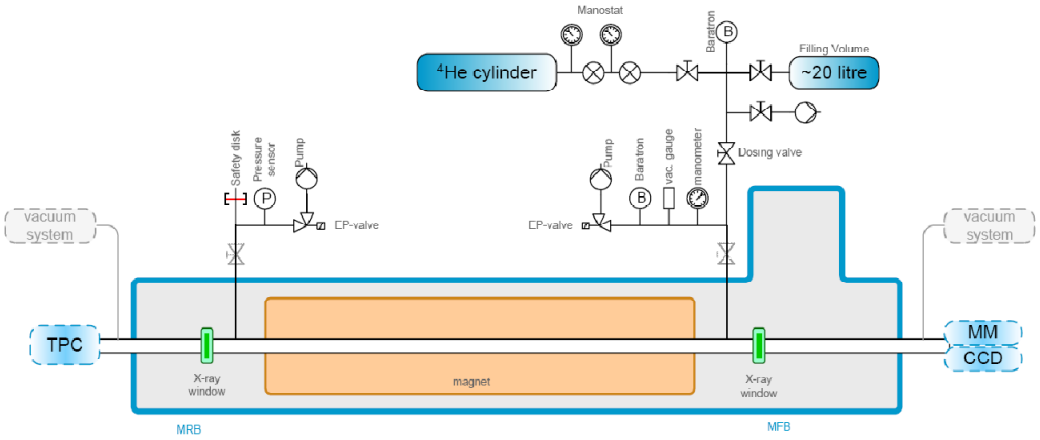

Figure 4-9: Scheme of the provisional Helium-4 gas handling system for quench tests.

The system consists of a ^{4}He cylinder and a manostat pressure reduction stage for the helium supply, the gas is transferred first into a filling volume of 20 l where the pressure is measured by a metrological pressure transducer (Baratron®), the gas can then be sent into the magnet cold bores via a multi-turn dosing valve. The measurement of the pressure in the buffer gas can be done by four different gauges: a precision metrological pressure transducer, a pirani vacuum gauge, a bourdon manometer (on the MFB side) and a capacitance pressure sensor (on the MRB side). On the MRB it is mounted a safety disk against overpressure that vents for a differential pressure above 100 mbar. This design gives additional safety against wrong manipulation avoiding that the cylinder is directly connected with the cold bores. At each extremity of the magnet two electro-pneumatic valves are mounted at the inlet of two ~30 m^3/h rotary vane vacuum pumps. If

needed and using the quench-trigger signal[19] these two valves are opened[20], allowing an active pumping of the buffer gas from the cold bores.

In order to extract the maximum information about the quench behaviour and minimizing the risk due to unknown parameters the quench tests program concept was scheduled according to Table 4-3, where at each test either the amount of gas or the current of on the magnet coils is increased and the active pumping can be triggered or not.

Quench	Pressure in Cold Bore [mbar]	Magnet Current [A]	Active Pumping [Yes/No]
A	3	1500	Yes
B	3	1500	No
C	3	8000	No
D	3	13000	Yes
E	3	13000	No
F	10	13000	Yes
G	10	13000	No

Table 4-3: Program of provoked quenches and parameters.

Tests A, B and C were done at lower currents than the nominal and serve only to gain extra confidence that all the parameters are under control.

Tests D and F were made at nominal current and extracting the gas via the two extremities of the cold bores with the help of the rotary vane pumps, the goal in these scenarios is to evaluate the time response of the electro-pneumatic valves for a possible future solution with active pumping.

In tests E and G the magnet current is set to its nominal value (13 kA) and the buffer gas is kept in the magnet cold bores during the quench (isochoric process), the gas pressure can be interpreted as an integral temperature measurement over the cold bore length, considering the apparatus a good approximation of a gas thermometer.

The goal on these tests is not to have an accurate measurement of a local temperature but to have a reliable evaluation of the overall pressure increase of the gas. The results of the most relevant tests are summarized in Figure 4-10.

[19] - The quench trigger signal is supplied by the quench detection system.
[20] - The opening time given by the supplier is 150 ms

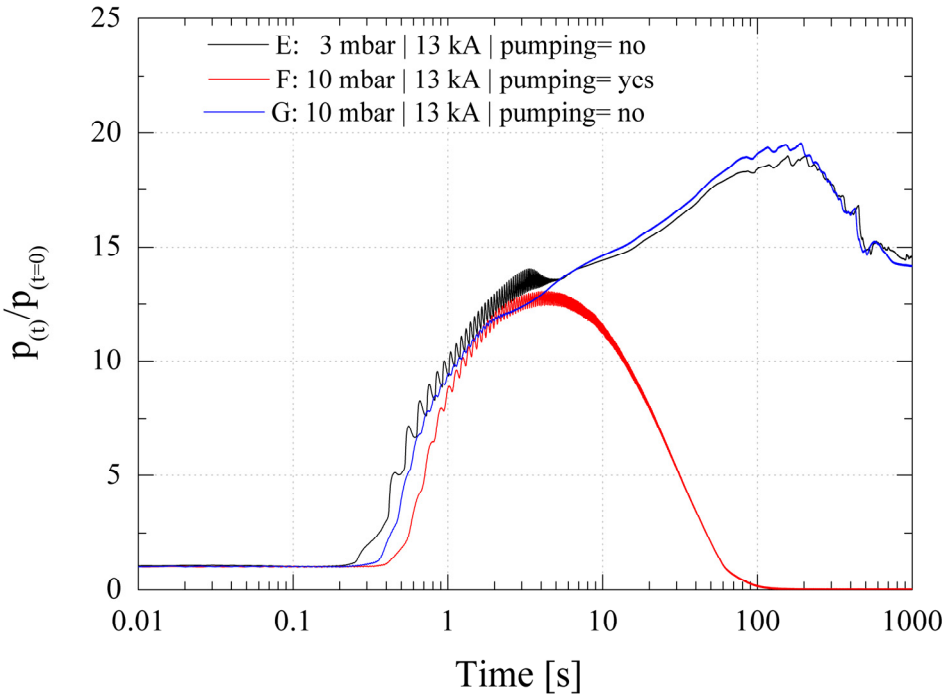

Figure 4-10: Measured pressure evolution during a quench with ^{4}He in the magnet cold bores. The plot shows the pressure increase $p_{(t)}/p_{(t=0)}$ as a function of time, being t=0 the quench time and p(t) the pressure at a given instant. The plot displays the recorded data by different sensors communicating with the cold bore for scenario E, F and G.

The results of tests E and G, show that the temperature rise of the buffer gas in the magnet cold bores has a behaviour that can be characterized in three phases:

- Dead-time of ~200 ms where there is no apparent pressure increase.
- Followed by 'fast' warm-up, up to the first 3 s where the pressure increase can reach the order of 13 times the initial value,
- And finally a 'slow' warm-up, with a maximum at about 100-200 seconds after the quench trigger, where the pressure increase reaches a maximum of ~20 times the initial value.

For scenario F the behaviour is similar during the first two phases, except for the last phase where the active pumping manages to overcome the pressure increase due to the quench and the pressure is reduced.

From the results of the previous tests one can extrapolate that in a future operation with ^{3}He gas in the magnet cold bores, with the maximum gas load (~130 mbar at 1.8 K), one would expect a maximum pressure across the cold thin X-ray windows of ~2.6 bar to be reached ~100 seconds after the quench (if no active pumping is set) and ~1.7 bar in the first 3 seconds (with and without active pumping).

During tests E and F it is present pressure oscillations through an important section of the time scale. During the test G this phenomenon is not present indicating that the phenomenon is pressure dependent and triggering within a specific range. This intriguing phenomenon will be addressed in section 4.3.

Simulations

In order to try to limit the maximum achievable pressure inside the magnet cold bores, as a result of a magnet quench, the results of the previous tests are now used as an input for the computation of possible solutions.

The adopted philosophy for the design of the final ^{3}He gas system is the condition of keeping, at any time, the whole system below atmospheric pressure. Adopting this idea would limit differential pressures to 1 bar, would make undesirable leaks detectable by pressure increase and restrict the loss of gas. As a result the maximum allowed pressure increase in the magnet cold bores during a quench would have to be limited to $P_{(t)} / P_{(t=0)} < 7.7$ for a total ^{3}He gas amount (130 mbar at 1.8 K).

It is clear from the results of the previous tests that protective measures need to be put in place; very little can be done on limiting the heat dissipated into the magnet cold bores, and as a consequence the temperature increase becomes a intrinsic variable of the system. A solution could be found by increasing the volume of the chamber (cold bores) and thus limiting the pressure.

Since the cold bores have a defined volume, a solution requiring a volume increase would have to pass by an additional reservoir to be put in contact with the later in case of quench. The connection would have to be done by fast opening valves with a response time smaller or similar to that of the dead-time.

The dimensions of the reservoir and the gas flow conduction of the connecting elements will have to be modelled and studied as to keep the pressure below the specified limit. A second solution to be studied is the possibility to extract the gas by active pumping.

The simplified mathematical model is represented in Figure 4-11.

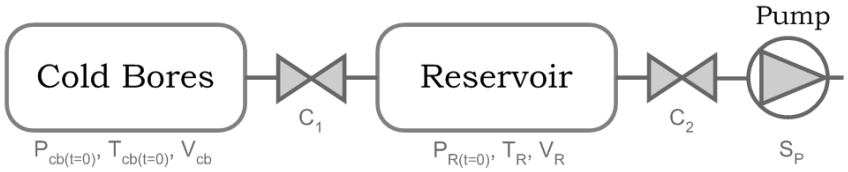

Figure 4-11: Schematic of the mathematical model, the amount of gas is enclosed in the cold bores, at t=0 (quench time) the valve C1 is opened and gas can flow into the reservoir, additionally the pump can be connected with the reservoir by opening the valve C2.

Initially the cold bores, with a volume $V_{cb} = 30\,\mathrm{l}$, contain the amount of ^{3}He gas at a pressure P_{cb} and temperature $T_{cb(t=0)}$=1.8 K . The reservoir volume V_R is initially under vacuum at $P_{R(t=0)}$=0 mbar and at room temperature T_R=293 K . At the instant $t = 0$ (quench time) the valve with conduction C_1 is opened thus connecting the cold bores with the reservoir. For modelling purposes the variables $P_{cb(t=0)}$, C_1, V_R and the possibility of pumping the gas through the pump with pumping speed S_P can be adjusted and its effects studied.

First, from the results of the tests E and G it is modelled the temperature increase in the magnet cold bores. In a first level approximation:

$$\left|\frac{T_{(t)}}{T_{(t=0)}}\right|_{coldbore} = \left|\frac{P_{(t)}}{P_{(t=0)}}\right|_{test(B,G)}, \text{ where } T_{(t=0)} = 1.8\ \mathrm{K} \qquad (4.2)$$

The results of tests E and G don't show the exact same behaviour, this is due to the intrinsic and unique properties of each quench, and also the existence of oscillations.

For modelling purposes, the pressure oscillations were removed from the original curve, an average result was taken in consideration[21].

One way to validate that the simplifications made in model lead to accurate solutions is to reconstruct the results obtained in test F (scenario A1), having $P_{cb(t=0)} = 10$ mbar , a total $S_p = 60\ \mathrm{m^3/h}$ and $V_R = 0\,\mathrm{l}$, meaning that the pumps are

[21] - The curve used in the modelling is presented in Figure 4-12 (curve A0). First the oscillations existing in test E were removed using a simple moving average in the important region fit, and then the two results (tests E and G) were averaged, finally the result was scaled up by a 5% factor to overestimate the intrinsic behaviour of different quenches.

directly connected at both extremities of the cold bores. The conductance of the pipework plus valve C_1 was set to $500\ \mathrm{l/s}$.

It was also modelled the behaviour of the system having 2 pumps with the same characteristics as the ones available in the market for highest pumping capacity ($S_p = 65\ \mathrm{m^3/h}$) and hermeticity to ^{3}He (scenario A2). Figure 4-12 shows the results of the simulations.

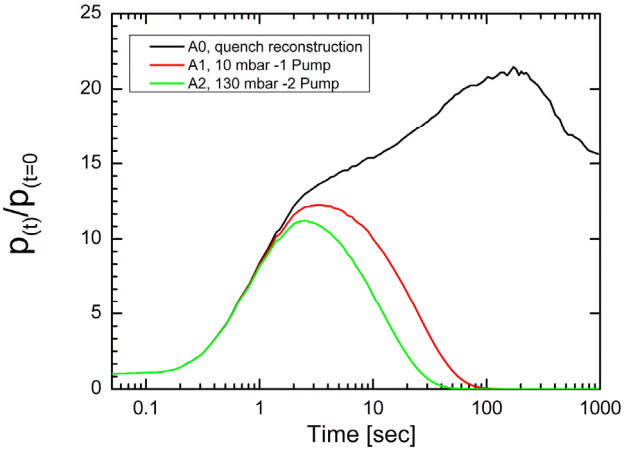

Figure 4-12: Reconstruction of the test conditions with model, A0 – represents the pressure increase in the cold bores using the results of tests E and G, A1 – It is the model result for the same conditions as in test F, A2 - is calculated for the same setup as in test F but this time with 130 mbar in the cold bores and higher capacity pumps (2x65 m^3/h).

It is shown a very good agreement between the results of the tests and the mathematical model A1. As for the scenario A2, it is shown that there is a very small advantage on having double pumping capacity directly connected to the cold bores, and that in any case, this expensive solution is still far from the desired pressure increase factor < 7.7.

The second step on the modelling, is to adjust the size of the reservoir, as to keep the pressure increase factor lower than 7.7. It is expected that, by having the cold bores directly connected to the reservoir, the evacuation is done more rapidly than by having active pumping.

The reasoning is that the conduction of the pipework is larger than the pumping speed of the pumps by a few orders of magnitude and thus there is an effective gain if the size of the reservoir is correctly dimensioned. Figure 4-13 summarizes these calculations.

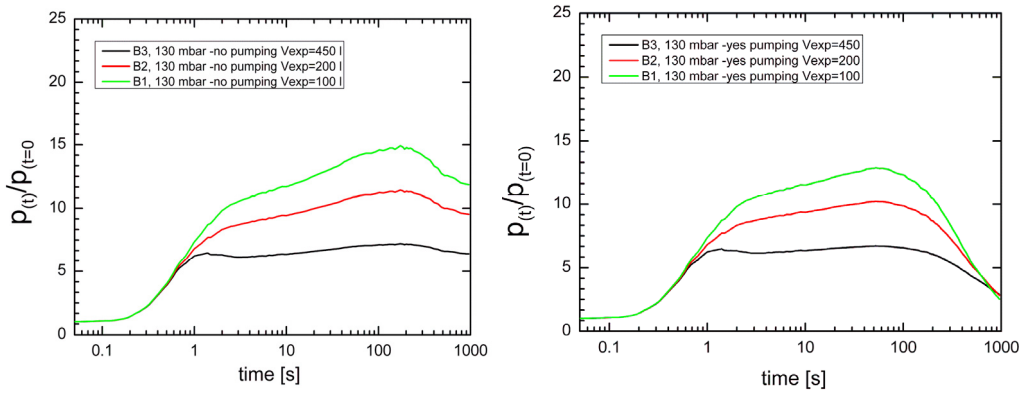

Figure 4-13: Pressure increase by connecting the cold bores to a reservoir with a volume of 100 l, 200 l and 450 l (Left). Pressure increase by connecting the cold bores to a reservoir with a volume of 100 l, 200 l and 450 l, plus active pumping with a 65 m3/h pump (Right).

It is shown that there is an effective gain with the introduction of a large reservoir connected to the cold bores. In scenario B3 with a reservoir volume V_R=450 l, the pressure increase in the cold bores is kept lower than the desired value of 7.7 throughout the quench evolution.

The introduction of an additional active pumping does not bring great advantages except for the high time scales.

Finally, we study the effect of the change in conductance of the pipework has on the evolution of the pressure for the scenario B3, keeping the reservoir volume set to 450 l. The results of this evaluation are summarized in Figure 4-14.

It seems that the conductance of the pipework only plays an important role on the behaviour or the pressure increase in the cold bores for the 'fast' warm-up time scale. The results show that for conductance values higher than 500 l/s there is a very little gain but, on the other hand, for smaller values it can cause the pressure to rise above the desired limit. This should be an important aspect to bear in mind for the design of the gas system pipework and choice of valves.

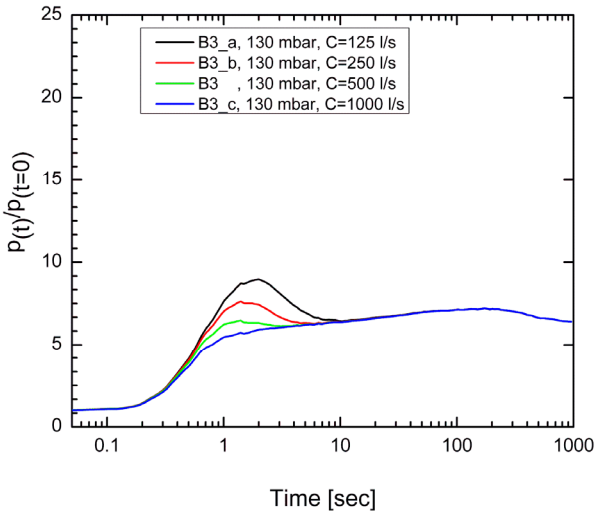

Figure 4-14:Pressure increase by connecting the cold bores to a reservoir with a volume of 450 l by changing the conductance of the pipework C1.

Measurements with gas extraction

The present section displays the results obtained after the completion of the final ^{3}He gas system.

In the design and construction of the ^{3}He system the guidelines from the previous simulations are implemented, i.e.:

- The necessity of having a reservoir (further called 'Expansion volume') of such dimensions that the total capacity to be larger than 450 l.
- The dimensions of the lines connecting the cold bores to the expansion volume were evaluated as to maximize the effective conductance.
- The use of fast opening valves where the total cross section should be attained in ~200 ms after the quench trigger.
- The option to start active pumping of the expansion volume, since there is no real gain for the limitation of the maximum attained pressure, but it can be interesting for the recovery of the gas.

Two provoked quenches at nominal magnet current (13 kA) served to verify that the implemented interlocks are fully operational, that the response of the system is within the desired threshold and that the pressure increase inside the magnet remains below the established initial goal. The results of these measurements are summarized in Figure 4-15.

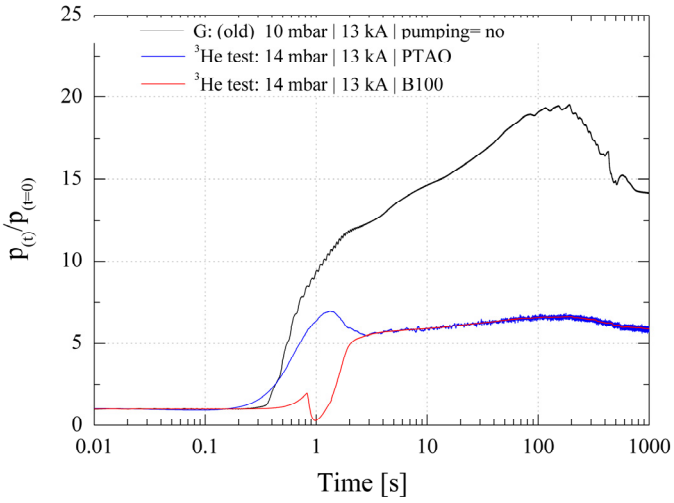

Figure 4-15: Pressure increase during provoked quenches with the final ^{3}He gas system. The pressure probes are placed in different regions. PTAO is placed directly inside the magnet cold bores. B100 is placed in the line linking the cold bore with the expansion volume.

The results of these tests show that that the initial goal was achieved and that the increase factor is kept below the desired value, it also shows a very good agreement with the results of the mathematical model.

4.3 Spontaneous Thermo-acoustic Oscillations

During the preparation for the quench tests described in the previous section the measured pressure in the cold bores has been shown to be unstable for some experimental conditions, what could naively be attributed to readout noise or instability, has shown to be an intriguing phenomenon, named spontaneous thermo-acoustic oscillations (TAO's).

A gas column inside a pipe with a steep temperature gradient along its axis can start to oscillate under certain conditions. In this section, a theoretical approach is given, followed by the description of the prejudicial influence of such an event on the detection of axions. Finally solutions how to avoid the occurrence of TAO's will be given and measurements of the occurrence and dampening of the phenomenon will be shown.

Theory

Sound waves in gas are commonly regarded as comprising pressure and motion oscillations, but temperature oscillations are also present, and when considering a solid boundary, heat transfer is also due to occur.

The research in thermo-acoustics has many roots, and in some cases invention and technology development has preceded fundamental understanding. Helmholtz [19] was the first to produce a numerical calculation of the dampening of acoustic waves due to friction, Kirchhoff [20] and Rayleigh [21] presented more complete equations describing the equations of motion of the dampening of the acoustic waves but still neglected effects of heat conduction to the tube walls.

Kramers [22] generalized the previous theory and quantified its effects in order to understand the problem that arose from cryogenics: when gas filled tubes spontaneously oscillate, a large heat transport occurs from room temperature to the cryogenic environment, disappointingly his results were far from agreement with the observations.

Nikolaus Rott [23][24][25] finally developed the mathematic equations that accurately predict the occurrence and extinguishing of oscillations which were later convincingly demonstrated experimentally by Yasaki [26].

The details of Rott formulations are very lengthy and therefore an outline of the main parameters to bear in mind will be given, considering its importance for the CAST purpose. The spontaneous TAO's occur as a consequence of the phase shift due to the heat transfer occurring in the Stokes boundary layer, which influences the pressure and the motion of the fluid.

The model assumes a long tube of length L, having a steep temperature gradient placed at length l_c, which defines two regions: the 'hot end' at temperature T_H and 'cold end' at T_C.

The hot end is closed and the cold end is open, or by geometric symmetry the problem can be defined as shown in Figure 4-16 with the hot ends closed and the symmetry plane as the cold end.

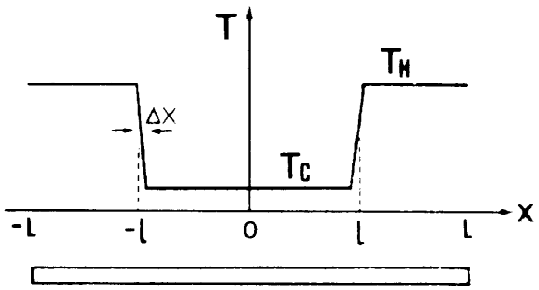

Figure 4-16: Temperature distribution along the tube axis, for the pipe closed on both ends.

The model assumes the following parameters:

$$\alpha = T_H / T_C \,, \tag{4.3}$$

as the temperature ratio and:

$$\xi = (L - l_C) / l_C = l_H / l_C, \tag{4.4}$$

as the length ratio.

But the existence of spontaneous thermally driven acoustic oscillations is far more complex, and has to obey to the stability criterion that is the main result of the model.

The stability curves derived from Rott depend on α and ξ, but also on:

$$Y_C = r_0 \cdot \left(\omega / \upsilon_C\right)^{0.5}, \tag{4.5}$$

the Stokes boundary layer thickness of the cold section, where r_o is the radius of the tube, ω is the frequency of the oscillation and ν is the kinematic viscosity.

From the model it is derived that each apparatus has its own characteristic natural frequency at which TAO's can occur, which is parameterized by $\lambda_C = \omega \cdot l_C / a_C$ where a_C is the acoustic speed.

The solution for the stability curves is first to find the dimensionless frequency λ_C, as a solution of $\cot(\lambda_C) / \lambda_C = \xi$.

The asymptote of the right-hand branch is given by:

$$Y_C = 2.382 \cdot \left(1 + \xi^{-1} + \lambda_C{}^2 \cdot \xi\right)^{-1} \cdot \alpha^{1.647}. \tag{4.6}$$

And the asymptote of the left-and branch given by:

$$\alpha = 0.228 \cdot \xi \cdot Y_C^{2.214}. \tag{4.7}$$

The later assumes the values $\gamma = 5/3$ for the specific heat ratio, $\sigma = 5/3$ for the Prandtl number, $\beta = 0.647$ the thermal expansion coefficient and $d = 0.0022$ for the Kramer's constant for helium.

The stability curves proposed by Rott for gaseous helium are presented in Figure 4-17.

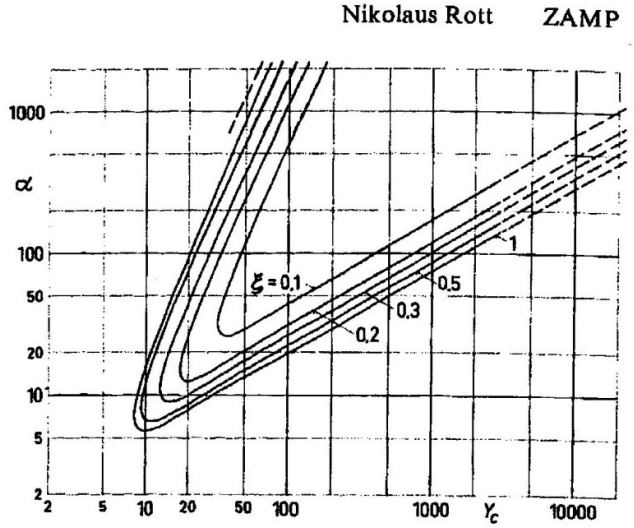

Figure 4-17: Stability curves for Helium [24]

The stability curves show a region enclosed by the left and right-had branches where spontaneous TAO's are due to occur and the region outside where oscillations are naturally dampened. The region of excited oscillations is wider for larger temperature and length ratios. The parameter Y_C is proportional to the tube diameter $2 \cdot r_0$ and to the pressure $\sim p^{0.5}$, thus by playing with all this variables TAO's can be dampened or spontaneous generated.

The CAST geometry can be compared with the model presented by Rott where the cold bore (from $-l$ to l) is maintained at T_C=1.8 K and two pipes of length l_H at both ends that connect to T_H (ambient temperature), thus resulting the CAST parameters as $\alpha \approx 162$ and $\xi \approx 0.2$, and by looking at the parameter space TAO's can occur for values of Y_C between $40 < Y_C < 2000$.

Solving the equations with the CAST parameters and assuming that the tube diameter is equal to the cold bore diameter through all the tube length (as for the model approximations) it is possible to calculate for which pressure of the buffer gas oscillations are due to occur. Results are presented in Figure 4-18.

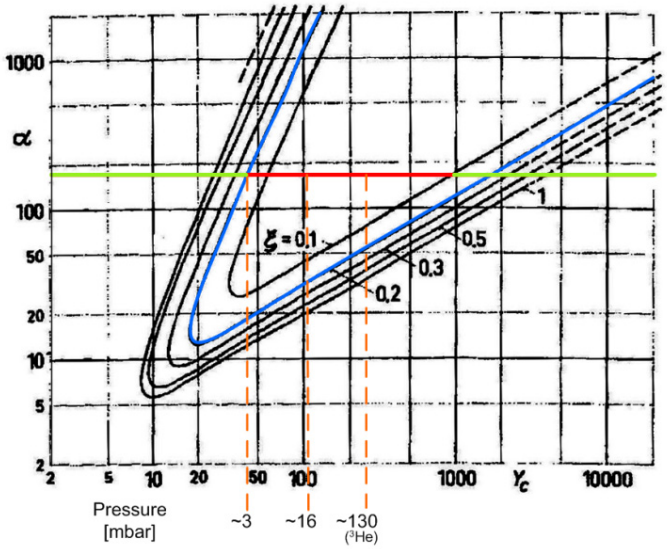

Figure 4-18: The CAST setup presented in the TAO stability space

It is also possible to compute the natural frequency of the oscillations in these conditions, resulting values of $\omega_1 = 24\ s^{-1}$ (or $f_1 = 3.77\ Hz$), dominated by the low acoustic speed in the cold end; these results entirely agree with the measurements done at CAST.

It is clear that for the CAST setup, thermo-acoustic oscillations are due to occur through all pressure range during the Second Phase of the physics experimental runs. Therefore, a study is necessary to evaluate possible effects, and if necessary the discussion of solutions as to eliminate TAO's.

Influence of TAO's on the axion-to-photon conversion

The maintenance of spontaneous thermo-acoustic oscillations during the experimental runs would ultimately convey density oscillations of the gas along the axion conversion region. The TAO's oscillate at a natural frequency f_1; the pressure

wave is a standing wave, stationary with axe of symmetry of the apparatus, thus having maximum amplitude at the warm ends. Neglecting the coupled temperature oscillation[22] by adiabatic expansion, it is possible to assume that the density oscillation is only coupled with the pressure, and thus one can write the electron density in a given time, in a given position along the magnet cold bores to be:

$$n_e\left(x,t\right)=n_e^0\cdot b_{(t)}\left[1+a\cdot\sin\left(2\pi\cdot f\cdot t\right)\cdot\cos\left(\frac{x}{L}\pi\right)\right], \tag{4.8}$$

Where n_e^0 corresponds to the pressure defined at the horizontal position of the magnet when the gas density is uniform (no oscillations) , or the average electron density along the axion conversion region, a is the ratio of the half-amplitude and the average density and f is the frequency of the oscillation of the electron density and $b_{(t)}$ is obtained from the requirement that the average electron density is equal to n_e^0 at any time given by:

$$b_{(t)}=\frac{\pi}{\pi+2r\cdot\sin\left(2\pi\cdot f\cdot t\right)}. \tag{4.9}$$

Thus, the axion conversion probability at $x=L$ (magnet length), averaged over the oscillation period $T=1/f$ comes,

$$P_{a\to\gamma}\propto\frac{1}{T}\int_0^T dt\left|\int_0^L dx\cdot e^{i\left\{q_1(t)x+b_1(t)\cdot\left[1-\cos\left(\frac{x}{L}\pi\right)\right]-i\frac{\mu}{2}x\right\}}\right|^2. \tag{4.10}$$

Using,

$$q_1\left(t\right)=\frac{a^2\cdot n_e^0\cdot b\left(t\right)-m_a^2}{2\cdot E_a}\text{ and }b_1\left(t\right)=\frac{a^2\cdot n_e^0\cdot b\left(t\right)}{2\cdot E_a}\cdot r\cdot\sin\left(2\pi\cdot f\cdot t\right)\frac{L}{\pi} \tag{4.11}$$

with $a=3.716\cdot10^{-11}\ \text{eV}\cdot\text{cm}^{3/2}$, $E_a=4.2\ \text{keV}$ and μ is the absorption coefficient for X-rays in the gas.

The calculations which are summarized in Figure 4-19, were made to see the effect of changing the amplitude parameter a (1%, 3% and 5%) for $f_1=3.77\ \text{Hz}$. The mean rate take over a time period (arbitrary units) is shown as function of the axion mass (eV) at an average pressure of 6 mbar at 1.8 K.

[22] - Other sources suggest the use of a less extreme scenario where the gas motion follows an isentropic path and the gas temperature is related with pressure via $(\gamma-1)/\gamma$.

The black line corresponds to the probability obtained with a uniform electron density along the magnet axis and the red line corresponds to the probability obtained with non-uniform density distribution (with thermo-acoustic oscillations).

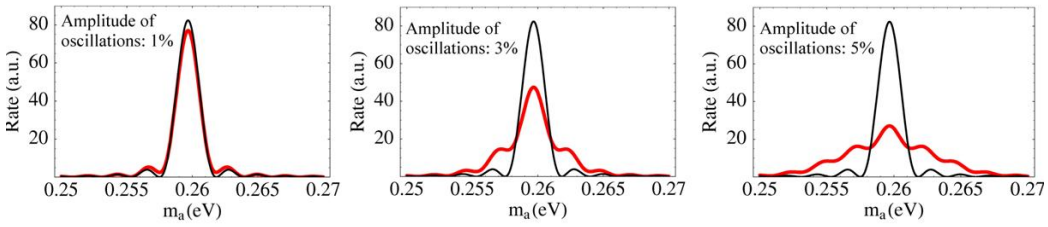

Figure 4-19: Influence of the amplitude of TAO's in the axion conversion rate. Three different scenarios are presented for increasing oscillations amplitude relative to the average pressure respectively, 1%, 3% and 5% (Calculations done by B. Lakic and M. Krcmar).

This simulation shows that when thermo-acoustic oscillations occur, there is a resulting reduction on the axion conversion rate which is proportional to the amplitude of the oscillations. With density oscillations of a relative amplitude of 5%, the maximum axion conversion rate for the axion mass for which the coherence is maximized, is reduced almost 60%, although with an important increase to adjacent masses.

This result is very interesting: in one hand, with the occurrence of TAO's, there is a loss for the axion discovery potential, but in the other hand the conversion rate broadens to larger axion mass ranges.

In order to maximize the axion discovery potential the CAST Collaboration decided that the TAO's should be eliminated, if possible, which also has as advantages the reduction of fatigue stresses on the cold thin X-ray windows film due to vibrations, the reduction of heat flux into the magnet which ultimately could cause a quench, and the improvement of measurements of such as temperatures and pressures of the gas and adjacent regions.

Solutions

The methods to eliminate TAO's can be easily defined by understanding the parameters that play a role in the stability curves, for instance a smaller length ratio ξ defines narrower excited oscillations zone, whilst reducing the temperature ratio α reduces the Y_C range where TAO's can be empowered, and lower pressures or tube

radius create an horizontal shift inside the parameter space. If this analysis look simple, practical ways can become hard to achieve.

To move horizontally inside stability parameter space can only be done by changing the pressure value, since the tube radius is a intrinsic property of the CAST setup (the radius of the cold bores), and because the goal is to avoid TAO's through all the available pressure range, there is nothing that can be done in this regard. Thus, dampening solutions can only be achieved by adjustment of properties α and ξ or in other words, regulating any of the parameters, T_C, T_H, l_C or l_H.

The temperature of the cold end T_C and l_C cannot be changed since they are defined for the CAST case as the temperature of the magnet (1.8 K), and magnet length[23] ($2 \cdot l_C$). Thus the possibility to dampen TAO's becomes now restricted to only two properties, T_H and l_H, which are inter-related. A solution can be achieved by having an efficient blockage of the flow at a colder region than that the original T_H (room temperate).

In reality this is not that easy to achieve, because this requires the introduction of cold elements inside the pipework able to efficiently block the flow, but in the other hand from the results of section 4.2 it comes out as a guideline, that the conduction should be maximized as to enhance the gas extraction in case of quench.

To overcome this limitation, during the ^{4}He gas phase where the maximum pressure reached during a quench event is lower than 300 mbar, there is no need for gas extraction, and therefore permanent TAO's dampers will be inserted in the pipework.

For the ^{3}He gas phase when the rescue of the gas is required during the quench, the solution is achieved with the integration of cryogenic valves in the cold part of the circuit that can be opened or closed to allow the gas flow.

The permanent TAO dampers have to be located as cold as possible, but not limiting the optical acceptance of the cold bores, the design of these dampers had to bear in mind not only the very limited space for the mounting but also its performance. The dampers consist of 1 m long and 3 cm wide multilayer super-insulation band, made of five 6 μm aluminized mylar and kapton thin sheets, wrapped together to form a compact cylindrical plug to fill the tube cavity (see Figure 4-20).

[23] - For numerical calculation purposes it is used 2*l* as the length of the cold tube, cooled by the superfluid helium at 1.8 K (10.254 m), which is slightly longer than the defined magnetic length (9.260 m).

The damper is placed inside the pipe that joins both cold bores which then connects to the room temperature pipework. The temperature in this region is expected to be $\sim 70\ \mathrm{K}$ (with windows temperature maintained at 120 K). This new setup completely changes the characteristics to TAO's, now with $\xi < 0.03$ defining a much narrower excited oscillation zone and $\alpha < 68$, whereas for working pressure range it is running below the stability limit.

Figure 4-20: Left: Scheme with the position of the TAO dampers relative to the magnet face and the cold X-ray windows. Right: Photo of the TAO damper.

Measurements

During the preparations for the provoked quenches tests the magnet cold bores were filled with ^{4}He gas at different pressures. It was noticed that pressure instabilities (later caller spontaneous thermo-acoustic oscillations) would occur for pressures higher than ~3 mbar.

A data acquisition setup was put in place to measure the shape of the pressure instability in order to make a discrete analysis of the components of the oscillation. The DAQ relies on a National Instruments PCI card for high sampling rates (250 kS/s for analogue inputs with 16 bits) and a fast readout.

During these tests, the cold bores were connected to the room temperature pipes, thus having favourable conditions for the occurrence of TAO's, due to the high temperature ratios and length ratios (see Figure 4-18). In Figure 4-21 it is shown the pressure wave shape and the Fourier transform showing several harmonics that are multiple of the natural frequency at ~3.7 Hz, multiple harmonics have been observed by Yazaki [27]

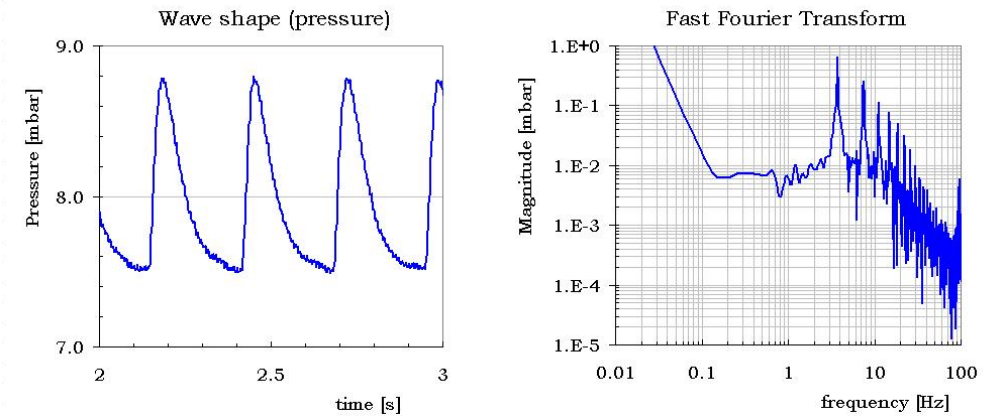

Figure 4-21: Left: Wave shape of the pressure oscillation due to the TAO's. Right: Fourier transformation of the pressure wave signal showing the characteristic frequencies.

Later the TAO dampers were inserted inside the cold bores connected pipes, and pressure oscillations could not be measured. Figure 4-22 shows the results of those measurements where no TAO's are observed and where the electrical pick-up noise can be easily identified.

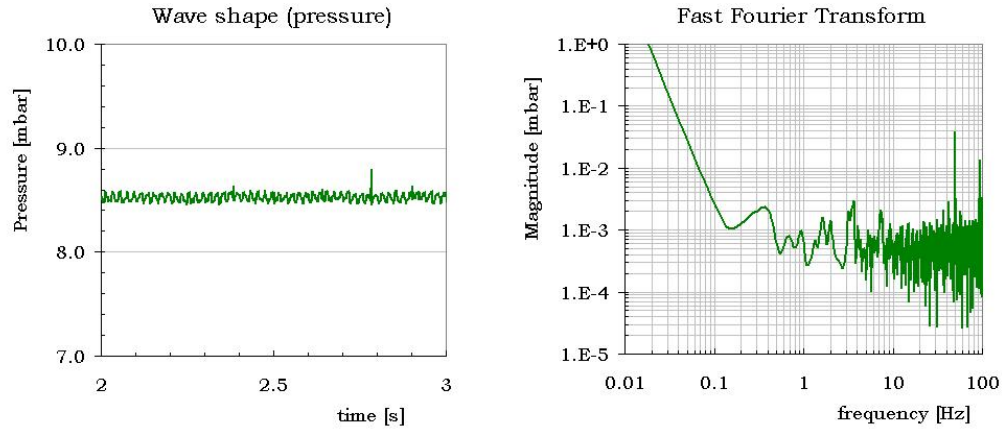

Figure 4-22: Left: Wave shape of the pressure signal in absence of TAO'. Right: Fourier transformation of the pressure wave signal showing the characteristic frequencies mainly due to electric noise.

The full control of TAO's occurs after the complete installation of the ^{3}He gas system where the TAO's are eliminated by the installation of remotely operated cryogenic valves, these isolate the cold part from the warm part, moreover the temperature of the windows can be regulated redefining the temperature ratio α . In

addition, miniature cryogenic pressure transducers are installed directly inside the cold bores allowing the monitoring of the pressure on both the cold part and the warm part.

4.4 Vacuum spikes with vertical movement

The cold X-ray windows are a thin interface between the buffer gas and the vacuum system leading to the detectors, where one of the main parameters to be maximized is the transmission of X-rays with energies up to 10 keV.

A good vacuum level is therefore required so that the number of absorbed photons is minimized. Moreover other technical aspects require high vacuum levels such as for the efficient behaviour of the X-ray mirror system (see section 2) or for cryogenic safety reasons, due to the temperatures that are achieved inside the cold part of the vacuum system, which is thermally clamped with the magnet thermal shield (70 K) and connects to the cold windows.

Although each detector has its own pumping station and careful leak-testing is done, the vacuum levels could be improved, and since the X-ray windows are positioned between the vacuum system cold thermal clamp and the magnet, the temperature of the windows is due to become the coldest point of the vacuum system.

After the installation of the final cold windows and the magnet cooled down, the cold X-ray windows were observed through the cold bore apertures; surprisingly it was observed that dark spots appeared in the cold window film (see Figure 4-23).

This astonishing observation caused great concern, meaning a possible loss of transmission or even contamination with oil vapours from pumps. The most plausible idea assumes that the vacuum gases are being released from surfaces on the vacuum side of the windows are being cryo-pumped onto the window foil, thus forming a layer of condensed residual gases that are trapped due to the low temperatures below the vapour pressure.

Although the source of the problem can be reduced by means of improving the vacuum levels (via a more powerful pumping of the vacuum or improvement on the tightness of the gas detectors, etc.), other measures can be taken to reduce the amount of gases that accumulate onto the windows foil or even to allow the removal of the accumulated gases.

The solution passes by a temperature increase of the X-ray cold windows, thus avoiding it to become the coldest point of the vacuum system. Ultimately, to remove condensed gases, the windows temperature should be increased above the vapour pressure of the residual gas constituents and the released gases should be actively pumped.

Running the windows warmer has, in the other hand, consequences for the amount of heat that the cryo plant has to cope with for cooling the magnet, since the windows are thermally coupled with the liquid helium coolant by conduction through the pipe walls and convective currents in the buffer gas occurring at the extremities of the cold bores.

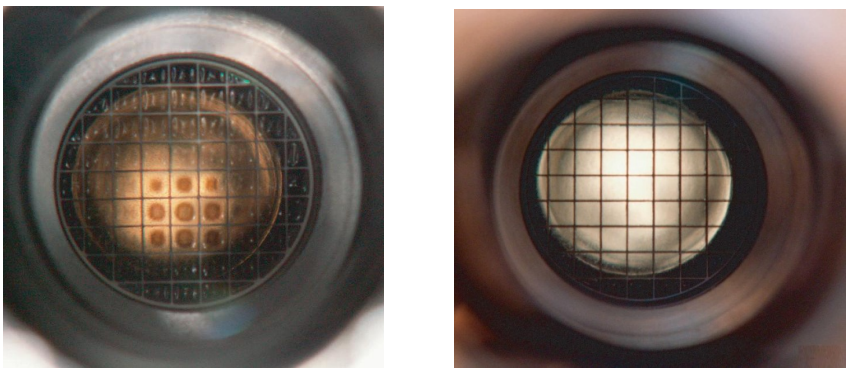

Figure 4-23: Pictures of the cold thin X-ray window visible through the cold bore aperture on the MRB side by shining a light source from the back. Left: Dark spots of accumulation of frozen gases visible on the window foil; Right: Window is optically transparent (no dark spots) after a temperature increase up to 200 K.

Vacuum spikes were measured during the vertical movement of the magnet. These seem to be correlated with the enhancement of convective currents at the cold bore extremity which is lowered.

A mass spectrometer was installed coupled to the vacuum system which allowed the partial pressures of the vacuum constituents to be measured. During the warm-up of the windows the gases that have been accumulated onto film are baked and by looking at the concentrations of the different constituents one can evaluated its origin.

Molecular surface pumping

Surfaces cooled at sufficiently low temperatures can provide molecular gas pumping (cryo-pumping) due to weak Van der Waals attractive forces. The sojourn time of molecules adsorbed on a surface is given by the Frenkel equation $\tau = \tau_0 \cdot e^{E/RT}$, with E

the energy of vaporization, R the universal gas constant and T the surface temperature. The energy of vaporization for different gases is given in Table 4-4.

Element	He	H_2	Ne	N_2	CO	Ar	O_2	CH_4	Kr	Xe	CO_2
Energy of vaporization	0.020	0.215	0.431	1.333	1.444	1.558	1.630	1.995	2.158	3.021	4.043
$\tau_{(70\,K)}/\tau_{(300\,K)}$	$1{\cdot}10^{0}$	$3{\cdot}10^{0}$	$1{\cdot}10^{1}$	$1{\cdot}10^{3}$	$3{\cdot}10^{3}$	$6{\cdot}10^{3}$	$8{\cdot}10^{3}$	$6{\cdot}10^{4}$	$2{\cdot}10^{5}$	$2{\cdot}10^{7}$	$5{\cdot}10^{9}$

Table 4-4: Energy of vaporization for different gases.

For a given gas and surface temperature, the progressive increase of the surface coverage leads to a saturation equilibrium between the gas adsorption and desorption.

Figure 4-24 shows the saturated vapour pressure curves for the most common gases. These curves indicate that most gases exibit a vapour pressure not higher than 10^{-6} mbar at 30 K (except for helium, hydrogen and neon).

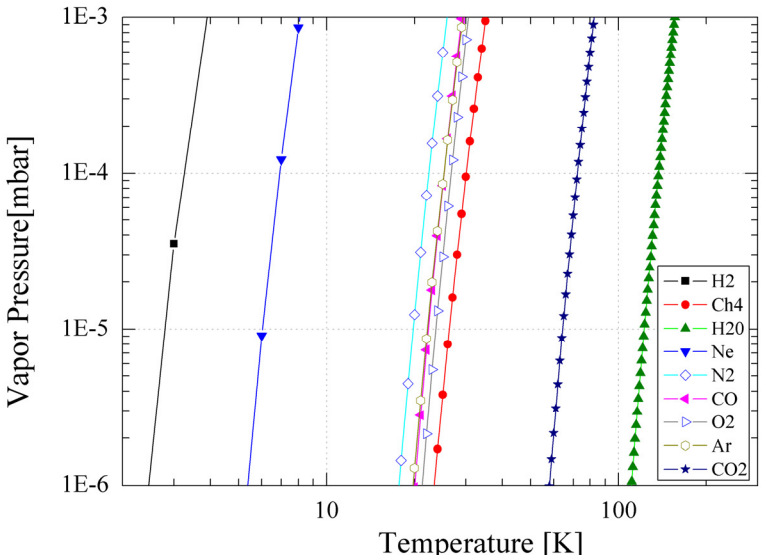

Figure 4-24: Vapour pressure of the most common residual gases present in vacuum systems

The cold X-ray windows being the coldest point of the vacuum system (except when higher than the thermal clamping region set at ~60 K), they act as a pump where the sojourn time is high due to its low temperature, and where residual gases will have more probability to condense.

Residual Gas Analysis

In order to identify the gas species that constitute the vacuum environment it is used an analytical technique called Residual Gas Analysis.

Residual gas analyzers operate by creating an ion beam from samples of the gas being analyzed. The resulting mixture of ions is then separated into individual species through their charge-to-mass ratios.

The output of a RGA is a spectrum that shows the relative intensities of the various species present in the gas, or by scanning the different species over a period of time one can create a partial pressure evolution of the different species for a given time frame.

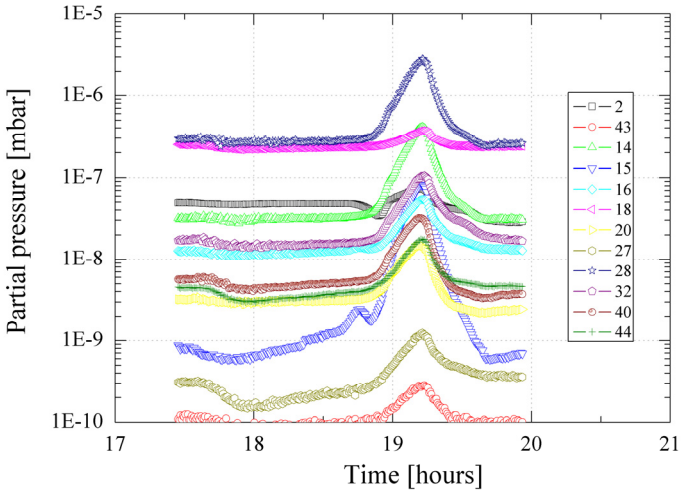

Figure 4-25: Residual gas analysis during the vertical movement of the magnet. The different species are represented by its atomic mass number.

Figure 4-25 shows the result of residual gas measurement performed in the CAST vacuum system during the magnet vertical measurement. It shows that when the magnet extremity is moved vertically upwards, it is noticed an important increase for some gas species, mainly:

- a.m.u. 28 (mainly N_2 + some concentration of CO)
- a.m.u. 18 (mainly H_2O)
- a.m.u. 2 (mainly H_2)
- a.m.u. 14 (mainly N_2 break)
- a.m.u. 32 (mainly O_2)

This type of composition is usually present in unbaked vacuum systems, where a small air leak is present. Although the size of the contamination is small in order to have an impact on the vacuum system interlocks, the accumulation of frozen gases in undesired regions is to be minimized and therefore proves the necessity of further improvements in the vacuum system requirements.

Although the CAST vacuum system is not physically a part of the gas system, in order to avoid residual gases from the vacuum system to be cryo-pumped onto the cold X-ray window foil with a possible reduction on the X-ray transmission, some possible solutions can be implemented on the gas system side.

A virtual solution would be to run with the cold window at a temperature higher than that of the vapour pressure of the main gases, but that would require impractically high temperatures <150 K, which would not only create high heat loads on the already charged magnet cryo-plant and a higher risk for quenches, but also large convectional currents on the cold bore extremities and also an increase of the ^{3}He diffusion through the cold window film resulting on a loss of precious gas.

The solution passes by a regular bakeout of the cold X-ray window during non running periods, by bringing the window temperature above the vapour pressure of the main constituent gases, and monitoring the amount of the released cryo-pumped gases by measuring the pressure increase.

5 The provisional ^{4}He gas system

The provisional ^{4}He gas system is built for the initial physics runs, after CAST First Phase with vacuum inside the magnet cold bores. The goal of this system is, by using ^{4}He as conversion medium, to explore the axion conversion limits up to the vapour saturation pressure of the gas, and gather vital information for the construction of the final and more complex gas system.

In this section the design of the ^{4}He gas system is reported, along with the operation modes, data taking overview and results.

5.1 Temperature measurement and control

A good temperature measurement allied with a data acquisition system is an important feature when the possibility to analyze thermal effects is desired. Important measurements such as temperature stability or transients can be a good indicator for heat flux at a given position or appearance of new phenomena. It is thus of great interest to have a good and reliable indicator of the buffer gas temperature in different possible positions of the gas system.

Since the gas system extents from room temperature regions down to cryogenic temperatures, those being maintained due to the magnet liquid helium cooling (1.8 K), in order to make reliable temperature measurements the choice of the appropriate sensing elements becomes essential.

Various important aspects have to be taken in consideration for the choice of the sensing elements: such as the operating temperature range, environment variables (magnetic field, external heat input, and electric noise), accessibility and solutions of good thermal clamping.

In order to maximize the quality of the measurement, the thermal heat load brought by parasitic heat sources has to be minimized, like conduction heat brought through the sensor wiring or heat radiated from other surfaces.

The reasons stated above show the great difficulty to have a direct measurement of the gas temperature. To overcome this constrain indirect measurement of the gas temperature can be made by positioning the temperature sensors on the surfaces in contact with the gas. In a steady state regime the temperature of the gas is similar to that of the surrounding element.

The quality of the measurement is then enhanced by a good thermal contact between the sensor and the surface by using glue and/or grease. The thermal clamping of the sensor with the surface is maximized by reducing the heat flux brought along the measurement wires by adding several contact points along the measurement wires with the surface, and finally the thermal radiation from the surroundings is minimized using thermal shields. The choice of sensors requiring low electrical excitation currents is also very important to limit the energy dissipation by Joule effect.

The choice of temperature sensors and instrumentation amongst the large variety of commercially available sensors falls mainly in the design operating temperature range, and the desired accuracy of the measurement.

The typical characteristics of cryogenic temperature sensors used at CERN [28] is summarized in Table 5-1. For the gas system it was decided to go for an 'hybrid' solution where a given type of sensor is used depending of its location.

The TVO® carbon-ceramic resistor (TVO®) works on a useful temperature range from 300 K down to 1.6 K, it offers excellent performance and stability characteristics under magnetic fields.

The Cernox^{TM} (Cx^{TM}) thin film resistance temperature sensors work on a temperature range similar to that of the TVO® while having a lower response time, but in terms of resistive values is the one with the largest span (3 decades).

Platinum resistance thermometers (PT) are an excellent choice for use as cryogenic temperature sensing devices above 30 K, due to its low cost, but below this temperature its sensitivity drops and therefore is usually used in combination with other to cover the full temperature span down to 1.8 K.

	Temperature span [K]	*Resistance Span [Ω]*	*dR/dT [Ω/K]*	*(dR/R)/(dT/T)*
Cernox	1.6 → 300	30000 → 30	-40000 → -0.1	-2.7 → -1.0
TVO	1.6 → 300	9000 → 900	-7000 → -0.7	-1.3 → -0.2
Platinum	70 → 300	18 →110	-0.4 → +0.4	+2.0 → +1.0

Table 5-1: Typical characteristics of cryogenic temperature sensors used at CAST

A resistive temperature sensor changes its electrical resistance depending on the temperature, thus the basic measurement principle is to send a constant current over a pair of wires and reading the output voltage developed at the resistor leads, via another pair of wires. Using a 4-wire technique the effect of the cable resistance is ignored.

The temperature sensors are installed inside the CAST cryostat and thermally clamped to the pipework. The chosen regions for placement are the cold X-ray windows and the connecting pipework to the cold bore where high temperature gradients are due to occur. Figure 5-1 shows the regions inside the cryostat where the temperature sensors are placed.

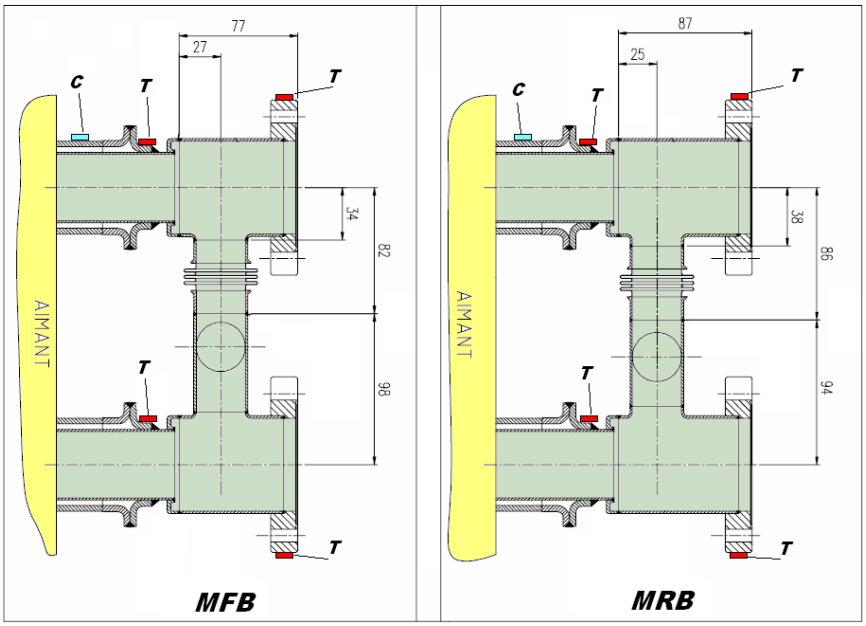

Figure 5-1: Location of the temperature sensors inside the CAST cryostat (top view). 'C' stands for Cernox® type and 'T' for TVO® type temperature probes.

The temperature probes are clamped to the surfaces with glue plus tightening braces. In order to avoid that any external heat load is brought through the sensor wiring influencing the measurement, the wire pairs are thermally clamped to the surface. Finally and to avoid any additional heat load brought by radiation, the region is thermally shielded with multi-layer insulation.

With the goal to minimize electromagnetic interference the wire pairs as twisted.

In order to control the temperature of the different regions, heaters are installed on boundaries with external heat sources. One of those regions is the cold X-ray window flanges, which is the interface between the gas system and the vacuum system.

Another region is the linking tube to the room temperature part of the gas system. The thermal clamping to those regions is done with custom made supports, braces and braids made in high purity copper to enhance thermal conduction (as shown in Figure 5-2).

This configuration allows the temperature of each individual region to be regulated, by adjusting the power supplied to the heaters.

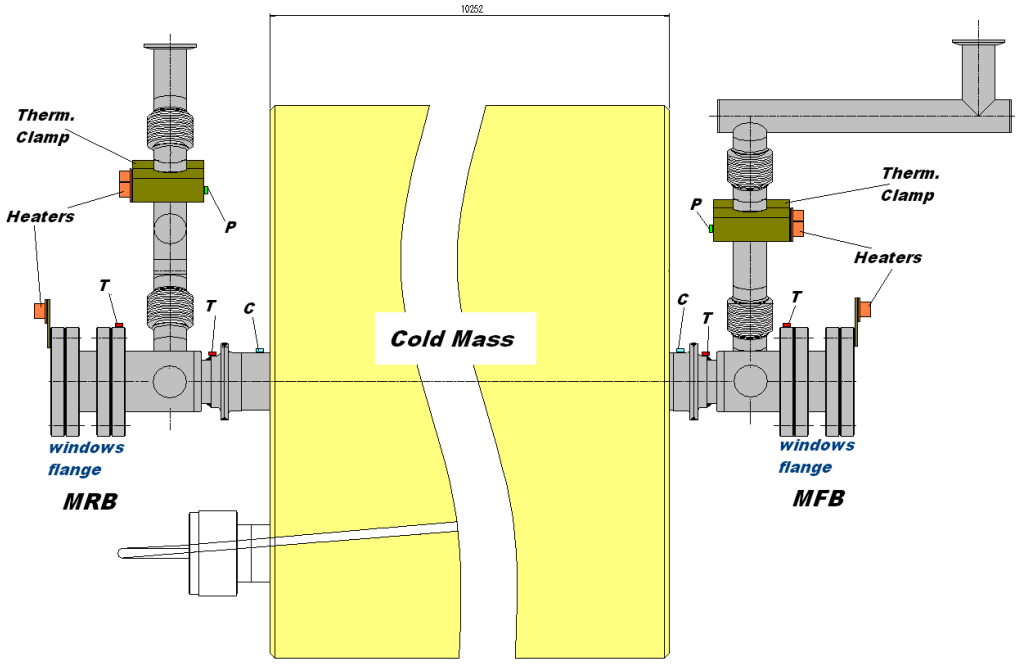

Figure 5-2: Picture showing the positioning of the heaters and the thermal clamping (side view). 'C' stands for Cernox® type and 'T' for TVO® type temperature probes

In total there are 4 heaters, 2 platine thermometers, 2 Cernox® thermometers and 4 TVO® thermometers.

The regulation of temperature on the cold X-ray windows flanges is necessary in order to avoid gases from the vacuum system to be cryo-pumped onto the foil and also to perform periodical bake-outs.

One undesired consequence of controlling the temperature is the additional heat load drawn to the superconducting magnet, which not only increases the potential for undesired quenches, but also brings additional heat load which has to be extracted via the cryogenic plant for magnet cooling.

Despite these limitations, the temperature control is an additional feature which can become of great advantage in some scenarios, such as for bake-out of cryo-pumped gases onto the cold X-ray windows or adjust parameters for dampening TAO's.

5.2 Gas Pressure measurement

The gas pressure is one of the thermodynamic properties that need to be known in great detail for the correct calculation of the electron density in the cold bores. For that reason a market survey was done to evaluate possible pressure sensor adapted for our application.

The MKS Baratron 690A (absolute pressure sensor) is a capacitance diaphragm sensor combined with solid state electronics used in metrology environments.

Capacitance sensors belong to a class of vacuum pressure gauges that read pressure directly by measuring the deflection of a tensioned diaphragm. When designed for absolute pressure measurements, one side of the diaphragm is exposed to the pressure to be measured and the other is evacuated to a reference low pressure.

The difference in pressure causes the diaphragm to deflect toward the reference pressure side, and the curvature of the diaphragm is sensed by two capacitance plates consisting of metal films on a ceramic substrate, forming two concentric rings. As the diaphragm deflects, both electrodes sense a change in capacitance, by differing amounts. The difference is sensed by a capacitance bridge circuit and converted to a DC voltage output.

This type of construction has the advantage that the indicated pressure is independent of the composition of the gas that is being measured and also a good accuracy throughout a wide range of pressures, unlike ionization gauges.

As a result, a capacitance gauge only needs to be calibrated with one gas to accurately reflect the total pressure for all gases and mixtures.

By housing the sensor head in a temperature controlled shell, temperature effects are dramatically reduced and the accuracy is improved to as high as 0.05% of the reading. Table 5-2 summarizes the specification of the sensors used:

Pressure Range	Resolution	Precision % of Reading	Useable Measurement Range	Temperature Coefficient		Max. Line Pressure	Operating Temp. Range (ºC)
(torr F.S.)	(of F.S)	(± T. coef.)	(F.S. to)	Zero (F.S. ºC)	Span (Rdg. ºC)	bar	Regulated
100 /1000	1×10^{-5}	0.05	1×10^{-5}	4 ppm	20 ppm	3.1	to 45 ºC

Table 5-2: Characteristics of the Baratron® pressure sensor.

For the maximization of the absolute accuracy of the instrument, two different units were purchased and installed in sections which will be operating at different pressures.

The further mentioned B-100 and B-1000 are both Baratron® pressure sensors with a full scale of 100 and 1000 torr respectively. The B-1000 type sensor is measuring the gas pressure in the metering volumes and the B-100 is measuring the gas pressure inside the cold bores.

The pressure sensor mount comes with vibration dampeners to reduce the structural vibration coming from the magnet movement that might reduce the pressure measurement sensitivity. The orientation of the pressure sensor mounting is set to have the sensor axis placed horizontally and parallel to the magnet vertical movement axis. In this way pressure measurement is unaffected by the vertical position of the magnet.

5.3 Thermo-acoustic oscillations measurement

With the goal of monitoring the absence of TAO's a cryogenic pressured transducer made by Kulite® (Figure 5-3) has been directly introduced inside the cold bore region. The damping of TAO's is assured by two sets of thermo-acoustic oscillations dampers placed inside the tubes that link the cold bore to the room temperature region, as previously described in Section 4.

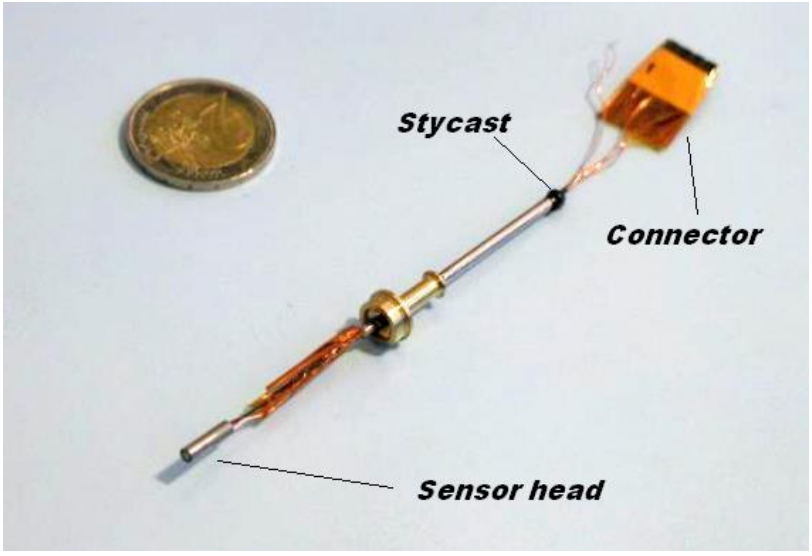

Figure 5-3: Picture of the miniature pressure transducer for absence of TAO's monitoring and picture of custom feed through.

This absolute pressure transducer is based on a full active 4 arm Wheatstone bridge, dielectrically isolated silicon on silicon.

Although the operating temperature of this component is guaranteed from 120 ºC down to -195.5 ºC, the sensor can still be used for lower temperatures.

The absolute accuracy of such sensors is low (mainly because of its drift with temperature), nevertheless due to its high natural resonant frequency of the sensor (typically 240 kHz) which has a much larger bandwidth than that of the TAO frequencies (few Hz), these sensors allow one to monitor and identify possible oscillations (with minimum amplitude ~0.01 mbar).

The sensor is fed by 10 VDC low noise voltage supply from SRS®, and the readout of the 100 mV (for a full scale at 1.7 bar) is done by a low-noise pre-amplifier by SRS®.

The position for placement of this miniature pressure transducer had to be studied carefully, in order not to obstruct the effective cold bore aperture seen by the detectors.

For this reason, it was placed on the MFB side of the magnet in the 77 mm length straight section of tube of 63 mm diameter (magnet cold bores are 43 mm diameter). This gives a margin of 10 mm for the sensor head to be immersed in the gas.

The custom made hermetic feed-through was fabricated in Cryolab; Figure 5-4 presents its dimensions.

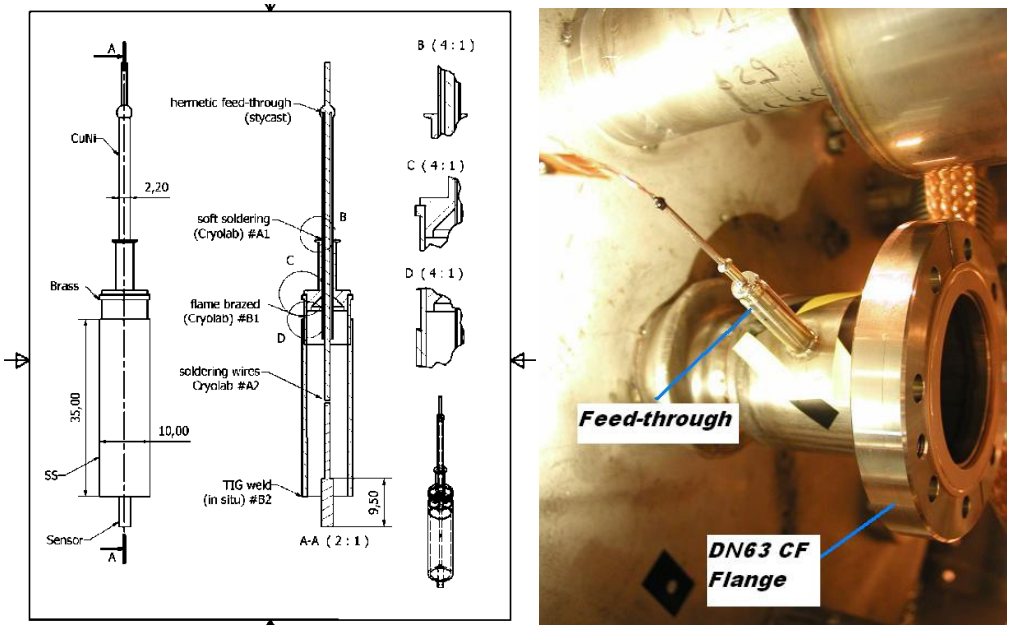

Figure 5-4: Custom made hermetic feed-though for miniature cryogenic pressure transducer. Right: Design drawing and dimensions. Right: Photograph of the sensor positioned inside the cryostat.

The design was optimized to minimize the number of welds made in-situ due to severe space limitations. The main difficulties to assemble this component occur during the brazing and soldering phases due to the need to reduce the amount of heat brought to the sensor wiring, due to its miniature dimensions.

5.4 Data Acquisition and Monitoring

All the signals brought from the various sensors are routed to one dedicated rack placed in the experimental hall ground level. Since during the physics runs the magnet performs a horizontal and vertical movement around the pivoting point, the routing of the cables coming from both extremities of the cryostat had to be studied to avoid interference between moving and static parts that can endanger the integrity of the cables and ultimately the loss of the signals.

Commercial hermetic feed-troughs are used for all electrical signals that need to be extracted from the interior of the cryostat vacuum. These are prepared and tested prior to the installation in the cryostat. The feed-troughs allow an easy disconnection for testing the signals and have 40 “Burndy” numbered pins for easy referencing.

All the signals coming from each side of the cryostat are comprised in two multi-conductor screened cables of 24 twisted pairs each, for minimization of electromagnetic interference from external sources.

A dedicated 19” rack hosts all of the read-out electronics, display units and power supplies. Table 5-3 summarizes the existing equipment:

Item nr.	Un. x Device	Description
Thermometry		
1	1 x AVS-47	Picowatt AC Resistance Bridge
2	1 x AVS-47IB	Picowatt Preamplifier
3	1 x AVS-47B	Picowatt Computer Interface (IEEE488)
4	2 x LogTherm	Cernox signal conditioner
Pressure Measurement		
4	2 x MKS 670B	MKS Baratron Signal Conditioner

5	2 x SR560	SRS Low-noise voltage preamplifier
6	2 x SIM928	SRS Isolated Low-noise voltage source
Power Supplies		
7	2 x HM 8142	Hameg Power Supply for heaters

Table 5-3: Equipment on DAQ 19" rack

Data acquisition and monitoring is carried out in a dedicated computer via two National Instruments® (NI) PCI cards.

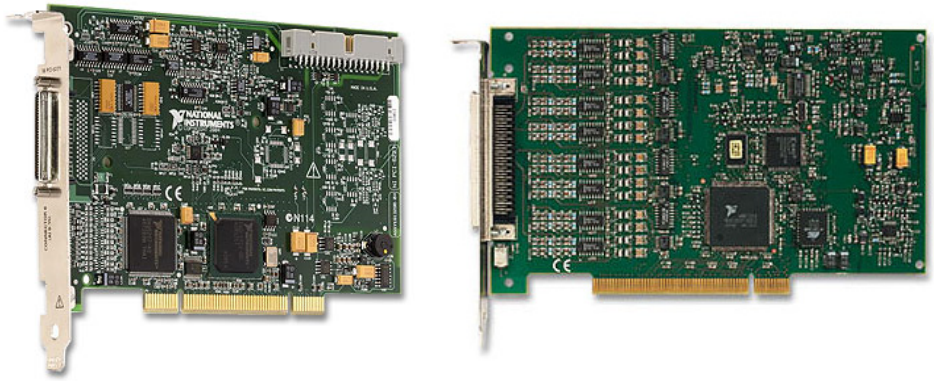

Figure 5-5: Data acquisition boards: NI PCI-6221 (left) and NI PCI-4351(right)

The NI PCI-6221 card is a 16 bit resolution board with a fast sample rate of 250kS/s, equipped with 16 analogue inputs and 4 analogue outputs. It is optimized for cost-sensitive applications where fast sampling is required. It is used mainly for fast measurements such as the pressure evolution during a quench or to evaluate the existence of TAO's.

The second card a NI PCI-4351, is a 24 bit high-precision data acquisition board, comprising 16 differential analogue inputs that can be read up to 60 readings per second, plus 8 digital I/O lines. This card is used for all 'slow' precision measurements such as pressures on the metering volumes and some temperatures (CERNOX).

The online monitoring is displayed in customized Labview® programs, which are designed for a rapid assessment and evaluation of the quantities to be measured. Depending on the cases, it can also perform calculations of quantities of interest, such as

the amount of moles transferred or pressures to be achieved at the end of a given procedure.

Let us now assess individually the distinctive acquisition hardware which composes the rack and its related customized software that was developed for monitoring the measured quantities.

The Picowatt AVS-47 is a versatile, precision AC bridge offering high performance for resistance measurements in a wide dynamic range from milliohms to megaohms. This instrument is ideally suited for measuring resistance thermometers commonly used at ultra-low temperatures.

Figure 5-6: Photograph of the Picowatt AVS-47 resistance bridge

The latest developments to this instrument have improved the screening of high frequency interference thus improving its overall sensitivity. This has been further enhanced by the addition of a separate pre-amplifier unit which is connected directly to the electrical outputs on the insert top plate (AVS47-IB). This reduces the length of the sensor cables and sensitivity to electrical pick up.

The bridge operates at excitation frequencies of 12.5 and 15 Hz for mains frequencies of 50 and 60 Hz respectively. The alternating excitation eliminates any thermal voltages. A square wave excitation is employed to minimize linearity errors.

In order to keep with the noise reduction philosophy, the computer interface is divided in two parts. The first part is a low-speed primary interface that doesn't contain any digital intelligence which is placed inside the AVS47B. The second part is external secondary unit (AVS47-IB) and uses IEEE-488 (GPIB) computer interface for being a fast and notorious interface standard in scientific instruments.

The original Labview® driver provided by the supplier was modified in order to comply with our specific use. It consists of a graphical user interface (GUI) comprising an initial configuration panel and the acquisition panel.

In the configuration panel (see Figure 5-7) the instrument GPIB address is specified, together with the length of data set to be displayed and the path to where the data is to be stored. Here the name for each individual channel is given and a specific temperature sensor calibration curve can be assigned.

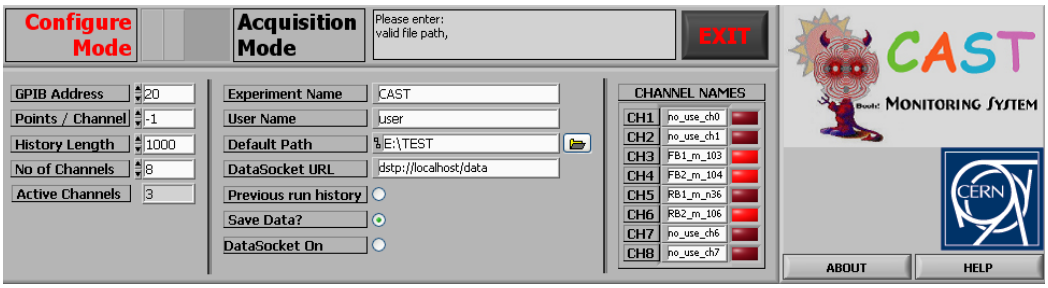

Figure 5-7: Configuration panel of the AVS47 driver

In the acquisition panel (see Figure 5-8) it is set the order for which the multiplexing of the different channels is done, together with the number of stabilization cycles before advancing to the following channel.

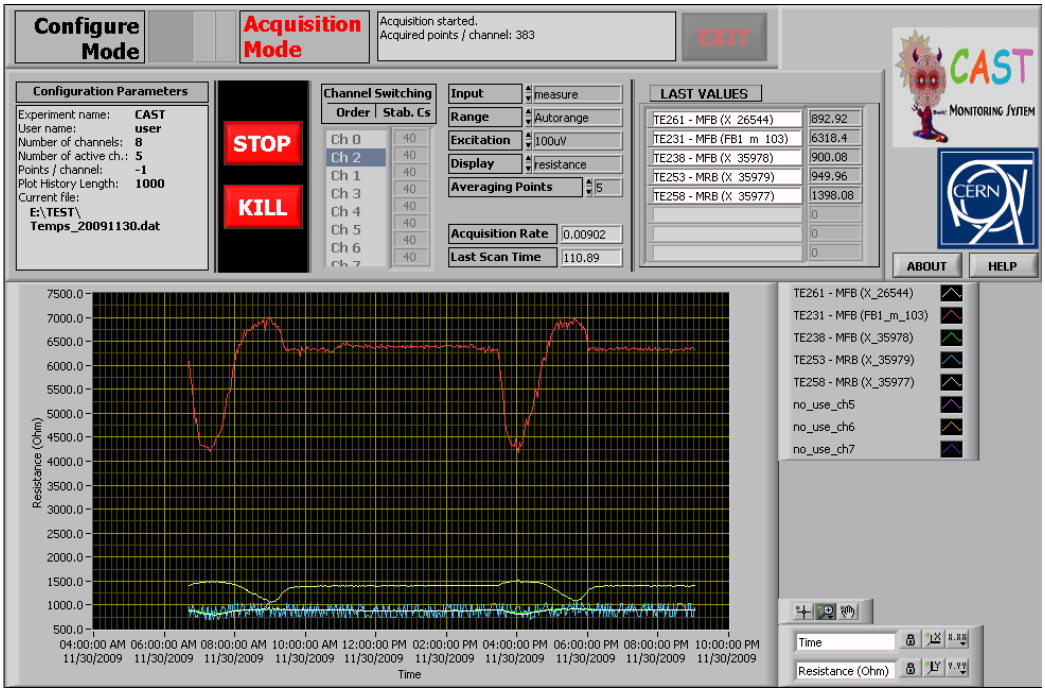

Figure 5-8: Acquisition panel of the AVS-47 driver

This allows optimizing the cycle time and the accuracy at which all the channels are read. By adjusting the order of the multiplexing sequence, for a minimum variation of resistance between sequential channels, the number of stabilization cycles can be decreased and the cycle time is optimized.

This panel also allows the specification of the basic parameters of the AVS47, such as excitation current or dynamic range. Moreover it allows an online visualization of the evolution of the temperature or resistance values for each channel, which is a great on-site tool to discern the thermodynamic behaviour of each individual region to be measured.

For the pressure measurement with the Baratron® pressure transducers we use one MKS® type 670B signal conditioner with display unit for each pressure sensor (see Figure 5-9).

Figure 5-9: High accuracy Baratron® together with the signal conditioning with display unit

This microprocessor based electronics unit has a front panel that allows full control of the instruments features. All functions can be controlled via the RS-232 or GPIB interface and a key-lock switch permits to choose the local or remote control.

Although the unit can be controlled remotely through these interfaces, unfortunately the supplier did not develop any software, therefore Labview® software had to be written from scratch to access to most desirable functions, such as range switching or interlocking.

This complex software controls the way the data is acquired by both acquisition cards. It can be sub-divided in two distinct parts depending on its goal: fast acquisition and accurate acquisition.

The fast acquisition with the NI-PCI 6221, is mainly used during the occurrence of a quench, the available 16 bit are sufficient for measuring the detailed behaviour of the pressure transient. In this case, the data is saved at a pre-established rate (~1 kHz) in a buffer for economy of disk resources.

In the occurrence of a quench, a ‘quench trigger’ signal coming from the quench detection rack activates the data recording and the data in the buffer is kept, this way one has an history of the data before the trigger event (pre-samples). The data is then continuously recorded until it matches the size of the ‘post-samples’.

Once the full set of data is recorded into a disk location and a histogram is displayed on screen. The data recording with a fast sampling rate can also be manually started, without the need for a ‘quench trigger’ signal.

The second part of the software, uses the high-precision NI-PCI 4531 card, and is mainly used for a continuous logging of the essential quantities. Here data is recorded

uninterruptedly and files are created on a daily basis. A histogram is presented always on screen (see Figure 5-10).

Figure 5-10: Display of the slow acquisition software. The left of the display contains different tabs for settings and controls. On the right side a histogram displays the evolution of the measured quantities.

This part of the software also performs some calculations that are essential during the physics runs. Here it is calculated the amount of gas that is transferred from the metering volumes into the magnet cold bores. The thermodynamic conditions in the metering volumes are recorded before and after the transfer and the cumulative amount of moles in the cold at each moment is therefore known.

5.5 Conception of the provisional ^{4}He gas system

The philosophy of the gas system for the ^{4}He runs is to have a reliable and easy to operate entity, able to provide a precise increase of the gas density inside the magnet cold bores up to ~14 mbar.

To ease the task of the various shifters or other trained person other than the system responsible, the operations were carefully thought to be conceived in a way to be easily perceived and also to minimize the risk of an erroneous operation and its effects.

A synoptic diagram of the ^{4}He gas system is presented in Figure 5-11. In order to keep it simple, only the elements that serve to control the gas flow or form a boundary with other systems are shown.

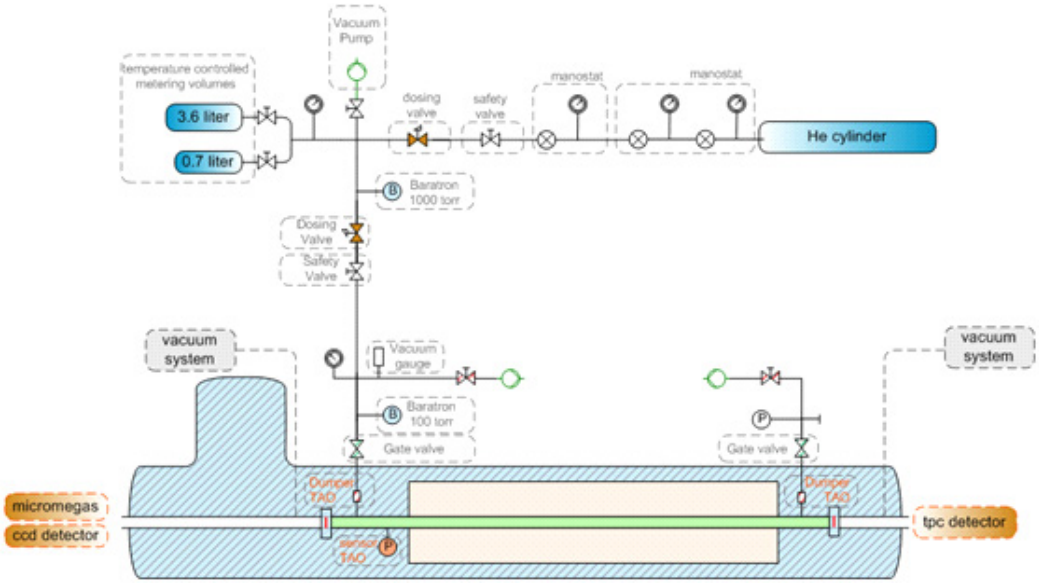

Figure 5-11: Synoptic diagram of the ^{4}He gas system

In general terms, the gas system is composed of an helium source from where the gas pressure is reduced by a series of manostats, prior to entering the metering volume. In the metering volume a precise amount of gas is prepared and sent into the magnet cold bores which will result in a corresponding increase of the gas density up to the desired setting.

During the physics data taking periods, the gas density is increased in metered steps, covering an important range in the axion mass spectrum. The gas can be removed from the cold bore through a set of pumps that can be placed at each extremity of the magnet.

The gas supply is assured by a pressurized helium cylinder (up to 200 bar), and for safety reasons is placed outside the experimental hall. The purity of the helium is better than 99.9995 % which is sufficient for metering purposes.

The pressure of the gas is initially reduced to ~ 1.5 bar in a two stage manostat before it enters the experimental hall. The pressure of the gas is further reduced to ~ 1.3 bar in a second manostat, this ensures that at any time the pressure remains below the full scale of the B-1000 pressure sensor.

The metering volumes are made of copper for improved thermal homogeneity, and require special tin brazing for a leak tight connection with the standard stainless steel piping. There are two metering volumes, and each one of them can be isolated by closure of an isolating valve.

The size of the metering volumes is optimized with the goal to maximize the full scale of the B-1000 pressure sensor during the transfer process. The smaller volume can house an amount corresponding to 1 density step and the larger volume is designed to hold 6 density steps.

The precise calculation of the amount of gas transferred at each step into the cold bore, is done by comparing the initial and final amounts inside a calibrated volume (metering volumes) immersed in a demineralized water bath, with controlled temperature in order to maintain a stable reference temperature (36ºC ±0.01ºC).

The metering volume is initially filled up to a set value of 900 mbar by opening the safety valve and a downstream dosing valve and allowing the gas to flow from the cylinder.

The flow of gas can be adjusted, by regulating the opening inside the dosing valve. To have a controlled transfer the opening of the dosing valve is decreased when the set value is approached, this allows that the set value is reach in a smooth and precise manner.

Once the set value is reached the dosing valve and safety valve are closed and the gas is left to stabilize inside the thermally controlled volume, before its pressure is recorded.

To increase the density of the gas inside the cold bore, a batch of gas is transferred from the previously filled metering volume by opening another set of safety and dosing valves that separate the two regions.

The gas flow is driven by the differential pressure between the metering volume and the cold bore. As the pressure approaches its final set value in the metering volume the opening of the dosing valve can be reduced to make the process more precise.

Finally when the set value is reached the dosing valve and safety salve connecting the cold bore to the metering volume are closed and the gas is left to stabilize inside the thermally controlled volume, prior to the recording of the pressure.

At each end of the cold bore one gate valve is installed, which allows to isolate the cold part of the system from the warm part of the system. Although during nominal operation these valves are always kept open, it was decided to place them for redundancy,

for the case when in the course of operation some upgrade needs to be done in the warm part of the system. This allows the warm part of the system to be isolated while the cold bore can be kept cold without risk of cryo-pumping gases.

In Figure 5-11 it is marked the location for connection of vacuum pumps. Although these are not necessary during nominal operations, they are indispensable during the commissioning phase of the system, when all the air needs to be pumped out, the complete circuit to be flushed with nitrogen and custom leak detection measurements to be performed. Moreover for the correct zeroing of the Baratron® pressure sensors, the pressure needs to be brought below the minimum resolution. Therefore it is foreseen extra ports and blanking valves for connection of vacuum pumps allowing the pressure to be brought down to 10^{-8} mbar level.

It was chosen to have all valves manually operated in order to give the necessary adaptability in this provisional system. This excludes the need for a programmable control but introduces the dependence in human operation.

In order to keep the of operator's task simple, the gas panel display was designed for an intuitive use, where only components that require interaction during shifts are easily reached.

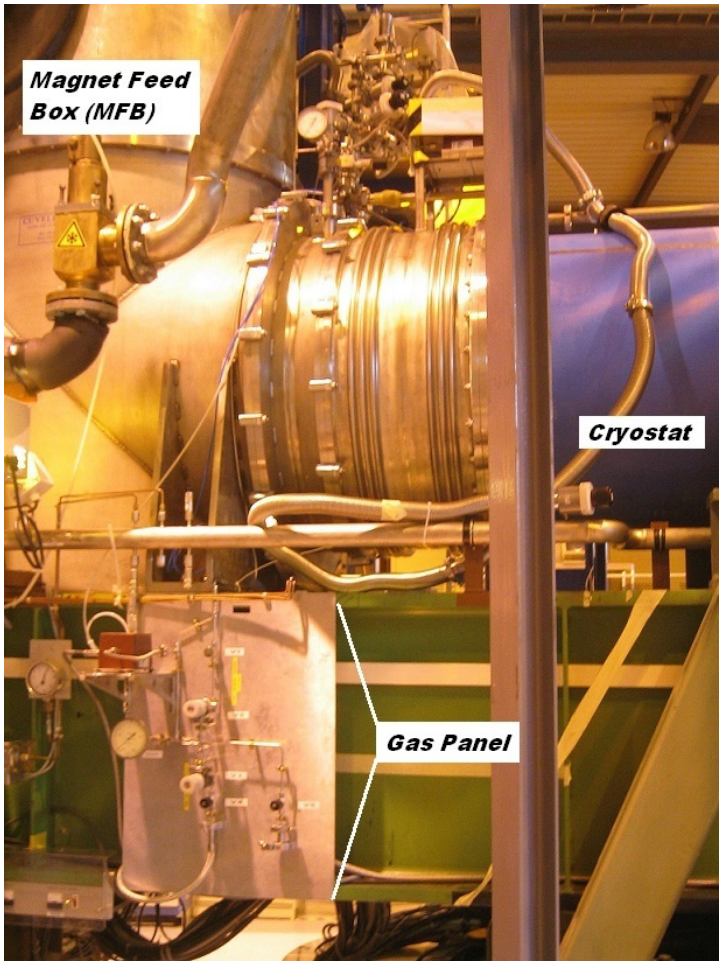

Figure 5-12: Position of the gas panel in the magnet structure

The gas panel is positioned on the MFB side of the magnet at a short distance from pivot point directly in the magnet supporting structure as shown in Figure 5-12.

The position had to be studied to find a compromise between having a reduced 'dead volumes' region and minimize interference with other systems. The panel is always reachable from the floor of the experiment even during the magnet solar tracking; this enables a safe and easy operation of the equipment and a fast action in case of need.

The thermostatic bath (not shown in the picture) is placed under the magnet between the two green girders. This position was chosen because of space limitations, which result mainly from the possibility of collision during the magnet movement with static structures around the experiment hall. Although of difficult access and installation, this location is one of the best in order to minimize the size of dead volumes.

5.6 Operating modes

The operation of transferring gas into the cold bore is done once per day, in the period of time that goes between the morning shift and evening shift. In this way the density setting is only increased once per day and both sets of detectors placed at the two extremities of the magnet are measuring in the same conditions.

The amount of gas transferred from the metering volume to the magnet cold bores can be easily calculated by filling in the following formula:

$$dn = n_{mv}^{i} - n_{mv}^{f} = \frac{P_{mv}^{i}}{R}\left(\frac{V_{mv}}{T_{mv}^{i}} + \sum \frac{V_{dv}}{T_{dv}}\right) - \frac{P_{mv}^{f}}{R}\left(\frac{V_{mv}}{T_{mv}^{f}} + \sum \frac{V_{dv}}{T_{dv}}\right),$$

where:

dn - amount of moles of gas transferred

n_{mv}^{i}, n_{mv}^{f} - initial or final amount of moles of gas in the metering volume

P_{mv}^{i}, P_{mv}^{i} - initial or final pressure in the metering volume

V_{mv}, V_{dv} - volume of the metering volume or related dead volumes

T_{mv}^{i}, T_{mv}^{f} - temperature of the thermostatic bath

T_{dv} - temperature of the dead volumes equal to room temperature

R - gas constant, 83.145 $\mathrm{mbar \cdot l \cdot K^{-1}}$

On the cold bore side, the new batch of gas will imply changes in the thermodynamic properties as:

$$dn = n_{cb}^{f} - n_{cb}^{i} = d\rho_{cb} \cdot \frac{V_{cb}}{R} + dn_{dv} = \frac{P_{cb}^{f} - P_{cb}^{i}}{R}\left(\frac{V_{cb}}{T_{cb}} + \sum \frac{V_{dv}}{T_{dv}}\right),$$

where:

n_{cb}^{i}, n_{cb}^{f} - initial or final amount of moles of gas in the cold bore

$d\rho_{cb}$ - density variation in the cold bore

P_{cb}^{i}, P_{cb}^{f} - initial or final pressure in the cold bore

V_{cb}, V_{dv} - volume of the cold bore or related dead volumes

T_{cb}^{i}, T_{cb}^{f} - initial or final cold bore temperature

T_{dv} - temperature of the dead volumes equal

The process of calculating the gas density setting after the operation of transferring a precise amount for gas from the metering volume to the magnet cold bores, is represented in the following diagram.

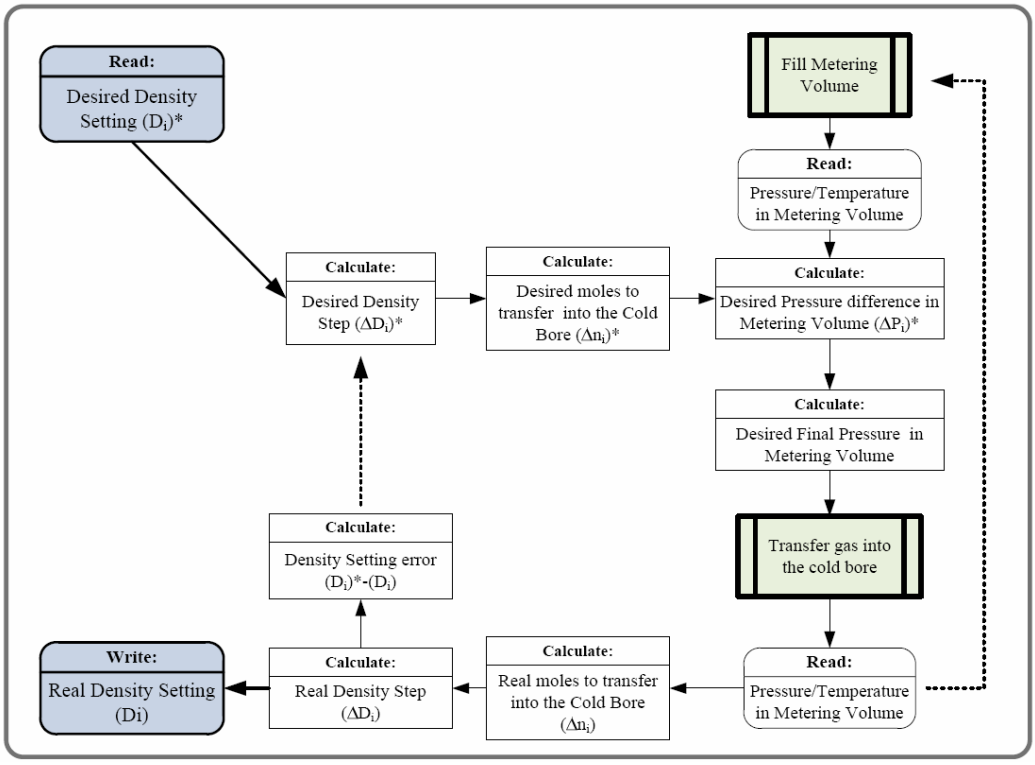

Figure 5-13: Diagram representing the calculation steps and actions for transferring a metering amount of gas from the metering volume into the cold bores.

The calculation takes into account the desired gas density inside the cold bore for a given physics run – 'desired density setting'. A list with all the desired density settings has been prepared by the CAST-Analysis group.

This group defines the data taking strategy for optimizing the available data taking time and having a smooth coverage of all axion masses with the same sensitivity, by means of overlapping at FWHM the expected axion mass distribution for two adjacent density settings.

The amount of gas to be transferred is calculated by comparing the desired density setting with the actual density inside the cold bores. By determining this amount it is possible to compute the desired pressure difference in the metering volume that will correspond to that amount (assuming a constant temperature).

Once the metering volume is filled with gas up to the set pressure the thermodynamic properties are accurately measured. From here the desired final pressure after transfer is determined, and becomes the setpoint value in pressure to be reached at the end of the transfer procedure.

The transfer procedure of gas is initiated by order of the operators (shift personnel). Here a set of valves is opened putting in communication the metering volume and the cold bore. The gas flow rate is controlled by the adjustment of the dosing valve throughput and the procedure is stopped when the desired final pressure in the metering volume is reached.

At the end of the transfer procedure, and once steady conditions are attained, the thermodynamic properties of the gas in the metering volume are measured, at this moment the real amount of gas transferred into the cold bore is also computed.

5.7 Physics Runs with ^{4}He

The physics runs with ^{4}He started on the 24th of November 2005 and lasted until the 8th of December 2006. During this time there was a forced shutdown due to maintenance works in the Cryo-plant, which lasted from February until April 2006.

During this period, the X-ray detectors were operated in the same configurations as for the First Phase, except for a small number of improvements:

The TPC, covering both cold bore apertures and looking for axions during the Sunset tracking, improved its electrical noise level, by using improved low voltage power supplies.

In the other magnet extremity looking for axions during the Sunrise tracking a new MM detector was installed, having an improved performance due to the introduction of a gold-coated amplification mesh that reduced the copper fluorescence which used to dominate the detector background. As for the CCD, improvements were done to the vacuum system of the telescope and control system which resulted in a more safe and flexible mode of operation.

During the data-taking period the magnet was aligned with the Sun during two periods of the day (each during about 1.5 h), while the rest of the time was used for acquiring background data and to make detector calibrations.

During the full data taking period, the gas density in the cold bores was changed in 160 consecutive uniform steps, each corresponding to 0.083-0.087 mbar at 1.8 K. The maximum pressure attained in the end of the runs was 13.424 mbar, which corresponds to an effective photon mass of 0.39 eV/c^2.

The density setting was changed once per day so that both sunrise and sunset detectors could cover all settings. Although all the detectors performed well, due to some problems related to individual detectors that were promptly identified and corrected, a small number of density settings were missing for individual detectors. The applied protocol was for most of the cases, to repeat the tracking for those specific settings. From the use of this method it results that all settings have been scanned without exception without major loss in data taking time.

A summary of the data acquired at each individual detector is given in Table 5-4. The final CAST result is a combination of all three detectors.

	Density Settings	Tracking [h]	Background [h]	Rate [keV^{-1}s^{-1}cm^{-2}]	Energy Range [keV]
CCD	147	264.8	2758.1	$(8.66\pm0.06)\times10^{-5}$	1-7
TPC	154	304.1	4346.6	$(7.68\pm0.01)\times10^{-5}$	2-15
MM	159	336.6	3115.0	$(4.75\pm0.02)\times10^{-5}$	2-9

Table 5-4: Summary of the data taken in the Second Phase with ^{4}He in the cold bores.

The results are compatible with absence of signal, and therefore it can be expressed as an upper limit on the axion photon coupling with a 95% confidence level. The full exclusion plot shown is shown in Figure 5-14.

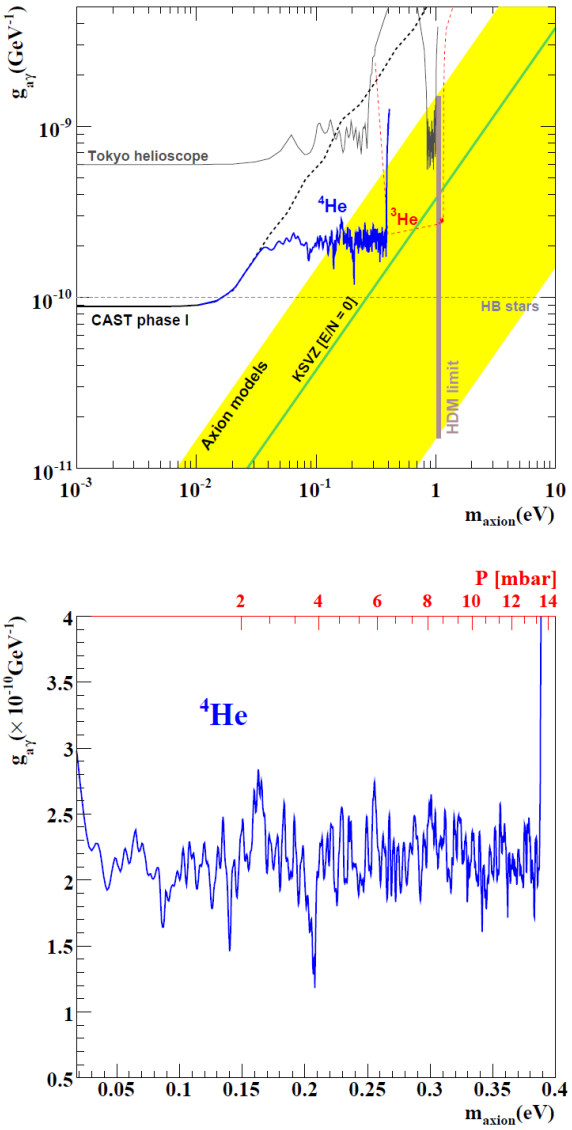

Figure 5-14 : Top: Exclusion plot in the axion-photon coupling versus the axion mass plane. The limit achieved by the CAST experiment (combined result of the CAST-First Phase and ^{4}He part of CAST Second Phase). The vertical line (HDM) is the hot dark matter limit for hadronic axions $m_a < 1.0$ eV/c^2 inferred from observations of the cosmological large-scale structure. The yellow band represents typical theoretical models (the green solid line corresponds to the case when E/N = 0). The red dashed line shows the prospects for the runs with ^{3}He. Results from the from the Tokyo helioscope and HB stars are also shown. Bottom: Expanded view of the limit achieved in the ^{4}He data taking in CAST Second Phase for m_a between 0.02 eV/c^2 and 0.39 eV/c^2 corresponding to a pressure scan from 0 to 13.4 mbar at 1.8 K [29].

As can be seen in Figure 5-14, CAST was able to extend its exclusion line from axion masses of 0.02 eV/c^2 (First Phase of the experiment with the magnet cold bores under vacuum), to an impressive increase up to masses of 0.39 eV/c^2, by filling the magnet cold bores with buffer gas (^{4}He). This is the first time that a result derived from direct observation was able to enter the QCD axion model band in the eV/c^2 range, excluding an important part of the parameter space.

6 The ^{3}He Gas System

The provisional gas system operating with ^{4}He has produced the best limit so far on the axion mass range from 0.02 eV/c^2 up to 0.39 eV/c^2.

It represents an important tool for study but has important limitations: The most important one is the saturation pressure of the ^{4}He gas (16.4 mbar at 1.8 K), representing a limit on the axion mass search at 0.41 eV/c^2.

To enhance the axion search above the previous limit, considerable changes have to be made. By changing the gas type to ^{3}He which has a higher saturation pressure at 135 mbar at the magnet operating temperature, it is possible to extend the axion mass search reach up to ~1.2 eV/c^2, thus closing the gap up to the cosmological limit.

Unfortunately there is a price to pay for this major improvement. ^{3}He is a very rare and expensive gas, and therefore 'zero losses' is one of the aims, representing an additional cost in components, but also additional methods to monitor the leak-tightness of the system have to be develop.

Moreover due to the high pressures that can be generated during a magnet quench, it is wise to have a methodology to reduce the risk of failure of the cold thin X-ray windows by limiting the maximum attained pressure to low and safe values.

Additionally, it is required that new and more flexible modes of operation are implemented, allowing the gas density to be increased or decreased, in a fast stepped manner or optionally in a slow ramped way, but always in a metered fashion.

Due to the increased level of complexity of this new system and numerous instruments to be read and operated, the supervision and control and logging is better done by a Programmable Logic Controller (PLC).

6.1 Conceptual design of the ^{3}He Gas system.

The philosophy behind the design of the ^{3}He gas system is based on a set of requirements endorsed by decisions of the CAST Steering Committee, which are based upon experience gained during operation with ^{4}He; these can be listed as:

- Safety against loss of ^{3}He gas
- Metering of the amount of ^{3}He in the magnet bores with the reproducibility compatible with the resolution and reproducibility of the temperature and pressure measurement of the gas metering volumes.
- Absence of thermo-acoustic oscillations
- Protection of the thin X-ray windows during a quench.
- Remote data logging of the state of the gas system, without feedback
- No safety release of ^{3}He elsewhere except to the safe storage vessel.
- Flexible operations modes, which include the possibility for increasing or decreasing gas density either by a stepping or ramping manner.

Based on these requirements a complete study was done. This entailed an investigation into the most suitable system configuration and an evaluation of the the necessary equipment to build it. The Technical Design Report (TDR) [30] of the CAST ^{3}He gas system was submitted to a review committee of internal and external referees for recommendations.

The gas system can be described as a hermetic closed gas circuit assuring full recovery of helium. It can be divided in functional sections with specific purposes:

- Storage: Region where all the necessary ^{3}He gas for the physics runs is contained.
- Metering: Region where the batches of gas are accurately metered before being transferred in or out from the cold bore.
- Cold bore: Region confined by the cold X-ray windows where the gas density is maintained stable during the solar tracking. Here axions are expected to convert into photons. The absence of thermo acoustic oscillations is monitored.
- Expansion: Region used for fast extraction of the gas from the cold bore in case of quench.
- Recovery and circulation: Region where the gas is circulated back into the storage, where the pressure is elevated for driving the flow and where any gas contaminants can be trapped.

Figure shows a simplified diagram on how each individual block interacts with the others, making it a closed hermetic and recirculating system.

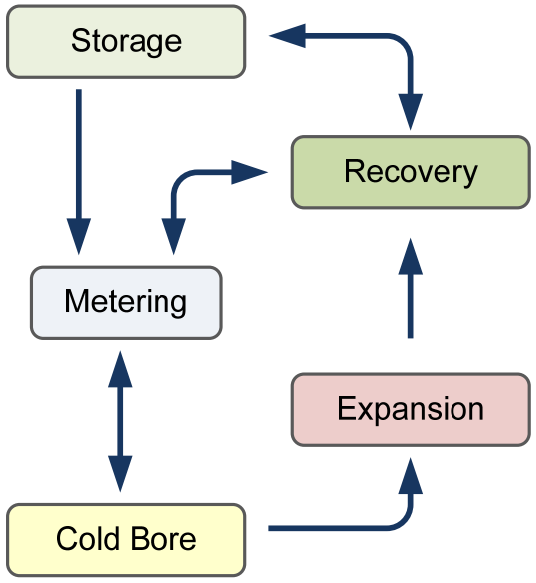

Figure 6-1: Simplified flow diagram of the main blocks that compose the ^{3}He gas system

Additionally there are a small number other detachable units that are required for completeness:

- ^{3}He transfer unit: Used for transferring the gas from the original transport cylinder into the storage.
- Trap purging unit: Used for regeneration of the traps (charcoal and room temperature)
- Pump oil purging unit: Used for purging the pump oil form air contaminants.
- Initial evacuation unit: Vacuum pumps responsible for the initial evacuation of air from the circuit
- Leak detection unit: Standard Helium leak detection unit

The following synoptic diagram represents the ^{3}He gas system process layout. Due to the large amount of equipment a naming code has been implemented for a faster identification:

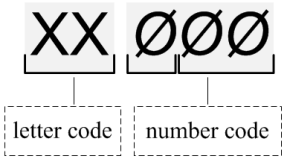

The letter code and the symbol identify the type of object:

Letter Code	Represents
P	*Pump*
V	*Volume*
PI	*Pressure Indicator*
PT	*Pressure Transducer*
PV	*Powered Valve (Electro-pneumatic actuated)*
CV	*Control Valve (Mass flow controller)*
HV	*Hand Valve (Manually operated)*
NV	*Check Valve (Opens by pressure differential)*

The number code addresses to the equipment list. The first digit indicates the location on the system where the component is located:

Number Code	Represents
1##	*Metering Panel – Located on the magnet support structure for easy access.*
2##	*Cold Bore and Expansion volume – Located inside the magnet cryostat, or on top of the magnet cryostat.*
3##	*Storage volume and Recovery – Located on the floor of the experimental hall.*

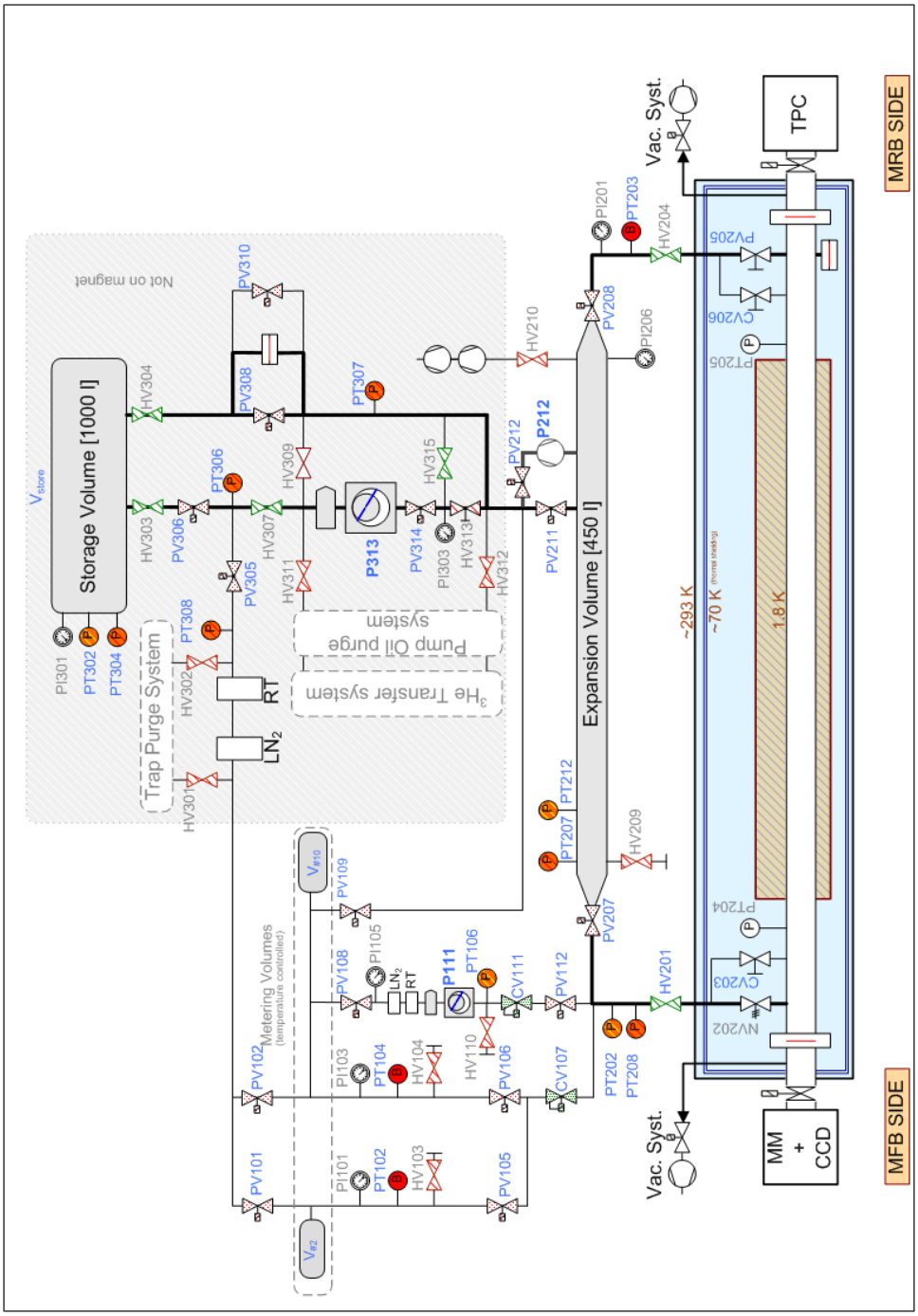

Figure 6-2: Schematic diagram of the ^{3}He gas system, with the cold bore tubes shown as one volume inside the cold dipole magnet (blue). The thin X-ray windows are represented by red lines. The thick lines represent the large pipework used for normal and emergency recovery of ^{3}He. The green valves are blocked in open position, and the red ones in closed position, during all normal operations.

The system is initially completely evacuated of air to a pressure better than 10^{-6} mbar using powerful pumping groups consisting of primary and turbo vacuum pumps. These groups allow a possible ultimate pressure of the order of 10^{-9} mbar or better.

To accomplish this manipulation, dedicated pumping ports are available in different sections of the system, which can be closed or opened via manual valves and blanking flanges. The same ports can be used for standard helium leak testing with a mobile detection unit, having a resolution in the 10^{-9} mbar·l·s^{-1} range.

All the necessary ^{3}He gas (~1000 atm·l) is property of LNLL and is supplied in a pressurized transport cylinder. A dedicated unit is needed for the manipulation of transferring the gas from the transport cylinder into the system storage.

The size of the storage volume is such that the gas is contained below the atmospheric pressure; this allows that in an event of a developing leak, the phenomenon can be identified by a raising pressure towards atmospheric values and the helium loss is minimized. The use of standard pressure transducers is an advantage.

The gas can flow through the circuitry naturally due to the pressure differential between adjacent regions or, in the case that the differential is too low, the flow can be forced using a ^{3}He hermetic rotary pump.

Prior to its metering, the gas passes a set of purification traps, filled with activated charcoal. One of the traps is at room temperature and the second one is cooled in a liquid nitrogen bath.

The precision of metering is obtained by the accurate temperature control of the metering volumes, and by the use of a metrology-grade pressure measurement instrument to determine the amount of gas introduced into the cold bores.

The temperature of the gas along the cold bore tubes should be maintained stable during run conditions due to the good thermal anchoring provided by the magnet superfluid helium. The gas is confined in the cold bore region of the magnet with thin X-ray windows.

Different scenarios have to be considered for the heating of the windows, and the heaters on the window flanges have to be foreseen also to make periodical bake-out of gases adsorbed on the window foils.

To avoid thermo-acoustic oscillations, the warm pipes linking to room temperature are isolated during normal operation by means of the cryogenic valves. These valves consist of a check valve NV202 and a shut-off valve PV205, which are closed during normal operation, and open only during a quench when evacuating the cold bore.

In case of quench, the pressure of the gas increases rapidly and the cryogenic check valve NV202 opens when the differential pressure reaches 30 mbar, whereas on the MRB side a cryogenic valve will open by *quench triggering*.

During the quench, the gas is safely evacuated from the cold bore to an expansion volume via two electro-pneumatic valves PV207and PV208. The X-ray windows should withstand at least 2 bar pressure in the cold bores.

These two electro-pneumatic valves will open by *quench-trigger* signal activation, and the gas is led to an expansion volume kept normally under vacuum. The pressure reached in case of quench should not exceed 1.2 bar even in the case that the main ^{3}He pump fails to start. Normally the pump will automatically start by the quench trigger, and it displaces the gas from the expansion volume to the storage volume.

The electro-pneumatic valves PV207 and PV208 will open in the case of failure of electrical power, and they are also partially opened in absence of compressed air.

The permanent availability of compressed air is secured by a large buffer volume which is part of the auxiliaries upgrade in the experimental zone. The compressed air pipework is secured against accidental ruptures, and an alarm is provided in the event of any anomaly in the compressed air system.

In case of accidental conditions where the ^{3}He pump will not automatically start (loss of power, unknown factors) and the pressure during a quench exceeds 1.5 bar, a rupture disk is foreseen to open the cold bore to the storage volume and the pressure to be equalized below 1 bar.

Moreover, the simmering seals of the ^{3}He pump can only withstand up to around 2 bar and will release the gas if this pressure is reached.

The system will be supported on the magnet structure on the airport side of the magnet. By doing this, complications due to the flexibility of the lines are minimized, but careful study should be done in order to avoid interference with non moving structures.

6.2 Functions of the main components

Storage

All the necessary ^{3}He for the CAST physics runs should be first transferred to the storage volume, dimensioned to keep the gas pressure below atmospheric. The gas in the storage volume will be contaminated by pump oil vapour, but oil mist will be filtered right behind the main ^{3}He pump.

Purification traps

Before entering the metering volumes the gas passes through 2 charcoal traps, the first at room temperature (RT) and the second at liquid nitrogen temperature (LN_2). The first one traps oil and water vapours, and it is regenerated by exchanging the charcoal cartridge. The second one can be warmed up in order to evacuate and purge the impurities using a neutral gas. The purge operations will be scheduled in shutdown periods, and ^{3}He will be evacuated from the traps before the purge.

Metering of gas

To scan over a wide range of axion masses CAST will need to control precisely the ^{3}He gas density in the cold bore. This is achieved by filling the cold bores with precisely metered amounts of gas in incremental steps, or by ramping between metered increments using a mass flow controller and a small auxiliary pump.

Each day two tracking periods take place, one in the morning and another in the evening, each of them with duration of ~100 minutes. Stepping of the gas density is done in equivalent pressure steps of between 0.0833 mbar and 0.1000 mbar (calculated with gas at a nominal temperature of 1.8 K).

The step spacing between density settings corresponds to the density change required to shift the peak of the mass setting by one FWHM of the mass acceptance profile, as shown in Figure 3-2. In order to cover the whole available mass range efficiently, data taking runs will have to cover at least two density settings per solar tracking.

Different options are foreseen for the metering and ramping of the gas into/from the cold bore:

- Increased stepping mode (two discrete density settings per tracking)
- Density ramping-up mode (ramp over a range between 0.25 to a maximum of 10 steps)
- Density ramping-down mode (ramp over a range between 0.25 to a maximum of 10 steps)
- Density scanning mode (ramping around a pressure setting)

The gas introduced in the magnet bores must be pumped out after each quench and other major interruption of the experiment. The question of accuracy in reproducing a previous setting of the amount of the buffer gas was already addressed in section 3.4 and the measurement of the amount of gas transferred to the cold bore is calculated by

accurately measuring the pressure decrease on the metering volumes that are maintained at constant temperature.

As an alternative, for a reproducible and faster way of reaching the high-end gas fillings would be to send all gas into the magnet, and then step or ramp down in pressure to the desired value. The pressure and temperature measured in the magnet bore should then be used for estimating a safe overlap between the fillings reached from below and from above.

The ramping is done using mass flow controllers that assure a constant mass flow rate.

An additional small hermetic ^{3}He pump (P111) allows the removal of gas from the cold bore back to the metering volumes that are used for calibrating integrated readings of the mass flow controller. The reproducibility of the amount of gas after several successive ramps is similar to that of discrete stepping, because the amount of gas is always metered using the thermostated volumes and precise pressure gauges.

Axion conversion region (cold bore)

The axion conversion region (magnet cold bores) occurs inside two parallel straight pipes of ~10 meter (magnetic length 9.26 m) and 43 mm diameter, the pipes being immersed in a transverse magnetic field of 9 T (for a magnet current of 13 kA) produced by the superconducting magnet kept at ~1.8 K by a superfluid helium cooling circuit. The magnet, mounted on a rotating platform, is kept aligned with the Sun during the experimental runs that take place for 1.5 hours during both the sunrise and the sunset.

Outside the magnetic length the pipe changes diameter (63 mm) until the X-ray cold windows surface. The two cold bore pipes are allowed to communicate via two pipes of 35 mm diameter (one at each end of the magnet).

At each end of the cold bores two 15 μm polypropylene windows (thin X-ray windows) confine the gas in the cold region. The cold X-ray windows separate the ^{3}He gas region from the vacuum side connecting to the detectors.

The temperature of the windows can be modified, over a certain range, using heaters on the window flanges nearby. If no heating power is applied, the window foil becomes the coldest spot of the vacuum system, causing desorbed gases from surfaces to be cryo-pumped onto the window foil.

The accumulation of frozen gases in a layer on the foil reduces the X-ray transmission. For layer thicknesses near to the wavelength of light, interference effects are produced and with appropriate backlighting, dark spots on the surface of the foil can be observed. The constant heating of windows is a preventive way to reduce the formation of dark spots, but also permits scheduled warming (bake-outs) to assure that any frozen gases are released from the window foil.

Valves for preventing thermo-acoustic oscillations

To prevent thermo-acoustic oscillations from developing, the 35 mm pipes linking the cold bore tubes to the room-temperature pipework must be closed at the cold end. These oscillations were precisely characterized during the first tests with ^{4}He, and they were eliminated by laminar flow elements with large flow resistance, installed at the exits of the cold bore tubes. These reduce the gas flow severely in the viscous regime, while impeding relatively less the evacuation speed when the pressure and temperature reach molecular flow conditions.

For ^{3}He these laminar-flow elements must be replaced by cryogenic valves, which close well enough to avoid thermo-acoustic oscillations, and which open quickly enough to permit the rapid evacuation of the gas during a quench. These valves are NV202 that opens at 30 mbar forward pressure, and the electro-pneumatic cryogenic valve PV205 that is normally open.

These valves are bypassed by small needle valves CV203 and CV206 that can be adjusted so that no oscillation will start. These also allow a rapid pressure equilibrium between the cold bore volume and the pipework leading to room temperature. The needle valve on the MFB side also enables accurate monitoring of the cold bore pressure using the B100 MKS Baratron pressure gauge.

Although the cryogenic electro-pneumatic valve and the check valve can be purchased from specialized cryogenic manufacturers, the needle valves have to be custom made to fit into our system.

Expansion and recovery of ^{3}He triggered by the magnet Quench

During a quench the temperature of the magnet rises rapidly. If the cold volume remains closed, the gas pressure will rise proportionally as shown in section 4.2. When operating close to the saturation pressure of ^{3}He at 1.8 K the peak pressure would reach about 2.8 bar. This puts in danger the integrity of the X-ray windows, and forces to

evacuate the gas sufficiently fast to keep the pressure below the safe operating pressure of the windows.

The cryogenic valves NV202 and PV205 and the expansion volume provide a first safety to the system. The expansion volume is calculated in such way that the maximum pressure reached at the cold windows would be ≤ 1200 mbar by evacuating the gas from the cold bore into a initially under vacuum expansion volume.

The expansion volume initially under vacuum thus acts as a buffer volume for the gas coming out of the cold bore during a quench.

All entry connections are equipped with metallic seals, because the gas coming out of the cold bore during a quench is cold. The gas will reach practically stagnation conditions after conical entry transitions, which increase the gas temperature and pressure. The gas will subsequently warm up in the large pipe before entering the main pump at a temperature close to ambient.

6.3 Technical Design of the main equipment

Storage volume

We require that the storage volume be dimensioned to contain the entire inventory of the ^{3}He gas at a pressure below atmospheric. Its volume can then be estimated according to the formula:

$$\frac{P_{store} \cdot V_{store}}{T_{store}} = F_{safety}\left[\frac{P_{cb}^{n} \cdot V_{cb}}{T_{cb}} + \sum_{i}^{allregions} \frac{P_i \cdot V_i}{T_i}\right]. \qquad (1.1)$$

The left hand term is the amount of gas in the storage volume, the right hand multiplier is the safety factor $F_{safety} = 1.2$, and the terms in the brackets are the amount of gas in the cold bore for the highest pressure setting and the amount of gas in the dead volumes, namely those between the main pump and the storage tank, and the metering volumes.

At the highest steps of ^{3}He density (already well below the equivalent pressure of saturation, i.e. 135.58 mbar), the pressure in the storage volume will be too low to fill the metering volumes up to a pressure required to make a step in the amount of gas in the cold bores. Because of this, the ^{3}He pump will be used for pressurizing the gas prior to sending it through PV305 to the metering volumes.

The table summarises the properties of the gas in different regions:

	Pressure [mbar]	Volume [litre]	Temperature [K]	Fsafety x n [mol]
Cold bore	*135*	*30*	*1.8*	*32.6*
Other volumes (RT)	*800*	*10*	*310*	*0.4*
Other Volumes (OT)	*800*	*10*	*77*	*1.5*
Total				*34.5*

The total amount of moles needed is 34.5 mol. The storage volume will be maintained below atmospheric pressure (assume 900 mbar) and at ambient temperature (assume 293 K).

The following table summarises the properties of the volume:

	Pressure [mbar]	Volume [litre]	Temperature [K]	Fsafety x n [mol]
Storage volume	*900*	*932*	*293*	*34.5*

The volume of the storage tank is 932 litres. To give an idea of the dimensions it is a cylinder shape of about 800 mm diameter and 2000 mm length with a weight of about 300 kg.

It is made to withstand vacuum (avoiding elastic instability), and to withstand 500 mbar overpressure with respect to atmospheric pressure.

The following picture displays the results of a finite element study to account for elastic instabilities of a vacuum container with the same dimensions of the storage volume and a wall thickness of 3 mm. The maximum registered Von Mises stress (95 MPa) is about 56 % of the elastic limit (170 MPa), representing a fair safety margin and a good design.

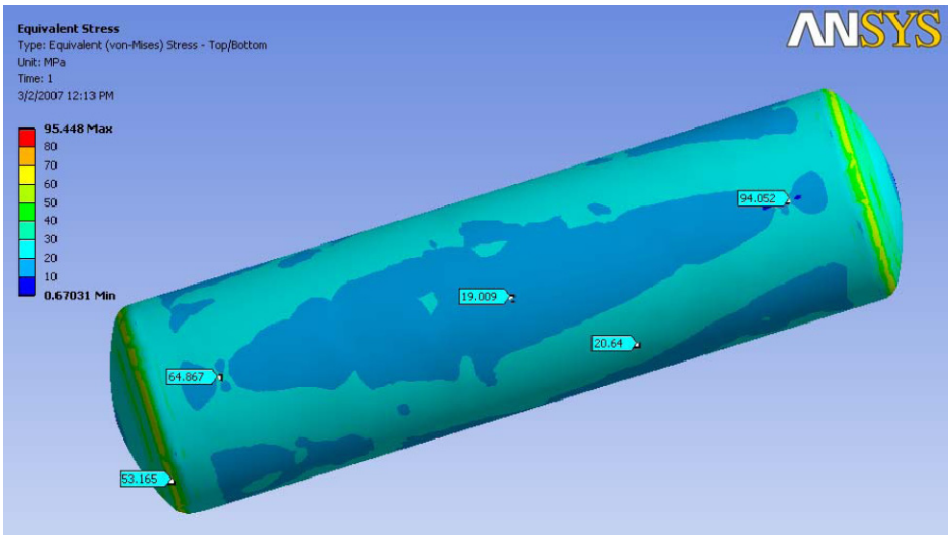

Figure 6-3: Finite element study of a vacuum container with dimensions of the storage volume. Von Mises stresses displayed with colour map. All results below elastic limit. Courtesy Ph.Silva.

Metering Volumes

The two metering volumes are placed inside a thermostatic bath. The smaller volume is used for transferring two density settings into the cold bore during a solar tracking; the second and larger volume is to be used specifically for pressure ramping over a range of up to 10 density steps.

The thermostatic bath should keep the temperature of the volumes constant at (36 ± 0.01 ºC), for accuracy the size of the piping and other dead volumes outside the metering volumes should be minimized to avoid systematic errors due to ambient temperature variations.

	dPressure [mbar]	Volume [litre]	Temperature [K]	dn [mol]
Cold bore	*2 x 0.1*	*30*	*1.8*	*0.04*
Cold bore	*10 x 0.1*	*30*	*1.8*	*0.20*

The metering volumes should be sized as:

	dPressure [mbar]	Volume [litre]	Temperature [K]	dn [mol]

Metering Volume (MV#2)	*600*	*1.63*	*309*	*0.04*
Metering Volume (MV#10)	*600*	*8.58*	*309*	*0.02*

The volume of MV#2 would be of 1.63 litres. To give an idea of the dimensions it is a cylindrical shape of 80 mm diameter and 330 mm length.

The volume of MV#10 would be of 8.58 litres. To give an idea of the dimensions it is cylindrical shape of 200 mm diameter and 280 mm length. Both are designed to withstand vacuum and an overpressure up to 1500 mbar.

It has previously been mentioned that in order to keep with the desired accuracy the 'dead volumes' should be minimized. Due to the large modes of operations and flexible manipulations, the layout of the metering panel had to be studied in great detail. The following picture shows a 3D model of the proposed layout:

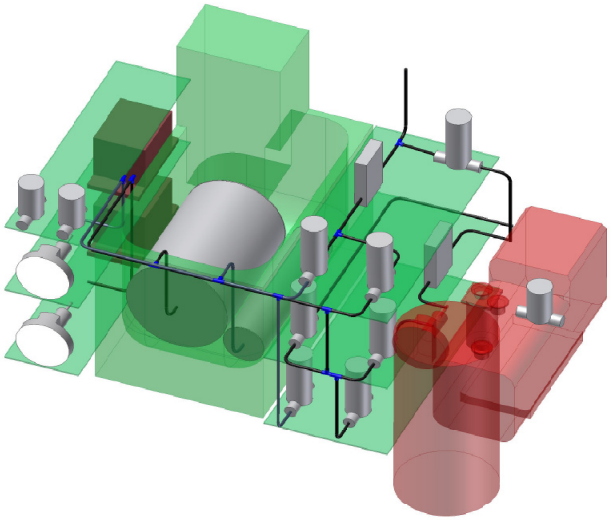

Figure 6-4: Three dimensional study of the metering panel layout in order to minimize the size of the 'dead volumes' making it possible to be assembled and welded together. In semi-transparent green the support structure and the thermostatic bath. In red, the small ^{3}He pump required for the stepping/ramping down the gas density in the cold bore and the LN_2 trap for purifying the gas in case of contamination with pump oil. In grey and black the volumes, valves and the pipework on brown the metrology grade Baratron® pressure sensors.

The metering panel has been assembled by qualified welders of the CERN main workshop, together with experts from the Cryolab that performed the leak testing. A picture of the final panel is presented below:

Figure 6-5: Picture of the metering panel after being completed.

Expansion volume

The expansion volume is designed to collect the gas rushing out of the cold bore during a quench, so as to keep the pressure inside the cold bore below the maximum value of 1200 mbar (without the ^{3}He hermetic pump running).

When a quench trigger signal is received, the interlock system will open the electro-pneumatic valves placed on both sides of the magnet, thus connecting the cold bore to the expansion volume. The hermetic ^{3}He pump will start running and another electro-pneumatic valve will allow the gas to be pumped from the expansion volume back to the storage tank. It is expected that the pressure in the cold bore will be lower due to the active pumping, but for the design we shall adopt the worst case scenario, where the pump or the electro-pneumatic valve connecting to the pump do not work properly. This may happen for example when the quench is caused by a power failure.

The expansion volume is placed at room temperature, because there is no place available inside the cryostat, and the cooling power of the magnet is already near its limit.

Our quench tests with ^{4}He have shown that during a quench the pressure increases by a factor of 14 in the first 3 seconds and by a factor of 21 in the first 200 seconds.

The worst case scenario would be in the last pressure setting 135 mbar (~33.7 mol of gas in the cold bore). The following formula summarizes the mass balance:

$$F_{safety} \cdot \left.\frac{PV}{RT}\right|_{CB,before\_quench} + \left.\frac{PV}{RT}\right|_{EV,before\_quench} = P_{MAX} \cdot \left(\left.\frac{V}{RT}\right|_{CB,after\_quench} + \left.\frac{V}{RT}\right|_{EV,after\_quench} \right)$$

The expansion volume is kept in passive vacuum and thus the second term of the equation falls to zero, P_{MAX} = 1200 mbar, and the temperature of the cold bore after the quench will increase from 1.8 K to 37.8 K (x21). A Safety factor, $F_{safety} = 1.2$ was used here.

This results in an expansion volume of 450 litres distributed along 10 meters placed alongside the cryostat and connected at both ends by electro-pneumatic valves to the gas lines connecting to the cold bore.

Its shape is mainly restricted by the chariot that holds the screws for the vertical pivoting of the magnet, but mainly has a cylindrical shape of 250 mm diameter designed to withstand vacuum and pressure up to 1 bar. Its weight is about 300 kg.

Figure 6-6: Picture of the 'Expansion Volume' being lowered by the crane into its final position on top of the magnet cryostat. At each extremity the expansion volume has conical tapers and for a reduced diameter, passing on the MRB side under the yellow chariot for the vertical movement and of the MFB side under the magnet cooling transfer lines.

Pumps of the ^{3}He gas system

There are 3 different pumps on the ^{3}He gas system, which are used to perform very distinct tasks.

The main hermetic ^{3}He pump (P313) has the task of emptying the ^{3}He from the cold bore tubes into the storage reservoir and, in the case of a quench, to recover the gas from the expansion volume back to the storage volume. This pump will also be needed for compressing the ^{3}He into the metering volumes, when the storage pressure is lower than the pressure required to fill these volumes.

We choose a two stage rotary vane vacuum pump model TRIVAC B65D from Oerlikon® with 65 m^3/h pumping speed. It ensures an ultimate continuous vacuum of 10^{-4} mbar and it has improved sealing so that it can attain a leak-tightness for helium below 10^{-7} $mbar \cdot l \cdot s^{-1}$. This pump has low oil back-streaming and in the exhaust port it is installed an oil mist filter, which has been adapted in order to have possibility for lubricant return.

The smaller hermetic ^{3}He pump (P111) is used in case of need to reduce the gas density in the cold bore, either being when a specific setting needs to be revisited, or in the alternative operation mode when it is desired to continuously ramp down the gas density. In either case the ^{3}He gas is pumped from the cold bore back into the larger metering volume where its thermodynamic properties are measured.

We decided for a two stage rotary vane vacuum pump model 2005H1 from Alcatel® with $5m^3/h$ pumping speed. It comes with a buit-in anti suck-back valve in the inlet port for vacuum integrity. It ensures an ultimate continuous vacuum of 10^{-4} mbar and it has improved sealing so that it can attain a leak-tightness for helium below $2 \cdot 10^{-7}$ $mbar \cdot l \cdot s^{-1}$. This pump has low oil back-streaming and in the exhaust port it is installed an oil mist filter.

Directly connected to the expansion volume we have foreseen a turbo drag vacuum pump (P212) for a final evacuation of both the expansion volume and the cold bore after a quench. This pump is backed by the main ^{3}He pump. It can achieve an ultimate vacuum level better than $5 \cdot 10^{-10}$ mbar and has a pumping speed of 520 l/s for helium. With its large inlet port CF160 it assures a fast and complete evacuation.

Purification Traps and Trap purge system

In order to remove any residual gases coming from an unbaked system one uses a set of regenerated charcoal traps. The first one, traps mainly water vapour and pump oil and is positioned at room temperature, the second one is immersed in a LN_2 bath is used

for trapping air contaminants For an efficient cleaning the gas flow is set to be below 10 mmol.s^{-1}.

The design of the trap consists of two cylindrical chambers; the smaller where the charcoal is confined, is contained by the outer chamber. Between these two walls a spiralling channel obliges the gas to cool down before entering the inner chamber. The regenerated charcoal will then trap any contaminants as the gas slowly flows through.

Figure 6-7: Exploded view of the construction of LN_2 charcoal trap

During maintenance periods a mobile gas handling system is connected to the valves HV301 and HV302 that give external access to the otherwise-closed gas circuit. The Trap Purge System has a vacuum pump, a leak detector, a cylinder of dry N_2 and pressure reducer, an oven that clamps onto the LN_2-cooled trap, and metallic valves that allow the practical execution of all operations.

The charcoal of the room temperature trap can be replaced by a new charge activated at a high temperature whilst the charcoal in the LN_2-cooled trap will be regenerated by warming it up to 150 °C and then purging it with dry N_2 before evacuating and cooling down. The purge operation will take about 8 hours.

^{3}He transfer system

This mobile gas handling system consists of a small vacuum pump, precise manometers, progressively opening metallic valves, a leak detector. The main pump is used for the complete evacuation of the gas from its transport cylinder.

Oil purge system

This mobile gas handling system injects dry N_2 to the inlet of a pump for purging the pump oil. The purge system is connected to valves HV311 and HV312, and it consists of a small rotary vane pump for initial and final evacuation, a cylinder of dry N_2 with a pressure reducer, a helium leak detector, and a floating bead flow meter. A cooled trap enables to monitor the cleanness of the nitrogen exhausted by P313 during the purge. During the purge the pump will be operated as warm as possible, in order to speed up the evacuation of the oil contaminants. The residues of nitrogen remaining in the oil will be removed by the liquid nitrogen cooled charcoal trap of the Purifier Trap System prior to the precise metering and admission into the cold bore tubes.

Pressure sensors

We use the same type of sensors as for the ^{4}He provisional gas system. The MKS Baratron 690 The instruments allow the pressure to be measured with an absolute accuracy up to 0.05% and a resolution of 10^{-5} of the full-scale reading. One such sensor is connected to each of the metering volumes (PT102 and PT104). A third Baratron is placed in a linking pipe to the cold bore in order to measure the pressure of the gas in the cold bore (PT203).

Cryogenic pressure sensors

The cryogenic pressure transducers are of the same type as for the ^{4}He provisional gas system. For the ^{3}He we install an additional sensor in order to have a measurement at each extremity of the cold bore (PT204 and PT205).

These sensors work on a pressure range up to 1.7 bar and tolerate an overpressure up to 3.4 bar.

Vacuum gauges

Vacuum gauges are installed on several locations to monitor the evacuation of the system (PT106, PT202, PT212 and PT312). These are to be particularly important before the ^{3}He is transferred into the system to assure that a good vacuum is achieved and to assure that degassing from surfaces is at a low rate.

They are important as well to help in the calibration of the accurate pressure sensors (these need a vacuum better than $1x10^{-5}$ mbar).

Pressure indicators (PI)

The pressure indicators or manometers allow the operators to check locally the pressures at critical points, without access to the slow control system or PLC. This may be particularly important in the case of power failures or other abnormal conditions.

Electro-pneumatic valves (PV valves)

These shut-off valves have different tasks depending of the region where they are installed. Electro-pneumatic actuators were chosen for their speed and ability to be commanded remotely, because most of these valves are also located in regions of difficult access, or are used repetitively in standard operations.

All of these valves are bellows sealed type, which ensure leak-tightness to helium below 10^{-9} mbar·l·s^{-1}. These electro-pneumatic valves have an in-built safety mechanism which allows the valve to open for differential pressures higher than 2 bar.

The following table gives details on the use and location of each component:

Valve Name	Description
PV101, PV102	Used for the operation of filling the metering volumes with a new batch of gas from the storage volume.
PV105, PV106	Used for transferring gas into the magnet cold bores from the metering volumes.
PV108, PV112	Used in the operation of pumping the cold bore to the metering volume.
PV109	Allows the metering volume to be emptied into the storage volume.
PV207, PV208	Placed at each end of the expansion volume. These should open in case of quench as part of the first step of the recovery operation (activated by the quench trigger). These are normally open valves and by definition they open in absence of electrical power or compressed air.
PV211	Placed on the line connecting the hermetic ^{3}He pump to the expansion volume. This valve is used in the second phase of the recovery operation, to allow the evacuation of the expansion volume back to the storage volume. It is used either when the main ^{3}He pump is running, or when the pressure in the storage volume is lower that of the expansion volume.
PV212	Placed on its outlet of the turbo pump P212. Opens when the pressure is low enough in the expansion volume ($<10^{-1}$mbar) for the turbo pump (P212) to start.
PV308	Used on the second phase of recovery. In the case that the pressure in the expansion volume exceeds that of the storage volume this valve is opened (the main ^{3}He pump is not initially necessary until the pressure in these two volumes is balanced).
PV306	Used in case of quench to allow the gas to be sent to the storage volume after passing the main ^{3}He pump.
PV314	Placed at the inlet port of the main ^{3}He pump and it is opened whenever the pump is running.
PV310	Used for pumping the gas from the storage volume to the metering volumes.
PV305	Used to allow the gas to flow into the purification traps before entering the metering volumes.

Compressed air outlets should be foreseen with large buffer volumes and a safety back-up supply to secure pressure during electric power failures. A monitoring and alarm system will be required to trigger valve actions in the event of a decrease in the compressed air pressure.

Cryogenic check valve

This valve (NV202) allows the evacuation of the gas from the cold bore in case of quench, and will open at 30 mbar differential pressure. The main characteristics are reliability at cryogenic temperatures, a reasonably low in-line leak rate when closed, low differential pressure for opening and high conductance when open. This valve has a nominal diameter of 32 mm.

This valve is installed inside the cryostat on the gas line that connects the cold bore to the expansion volume on the MFB side. Its size was minimized because of the very limited space, while the hydraulic diameter is maximized for a good conductance.

The installation of this valve requires modification of the pipework inside the cryostat which includes cutting and welding of pipes in situ. To complete this task an integration study of for the new routing had to be made.

Cryogenic valves

These valves will allow the separation and communication between the cold region and the regions at room temperature. Their main purpose is to almost close the buffer gas lines at the highest temperature gradient, in order to eliminate the thermo-acoustic oscillations. These lines cannot be entirely closed, however, because the buffer gas needs to be loaded in and it has to be pumped out, and the cryogenic pressure gauges need to be calibrated against the accurate Baratron sensor outside the cryostat at room temperature.

Cryogenic Electro-pneumatic valve

On the MRB side the valve PV205 is used for pumping the cold bore to a good vacuum, since on the MFB side the check valve will only open unidirectionally by pressure gradient.

This valve, has a conductance of the same order of magnitude as the pipe work, and during normal operation is closed, except when the cold bore has to be pumped or in case of quench (commanded by quench trigger).

The main characteristics are reliability at cryogenic pressures, a reasonably low in-line leak rate when closed, low heat conductance to the magnet and possibility to be remotely commanded.

This valve is installed on the MRB side inside the cryostat on the gas line that connect the cold bore to the expansion volume, and its size should be minimized because of very limited space while maximizing its diameter for a good conductance.

Since the actuator of the valve is placed outside the magnet cryostat, an additional mounting port is necessary for installation. Moreover since a new routing of the pipe work is necessary an integration study was made.

Cryogenic needle valve

The cryogenic electro-pneumatic valve and the cryogenic check valve will be bypassed by small cryogenic needle valves CV203 and CV206 to balance the pressure of the gas upstream and downstream, while reducing the flow so as to damp the TAO.

These bypass valves are connected with 2 mm capillary tubes, and their orifices have a diameter of 0.7 mm. Similar type of needle valves have been used at CERN in the ^{3}He gas systems of dilution refrigerators in polarized targets and its design has been adapted to fit CAST needs.

To ease the installation the valve is mounted with Kenol® type metallic connections which confer a good leak tightness level.

The fabrication of this valve requires a vacuum brazing and full penetration welding in thin walled tubes that was performed by experts from the Cryolab and CERN main workshop. The leak-tightness is assured by double compression seal fitting at room temperature.

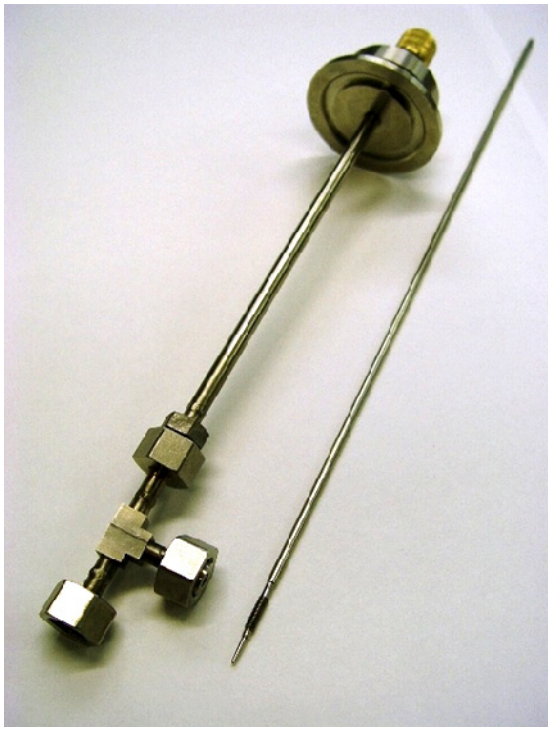

Figure 6-8: Picture of the customized cryogenic needle valve. The design of this valve allows an easy installation. Here most of the connections are tested in laboratory, and a minimum of connections tested in situ. It allows an easy control of the flow by adjusting a knob placed at room temperature.

Mass flow controllers

The control valves CV107 and CV111 are part of the mass flow controllers and are operated by an electromagnetic coil, the control is done relative to the set point on the desired mass flow. These flow controllers enable the ramping of the buffer gas density by providing a constant mass flow rate.

The valve CV107 is used for ramping up the density in the cold bore, and the gas will be driven by the differential pressure between the metering volume and the cold bore.

The valve CV111 is used for ramping down the density in the cold bore, and the gas will be driven by the differential pressure between the cold bore and the vacuum at the inlet of the small ^{3}He pump, P111.

Gate valves

Two gate valves, HV201, HV204, placed at each end of the gas lines coming from the cold bore allows to isolate the cold bore and to make manipulations on the outside without the risk of damaging the X-ray cold windows, or any leakage from the ambient. These valves are kept open and only be closed in very exceptional conditions.

Shut-off valves

There are several shut-off valves placed on different regions of the circuit; basically these valves assure very rare manipulations and/or are ports for pumping and leak testing. These valves are manually operated and have a bellows sealed type construction which allows to achieve very low leak rated $<10^{-9}$ mbar·l·s^{-1}.

Rupture Disks

Following the suggestions of the Technical Design Report review committee, 2 rupture disks are foreseen to be mounted into the system. One rupture disk designed for rupture pressure of 2 bar to connect the expansion volume with the storage volume. A second one is to be mounted directly in the cold bore with a rupture pressure of 3.7 bar to evacuate directly into the cryostat vacuum. This device provides ultimate safety against the worst failure conditions, including the failure of the safety interlock system. Both rupture disks are designed to withstand 1 bar differential in the inverse to the nominal direction.

Valves and fittings

All valves and fittings are chosen to be leak tight to ^{3}He, to avoid any loss of helium and all fittings are preferable UHV fittings or other all-metal sealed connections.

Instrumentation

Temperature sensors and heaters of different types are installed in critical regions similarly to what was done for the ^{4}He system. They are positioned especially in regions near the cold bore, window flanges, filling lines, thermostatic bath, and additionally were added to the cryogenic valves body and magnet cold mass face.

Heaters are installed on the cold window flanges. These allow, if necessary, to increase or maintain the windows at a constant temperature, and to periodically bake-out possible trapped gases from the X-ray window foils. The solution adopted so far is to maintain the window flanges at 120 K, and to make monthly bake-outs to assure a good transparency.

Although most of the components of the ^{3}He gas system are controlled and supervised by a dedicated PLC, there is nevertheless a variety of signals that are directly read by the gas system slow control DAQ. The following diagram simplifies the structure:

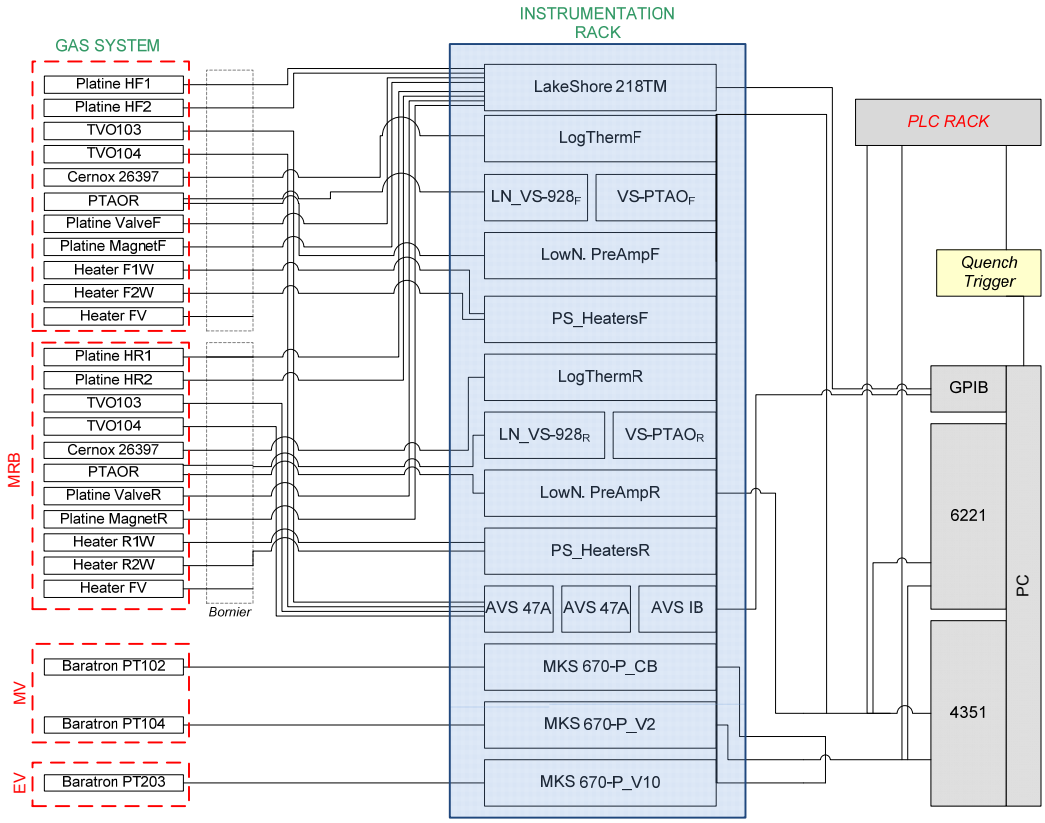

Figure 6-9: Instrumentation layout for the gas system slow control DAQ, similar to that of the ^{4}He gas system with some improvements.

6.4 Safety Interlocks to protect against loss of ^{3}He

The X-ray windows are clearly the weakest part of the hermetic gas system. The windows have a strongback on the vacuum side and they are tested to withstand 1.2 bar pressure difference between the cold bore and the vacuum.

They may break at substantially higher pressure, and will certainly fail already at much lower pressure when applied on the vacuum side. There will therefore be precautions against the loss of ^{3}He in the event of a rupture of one of the windows.

The identification of scenarios which can lead to the rupture of one of the windows is an important tool for increase the safety against loss of ^{3}He and to improve the system reaction. Although with very remote probability of occurrence, either due to the construction concept or due to the existing means of diagnose, a set of scenarios is listed:

- A large leak of air into the part of the ^{3}He pipework that is open to the cold bore tubes. The cryo-pumped air would accumulate on the cold surfaces, and would degas during a wrong manipulation of the cryogenic circuit. This could potentially give rise to a pressure that could endanger the windows, if the ^{3}He system would not be evacuated and monitored during the magnet warm-up. It should be noted, however, that a quench raises the temperature of the magnet bores only to about 40 K temperature, which is too low for the cryo-pumped air to degas.
- A wrong manipulation or a large air leak in the vacuum side of the window causing it to break because of a pressure gradient in the wrong direction.
- A small leak of a detector window, followed by the cryo-pumping of one of the detector gas components onto the cold surfaces of the vacuum pipe between the two windows. This would require, however, that the cryogenic circuit is not operated under normal conditions, where there is no risk of cryo-pumping of any of the main components of the detector gases.
- A mechanical failure of a window caused by fatigue.
- A mechanical failure of the window caused by unknown factors.

In all of the above scenarios the gas confined inside the cold bore could flow through the broken window and be pumped out by the vacuum pumps that evacuate continuously the sector of beam tubes between the windows of the detectors and the cold windows.

To avoid such a release of ^{3}He into air, the following interlocks are implemented:

- In case of quench, the electromagnetic valves which isolate the cold bores from the detectors (VT1, VT2, VT3, VT4), must immediately close to protect the detectors of contamination or unwanted pressurization (this is already an established procedure).

- In case of a cold window rupture, the vacuum side of the window will need to be isolated from the vacuum pumps and from the detectors. This is implemented by monitoring the pressure on the vacuum side using several highly reliable Pirani vacuum gauges, and in case of rapid rise of pressure, valves will close to isolate the lines. After that the ^{3}He gas (possibly slightly contaminated by the gases that leaked in) will be pumped back to the storage tank, and the cold windows will be repaired.

The purification of the ^{3}He gas after a contamination will take place by sending the whole inventory through the traps to the magnet bore tubes, and then pumping it back to the storage vessel. The traps and the 1.8 K cold bores will remove all possible impurities except ^{4}He.

6.5 Integration an Installation

The ^{3}He gas system components are distributed all over the CAST experimental area. Since the CAST experiment is a non-static experiment, in order to assure no interference with the existing facilities important integration studies had to be carried out.

One of the most complex studies is the new pipe work routing inside the magnet cryostat, since a new cryogenic valves have to be installed at both the MRB and MFB extremities.

Inside the cryostat the components are submitted to large temperature variations, from their nominal operating temperature to the ambient temperature when its installation is taking place. For this reason important considerations have to be made about thermal contraction coefficients and possible structural stresses.

Three-Dimensional modelling was done to integrate the new components within very limited space available. In Figure 6-10 it is shown the proposed design for the MRB side, where the cryogenic electro-pneumatic valve is to be installed.

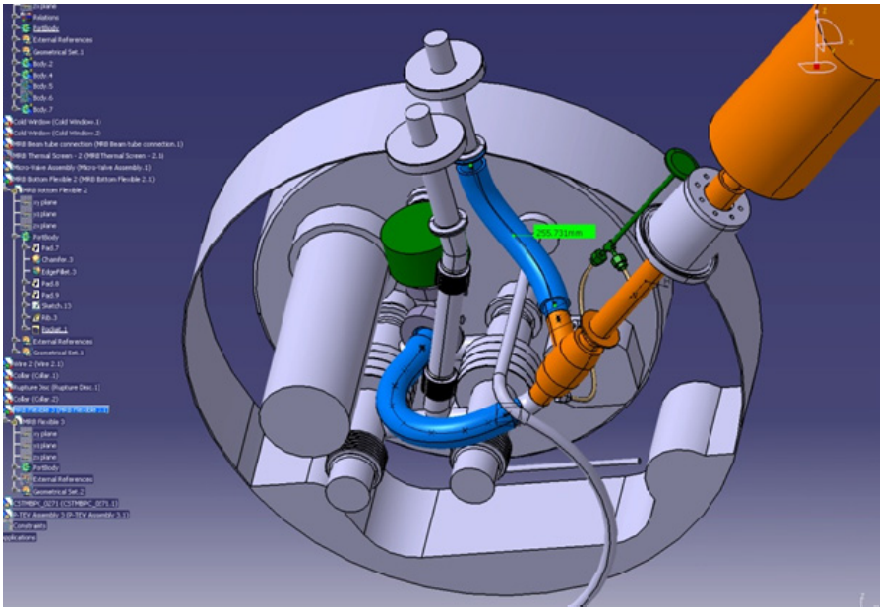

Figure 6-10: Mechanical integration 3-D model of the components inside the cryostat (MRB side). In the picture it is shown the new cryogenic electro-pneumatic valve (orange), the new pipework (blue) makes the connection of the valve with the line that exits the cryostat and the line that connects to the cold bore. The new rupture disk and needle valve is also presented (green).

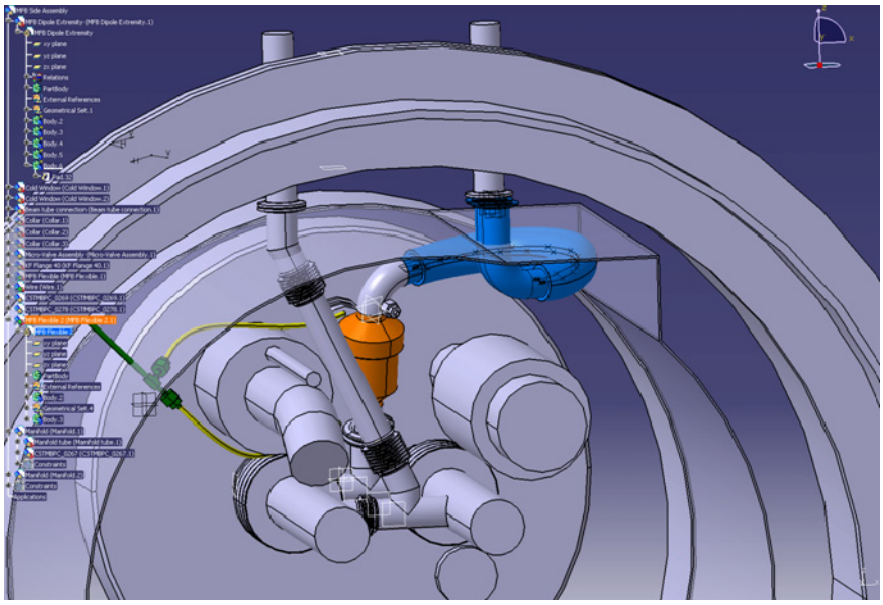

Figure 6-11: Mechanical integration 3-D model of the components inside the cryostat (MFB side). In the picture it is shown the new cryogenic check valve (orange), the new pipework (blue) makes the

connection of the valve with the line that exits the cryostat and the line that connects to the cold bore. The new needle valve is also presented (green).

From the above pictures it is possible to see the complicated routing that the new pipe work has to follow in order to remain within safe values for the bending radius and avoid touching other equipment. One gets a feeling of the difficulty of modification work which is necessary comprising difficult welds and sensible pipe cutting in such a crowded region.

The following pictures complete this explanation showing works inside the cryostat.

Figure 6-12: Pictures of the intervention inside the Cryostat. Top: Welder working on the MFB side. Bottom: welder working on the MRB side.

In Figure 6-12 we show the difficulties behind the mechanical intervention inside the cryostat. This highly qualified welder had sometimes to utilize mirrors to perform its welds, and other times he was placed in very complicated positions to perform his tasks. Protection sheets were put around the MLI in order to avoid deflagration of fire and aluminium foils protected the knife edges of the X-ray window flanges.

Figure 6-13 shows a view of the final installation of the storage volume. Also visible are the LN2 dewar for the purification traps (on the right side of the picture). The main ^{3}He pump is also visible which is enclosed in a plexiglass frame for protection of the numerous instruments placed in this crowded region.

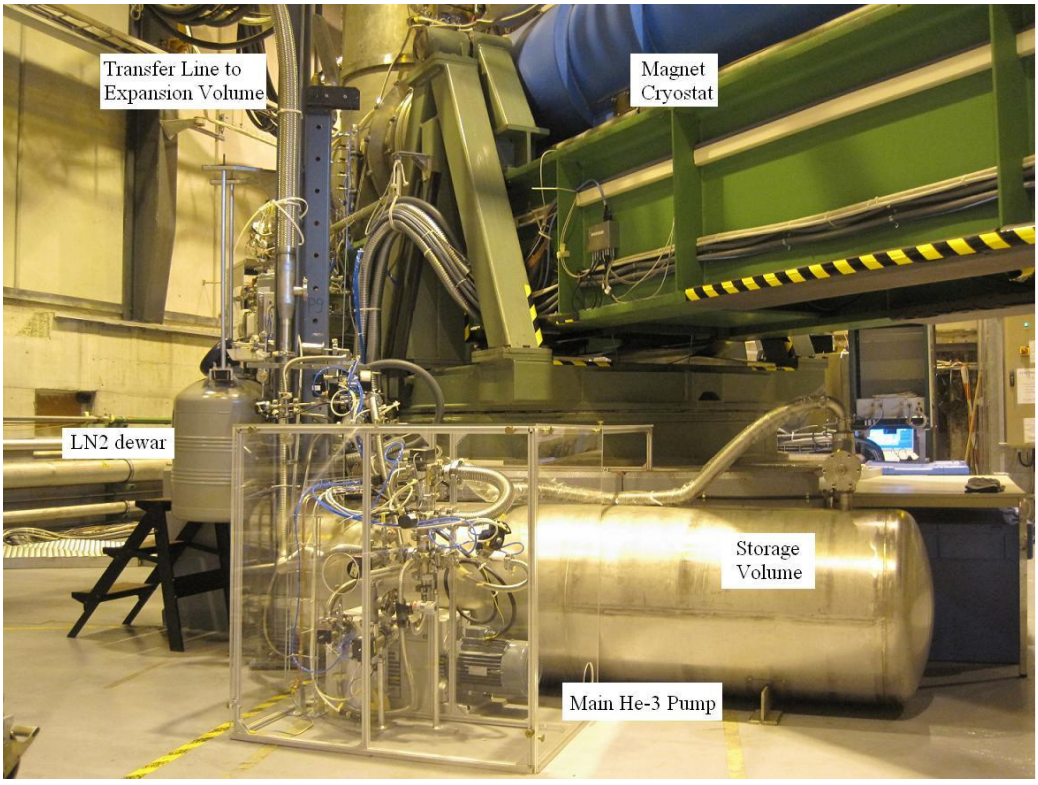

Figure 6-13: Picture of the Storage volume and auxiliary equipment.

6.6 The Programmable Logic Controller

The use of a Programmable Logic Controller (PLC) was chosen for control and supervision of the system. The reasoning for this decision falling on the high complexity of the ^{3}He gas system, either because of the large number of signals, or various possible modes of operation or large number of instruments to monitor continuously.

The PLC system allows the remote operation of valves and pumps using a computer interface where the synoptic of the system is displayed; it also allows the initialization of pre-programmed operations that have to be done routinely such as transferring gas to the metering volumes or cold bore, or engaging in a sequence of operations to recover the gas in case of quench.

Another advantage of the PLC is that it also allows the data logging of any equipment states, or instrument values that are to be recorded in a central database.

The ^{3}He Control system has been designed using the standard control architecture developed at CERN for the cryogenics systems (LHC and Experiments) called UNICOS - UNified Industrial COntrol System [31].

UNICOS is an industrial framework developed to produce control applications for the typical approach of three-layer industrial control systems. UNICOS proposes a method to design and develop the complete control application based in a specification dossier where all the I/O channels and field objects (e.g.: pumps, valves, position switches) are described.

Current UNICOS implementation targets Siemens and Schneider PLCs at the control level and PVSS II® at the supervision level.

It provides flexibility and operation facilities due to a standard design of the interface, and ensure its durability by support and expertise resources at CERN. It is based on simultaneous generation of PLC and SCADA devices, diagnostics tools, and object-oriented programming with specific hierarchy, and results in rapid prototyping and optimal regeneration mechanisms.

In the CAST ^{3}He gas system the PLC is structured as shown in the Figure 6-14.

In the ‘Process Control Object’, the global logic is described and also any interlocks or tasks that are to be pre-programmed (option modes). Under this layer, individual objects (representing real components) are described, specifying its own states and

interlocks. Finally the I/O channels serve to describe the way the communication between the field equipment and the PLC is done.

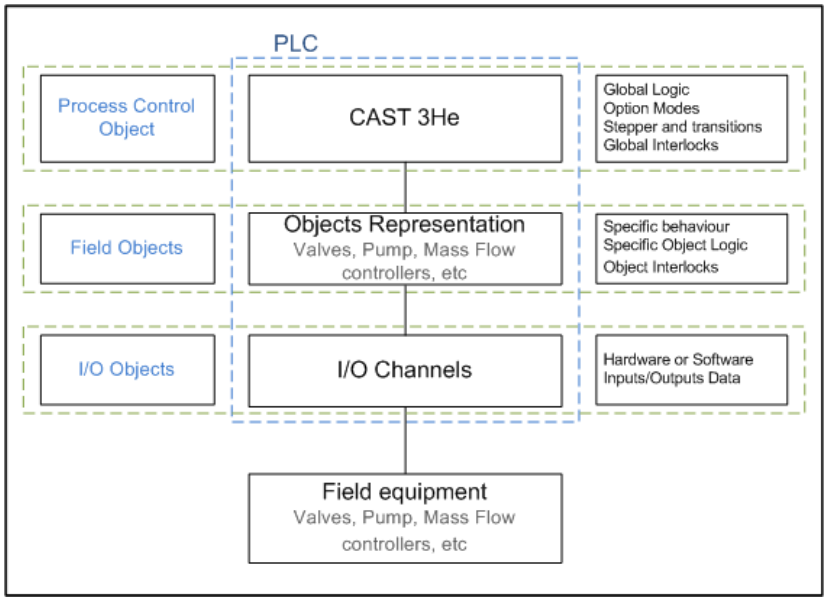

Figure 6-14: UNICOS based control system. Architecture of the control system comprising the PLC and the field equipment.

The field equipment is distributed all around the experimental zone (Figure 6-15), the first step is to identify its location and lay down cable routes for bringing the signals into the PLC rack through the I/O channels.

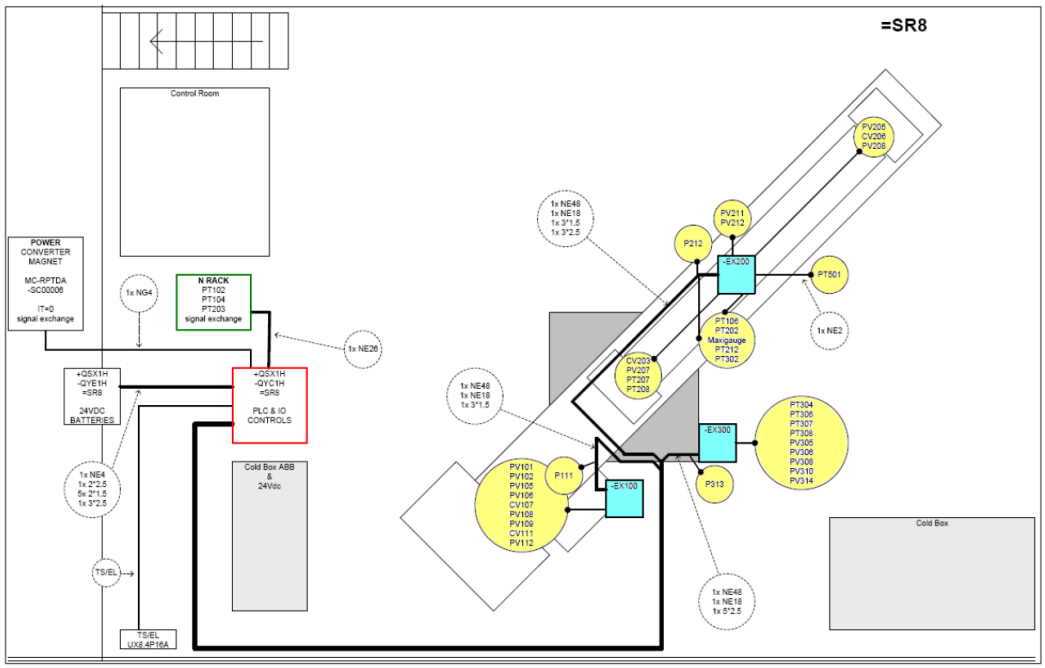

Figure 6-15: Electrical distribution layout of the ^{3}He gas system PLC. This schematic diagram represents the electrical layout in the CAST experimental zone, where in the center of the picture is the 10 m magnet and in the top left corners the CAST Control Room. The red box represents the ^{3}He PLC rack and the green box is the gas system slow control rack. Inside the yellow circles are the names of the field equipment which are first connected to the electrical switchboxes (blue boxes) from where the signals are grouped. Thick black lines represent the routing of the electrical cables.

The PLC rack is connected to the electrical network and it has its own Uninterruptable Power Supply (UPS) consisting of 2×12 V batteries with a total capacity of 100 A·h.

The communication between the field equipment and the PLC is made through Inputs and Outputs. There are several types of I/O consisting of:

- Digital Input (ex: position switch on of a valve, either ON or OFF)
- Digital Output (ex: alarm sign, either ON or OFF)
- Analogue Input (ex: current output of a pressure sensor, 4 to 20 mA)
- Analogue Output (ex: set point of a mass flow controller, 4 to 20 mA)

Similar to the ^{3}He gas system schematic diagram, the PLC main graphical user interface (GUI) consists of a synoptic diagram representing the real implementation (Figure 6-16). The advantage is that one can have a general view of the status of each

individual controlled object just by looking at the monitor, and also other important information concerning the status of the operations.

Different user accounts specify different the access rights, which allows people with less experience the get acquainted to the system without the danger of human errors, or people with more experience to perform commissioning operations outside the pre-programmed operations:

Account	Rights
Monitor account	*Allows monitoring of the system status*
Operator account	*Allows monitoring + running pre-established operations*
Expert account	*Allows manipulation of all objects*
Admin account	*All rights*

It is possible to visualize the preferences of an individual object, check or modify its status by 'clicking' on it, or see a timeline with the status or value of each instrument. Moreover since the PLC is built on a PVSS platform any computer can load the CAST ^{3}He project and supervise the system.

Additionally it is possible to save and load pre-defined histograms, to display for example: the values of specific pressure probes which are of importance whilst performing a specific operation.

From the main GUI it is possible to start a predefined routine operation or to navigate to other 'screens' displaying for example:

- List of DI, DO, AI, AO and states.
- List of Alarms and Interlocks
- List of used setpoints
- List of previously performed actions

All these tools are a great asset specially for diagnosis and commissioning, and in our case are all integrated in the same platform.

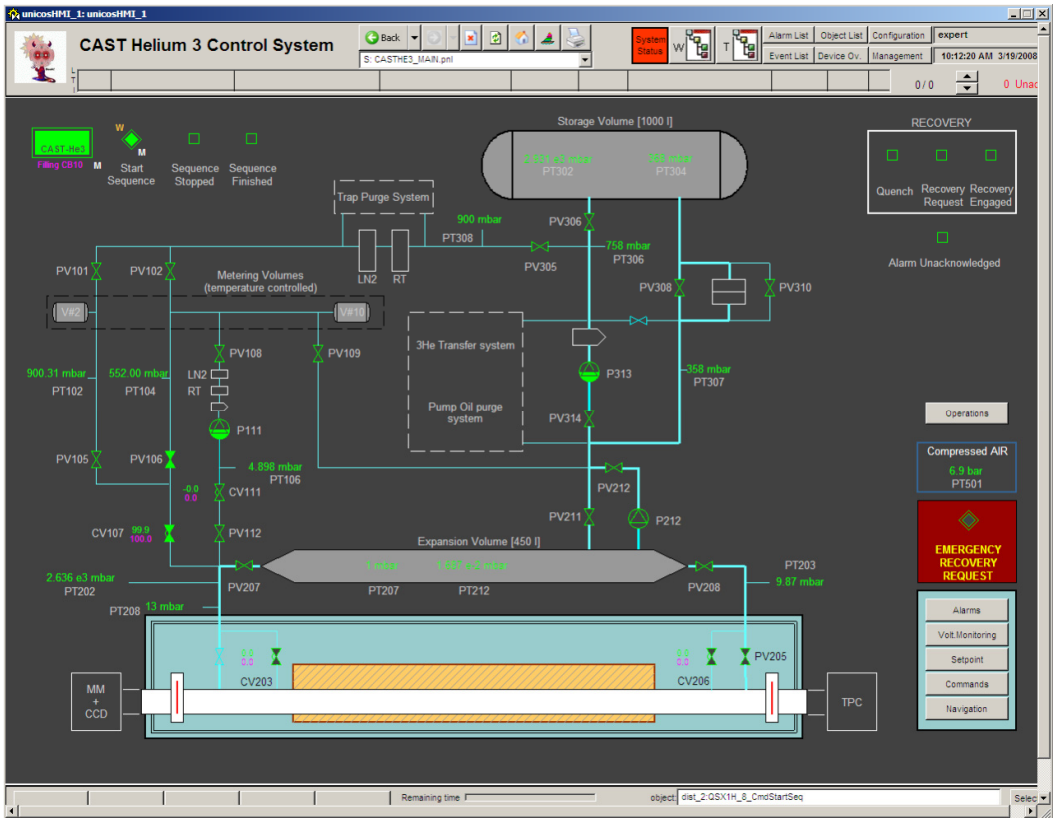

Figure 6-16: Main graphical user interface of the ^{3}He Gas system PLC.

The ^{3}He Gas system benefits from the LHClogging[24] for long term archiving and also the Technical Infrastructure Monitoring user Interface (TIMBER) for process data analysis.

This application, initially developed for the LHC, provides a set of tools, templates and other software components to ensure the functionality of a long-term data logging facility for CAST ^{3}He gas system.

The main functionalities of the software are:

- To receive pertinent data from LHC systems and store this data centrally. The ^{3}He gas system of CAST was included as a sub-system.

[24] http://lhc-logging.web.cern.ch/lhc-logging/

- To be able to choose and retrieve data of interest from the central repository, pre-process it if needed and present the data by means of the user interface or transfer the data to external software tools.
- To make easy comparisons between different parameters, and thereby detect a given correlation.
- To have an effective tool for displaying data versus time.

By using this application, it is possible to benefit from TIMBER, which is a web application running from a JAVA API, which enables the users to get to selected logged variables, show their data graphically, and extract the data in a file format. This application is also used by the LHC operation and most of the experiments.

7 Conclusions

This thesis project was set out to develop a reliable gas handling system for the CAST Second Phase, allowing the experiment to extend its axion search above the axion mass limit of 0.02 eV/c^2 reached in the First Phase of CAST where a sensitivity of $g_{a\gamma} = 8.8\times10^{-11}$ GeV^{-1} (95 % C.L) was achieved.

To restore the lost coherence and extend the search to higher axion masses, a buffer gas has to be introduced in the magnet cold bores, such that the emerging photon from the Primakoff conversion acquires an effective mass.

The introduction of a buffer gas with a given density inside the magnet cold bores allows the axion conversion to be coherently done over a very narrow mass range. Therefore, to scan over the available range of masses, accurate steps in density have to be made, such that all masses can be scanned with a maximum sensitivity.

Since the magnet is cooled with superfluid helium at a nominal temperature of 1.8 K, only two elements remain gaseous below their saturation pressure: the abundant ^{4}He and its other stable isotope ^{3}He, which is very rare and expensive.

To ensure a good stability, homogeneity and reproducibility a detailed study was carried out, to quantify the effects of temperature fluctuations and temperature gradients in the magnet extremities.

Generally, superconducting magnets in particle accelerators are used to bend the trajectories of particles, or focus beams before collisions, in those conditions a good vacuum level is an important requirement. The introduction of a buffer gas inside the cold bores of a superconducting LHC magnet is thus an exercise without precedents that had to be studied with great care.

In the CAST setup, the buffer gas needs to be contained in the magnetic field region with elements able to sustain the differential pressure, but also be designed to maximize the X-ray transmission in the important energy range. The development of cold thin X-ray windows resulted in the publication of an impressive study. We were able to design, test and produce, elements meeting both the requirements of hermeticity, mechanical robustness and X-ray transmission for physics runs.

The study of the magnet transient behaviour during a resistive transition was also studied and measured. The results of these measurements allowed the design of safety measures to rescue the gas from the cold bore during the rapid warm up.

The study of thermodynamic phenomena such as spontaneous themo-acoustic oscillations was also subject of analysis, since its occurrence would have detrimental consequences to the gas density distribution along the magnet axis. These studies revealed that the original CAST setup would require modifications in order to eliminate this effect. Active and passive prevention measures were implemented, resulting in the complete elimination of the phenomena.

A provisional gas handling system for ^{4}He runs was designed, tested and built. It served as an important tool to prepare for the more complex final system. Successful data-taking physics runs were carried out during the year 2006 and 2007 using this system.

This provisional gas system allowed CAST to enter for the first time the theoretical models favoured band, establishing an impressive new limit of $g_{a\gamma} = 2.17 \times 10^{-10}$ GeV^{-1} in the range $0.02 < m_a < 0.39$ eV/c^2 (95 % C.L).

Important lessons were learned from the operation with ^{4}He, which were taken in consideration on the design of the final ^{3}He gas system. Here, due to the increased level of complexity, flexible modes of operation were required. Moreover, due to the rarity of the gas in use and its inferred cost, great deal of care was put in the choice of materials, equipment, and supervision and diagnostics tools.

One important achievement was the implementation of a Programmable Logic Controller for control and supervision of the system, which allows the remote operation of the controlled equipment and verification of states, but also the possibility for a continuous improvement of the system by adding control flags and interlocks.

The operation with ^{3}He started in April 2008, since then more than 550 density settings have been scanned, with an equivalent axion mass coverage up to 0.76 eV/c^2, making this experiment the one having gone further into the axion favoured region with higher sensitivity.

It's been a long way from the starting point, where the reach of axions with higher masses than 0.02 eV/c^2 was just a creative thought. Presently, with each day new physics territory is explored, and with each day, the possibility to be one step closer to an axion signature.

Appendix A

Here is presented an overview of the problem in Quantum Chromodynamics that gave rise to the postulation of a new particle called the axion, along with its properties and searches.

A.1 A solution to the strong CP-Problem

A puzzling question in particle physics is the strong CP-problem, where Quantum Chromodynamics (QCD) does not seem to break the Charge-Parity (CP) symmetry. In QCD the strong interactions of hadrons is described in terms of the interactions with their quark and gluon constituents via the Lagrangian [32]:

$$\mathcal{L}_{QCD} = -\sum_f \overline{q}_f \left(\gamma^\mu \frac{1}{i} D_\mu + m_f\right) q_f - \frac{1}{4} G_a^{\mu\nu} G_{a\mu\nu}. \quad \text{(A.1)}$$

The QCD Lagrangian (for f flavor of quarks) has a global symmetry in the limit when $m_f \to 0$ given by: $G = U(f)_R \times U(f)_L$. The $U(1)_V$ subgroup of the $U(2)_R \times U(2)_L$ symmetry corresponds to the vectorial $(V = R + L)$ baryon number and is an exact symmetry of QCD. On the other hand the corresponding axial $(A = R - L)$ symmetries $U(1)_A$ are not preserved in the QCD vacuum.

Whenever a continuous global symmetry is broken a Nambu-Goldstone boson is created, a massless spin-zero boson corresponding to the remaining symmetry. However if the symmetry is not exact the particle will have a small mass and it is called Pseudo-Goldstone boson.

For a possible $U(1)_A$ symmetry breaking of QCD four Goldstone bosons are expected, but it turns out that only three of them have been observed, namely the pion triplet π^+, π^0, π^-.

The idea presented by t'Hooft, by postulating the anomalous breaking of $U(1)_A$ symmetry, allows a solution to the $U(1)_A$ problem. The anomaly is known as axial or Adler-Bell-Jackiw anomaly and it adds $\mathcal{L}_\Theta$ to the QCD Lagrangian:

$$\mathcal{L}_\Theta = \Theta \frac{g^2}{32\pi^2} G_a^{\mu\nu} \tilde{G}_{\mu\nu}^a, \quad \text{(A.2)}$$

with the coupling constant g and $\tilde{G}_{\mu\nu}^a$ the dual of the gluon field strength tensor.

This new Lagrangian exists due to the complicated structure of the ground state, which is formed by an infinite number of vacuum states. The distinct vacua can be

characterized by the winding number n, and the ground state can be expressed by a superposition of the degenerate vacua, $\Theta - vacuum$:

$$|\theta\rangle = \sum_{n=-\infty}^{\infty} e^{-in\theta}|n\rangle, \quad \text{(A.3)}$$

for $0 \leq \Theta \leq 2\pi$.

For the Standard Model, in order to consider the electroweak interactions, Θ has to be substituted by $\overline{\Theta}$, which is given by:

$$\bar{\theta} = \theta + arg(detM), \quad \text{(A.4)}$$

Where M is the quark matrix.

The $U(1)_A$ problem can thus be solved with the expense of raising another problem $\mathcal{L}_{\bar{\Theta}}$ violates the CP symmetry. No strong CP-problem would appear if at least one quark was massless, but since this is not the case, this requires a fine tuning of the two independent terms of the above equation.

Electric dipole moments are the most interesting parameters connected to CP violation. The electric dipole moment of the neutron has a strong experimental bound at $|d_n| \leq 12 \times 10^{-26}\ \mathrm{e} \cdot \mathrm{cm}$. However, a simple dimensional analysis of this quantity yields a value for $|d_n| \sim 10^{-16}\ \overline{\Theta}\ \mathrm{e} \cdot \mathrm{cm}$, thus implying $\overline{\Theta} < 10^{-10}$.

The smallness of $\overline{\Theta}$ requires an extreme fine-tuning of Θ and $arg\,(detM)$, the question of the smallness of is also known as strong CP-problem.

An elegant solution for this problem was given by Peccei and Quinn, requiring the extension of the Standard Model with an additional, spontaneously broken, global chiral symmetry, the $U(1)_{PQ}$, the result from the breaking of this symmetry is a pseudo Nambu-Goldstone boson, called *axion*.

Basically, what happens is that by incorporating this symmetry in the theory one replaces the static CP violating parameter $\overline{\Theta}$ by the dynamical (CP conserving) interactions of the axion field.

Because the axion field $a(x)$ is the Nambu Goldstone boson associated with the spontaneously broken $U(1)_{PQ}$ symmetry, this field translates under a $U(1)_{PQ}$ transformation. If α is the phase parameter of this transformation and f is the scale associated with the breakdown of the symmetry, one has:

$$a(x) \overset{PQ}{\rightarrow} a(x) + \alpha \cdot f_a \,. \tag{A.5}$$

Due of the chiral anomaly of this symmetry, the axion will couple to gluons, resulting in the appearance of an extra term in the Lagrangian, which is linearly depending on $a(x)$:

$$\mathcal{L}_{AXION} = \frac{a(x)}{f_a} \xi \frac{g^2}{32\pi^2} G_a^{\mu\upsilon} \tilde{G}_{a\mu\upsilon} - \frac{1}{2} \partial_\mu a \partial^\mu a + \mathcal{L}(\partial_\mu a, \psi). \tag{A.6}$$

Here the second term represents the kinetic energy of the axion field, and the last term the possibility of interaction between the axion field and a fermion ψ. The first term of the equation gives the axion field an effective potential where ξ is a model dependent coefficient. It allows the axion field to relax not in all values of vacuum, but only in those that minimize this potential:

$$\langle \frac{\partial V_{eff}}{\partial a} \rangle = 0 \implies \langle a \rangle = -\frac{f_a}{\xi} \overline{\theta} \,. \tag{A.7}$$

With the introduction of an additional axion field, it is possible to eliminate the disturbing $\overline{\Theta}$ term in the QCD Lagrangian, no violation occurs and therefore the strong CP-problem is solved (other alternative approaches to solve the strong CP-problem exist, one of them using supersymmetry is found in [33]).

A.2 Axion Properties and couplings

The axion properties and couplings depend on the breaking of the f_a scale of the Peccei-Quinn symmetry. The most significant feature is that the axion couplings g_{aii} are proportional to $1/f_a$or equivalently to m_a.

Axions interact with fundamental bosons, such as gluons or photons, as well as with fermion like electrons and nucleons.

The coupling of axions with gluons is due to the chiral anomaly and is described by:

$$\mathcal{L}_{aG} = \frac{\alpha_s}{8\pi f_a} a G_a^{\mu\upsilon} \tilde{G}_{a\mu\upsilon} \,, \tag{A.8}$$

where α_s is the fine structure constant of the strong interactions. This coupling is the feature that distinguishes axions from other pseudoscalar particles, since is follows directly from every axion model. Through the coupling with gluons, axions acquire a mass, which can be derived from the mixing with pions:

$$m_a = \frac{m_\pi f_\pi}{f_a}\left(\frac{z}{(1+z+w)(1+z)}\right)^{1/2} \simeq 0.60eV\,\frac{10^7 GeV}{f_a}, \tag{A.9}$$

where the pion mass is $m_\pi = 135\ \mathrm{MeV/c^2}$ and its decay constant is given by $f_\pi = 93\ \mathrm{MeV}$. Here z and w are the quark mass ratios [34]:

$$z \equiv \frac{m_u}{m_d} = 0.568 \pm 0.042 \tag{A.10}$$

$$w \equiv \frac{m_u}{m_s} = 0.029 \pm 0.0043 \tag{A.11}$$

For the value of z there is a significant uncertainty according to the reference [35], which states z between 0.3 and 0.7 while according to [36] $z = 0.553 \pm 0.043$.

The axion coupling with photons [37], which is of main relevance in the CAST experiment, is done via a triangle loop through fermions carrying PQ and electric charges, and through axion-pion mixing. The two Feynman diagrams shown in Figure 7-1 display these interactions.

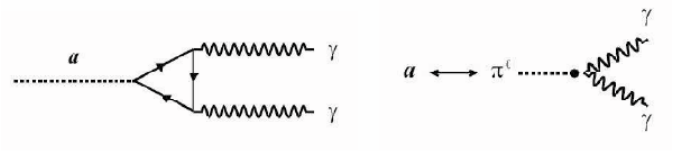

Figure 7-1: Axion coupling with photons represented by Feynman diagrams. On the left the coupling to fermions carrying PQ charge and on the right from the axion-pion mixing.

The Lagrangian of this interaction can be written in the form:

$$\mathcal{L}_{a\gamma} = \frac{g_{a\gamma}}{4} F_{\mu\upsilon}\tilde{F}^{\mu\upsilon} a = g_{a\gamma}\vec{E}\cdot\vec{B}a\ , \tag{A.12}$$

where $g_{a\gamma}$ is the coupling constant, F the electromagnetic field tensor, E the electric field and B the magnetic field. The coupling constant can be derived as:

$$g_{a\gamma} = -\frac{\alpha}{2\pi f_a}\left(\frac{E}{N} - \frac{2}{3}\frac{(4+z+w)}{(1+z+w)}\right) \simeq \left(\frac{E}{N} - 1.92 \pm 0.08\right), \tag{A.13}$$

where α is the fine structure and E/N depends on the axion model for E representing the electromagnetic anomaly and N the color anomaly of the axion current [37].

Axions couple with fermions and the Lagrangian of the interaction can be written as:

$$\mathcal{L}_{af} = \frac{g_{af}}{2m_f}\bar{\Psi}_f\gamma^\mu\gamma_5\Psi\partial_\mu a\,, \tag{A.14}$$

where here the f index denotes the fermion (electron or nucleon). For the fermion of mass m_f, the coupling constant is given by:

$$g_{af} = \frac{C_f m_f}{f_a}. \tag{A.15}$$

A.3 Axion models and limits

Axions can be classed in the context of different models. The distinguishing feature between the two major axion models is the size of the Peccei-Quinn scale f_a, that is inversely proportional to the axion mass m_a.

The *standard axion model* was originally proposed by Peccei, Quinn, Weinberg and Wilczek (PQWW)[38][39][40], it assumed the decay constant to be of the same order of the electroweak scale. However, the existence of this kind of axions, also known as *visible* has been ruled out by numerous experiments as well as astrophysical considerations [41].

For weaker couplings of the axion, i.e. for a f_a scale much larger than a f_{weak} scale, the axion was so far unable to be detected in the previous experiments, thus the name *invisible.* In models of this kind, an electroweak singlet Higgs field with a vacuum expectation value of a $f_a/\sqrt{2}$ is introduced. In this regard the two important models are the KSVZ[25] and DFSZ[26].

In the KSVZ model [42] leptons and quarks do not carry PQ charge and as far as the interactions with photons are concerned different types of KSVZ models suggest different E/N values as in equation (A.13) and consequently this coupling can be either enhanced or suppressed [43]

Unlike the previous model, in the DFSZ model [44] fundamental fermions carry PQ charge. The ordinary Higgs field is substituted by two new ones. Since the DSFZ axions can be implemented in Grand Unified Theories (GUT) for a given family of quarks and fermions the ratio and E/N equals 8/3 making the coupling with photons to become:

$$g_{a\gamma}{}^{DFSZ} = 0.75\frac{\alpha}{2\pi f_a} \tag{A.16}$$

Cosmological and Astrophysics constraints on axion properties

The information on the axion coupling and mass can be derived by deducting what would be the evolution of the axion expectation value through the Universe lifetime. In the primordial Universe the value $\overline{\Theta}$ is conventionally equal to zero, but when the

[25] Named after the authors Kim, Shifman, Vainstein and Zakharov
[26] Named after the authors Dine, Fischler, Srednicki and Zhitnitskn

Universe cools down to a temperature in the same range as the PQ scale, the expectation value of the axion field assumes a value Θ_i(initial misalignment angle). When the axion mass becomes comparable with the Universe expansion rate, the axion field oscillates around its final dynamic value $\overline{\Theta} = 0$. The axions abundance $\Omega_a h^2$ can be expressed as a function of the misalignment angle:

$$\Omega_a h^2 \simeq 1.9 \times 3^{\pm 1} \left(\frac{1\mu eV}{m_a}\right)^{1.175} \Theta_i^2 f(\Theta_i), \tag{A.17}$$

where the Hubble constant is h^2 and any anharmonic corrections on the axion potential are incorporated in $f(\Theta_i)$. The result of the Wilkinson Microwave Anisotropy Probe (WMAP) gives a matter density $\Omega_m h^2 = 0.135^{+0.008}_{-0.009}$ [45], assuming an abundance of axions of the same order, with a mass in the μeV range, then they would be dominating the Cold Dark Matter of the Universe.

Since axion models have spontaneous breaking of $U(1)_{PQ}$symmetries, cosmic axion strings would appear in the case that inflation did not occur at all or if it did. Some controversy exists in this matter, where Battye and Shellard [46] assume that the energy of the axionic strings turn into axions, the mass density at which the produced axions would contribute becomes:

$$\Omega_{string} h^2 \simeq \left(\frac{m_a eV}{10^{-3}}\right)^{1.175} \Theta_i^2 f(\Theta_i) \tag{A.18}$$

Which would therefore restrict the axion mass to $m_a \geq 10^{-4}$ eV/c^2.

On the other hand, according to Sikivie [47][48] the string radiation is converted into kinetic axion energy, and wouldn't increase the density of relic axions significantly more than the misalignment mechanism, and therefore the axion mass could be restricted to $m_a \geq 10^{-6}$ eV/c^2.

It has been noted [49] that axions with a mass above 0.1 eV/c^2, could have lifetimes long enough to sustain that not all relic axions have decayed, and that a fraction decay also at present.

Despite their small interaction with matter, axions can have a considerable influence on the evolution of stars. Axions could be produced in the interior of stars, and therefore meaning a novel energy-loss mechanism that would have an important impact in the stellar evolution.

By demanding that the time scales of stellar evolution match the observational limits [37] it is possible to put limits on the coupling of axion to photons, electrons and nucleons. Horizontal branch stars and low mass globular clusters, with low-mass and

helium burning core have provided the best limit on axion-photon couplings, resulting in a coupling constant of $g_{a\gamma} \lesssim 0.6 \times 10^{-10}\,\mathrm{GeV}^{-1}$. Due to uncertainties of the determination it is often mentioned as globular cluster limit the value $g_{a\gamma} \lesssim 1 \times 10^{-10}\,\mathrm{GeV}^{-1}$.

Restrictive limits come from the observation of the supernova SN 1987A, when referring to axions produced by nucleon-nucleon-axion bremstrahlung. Results of Kamiokande II and IBM detectors [37], where the coupling of axions and nucleons is excluded in the range $3 \times 10^{-10}\,\mathrm{GeV}^{-1} \lesssim g_{aN} \lesssim 1 \times 10^{-7}\,\mathrm{GeV}^{-1}$, exclude KSVZ axions in the mass range $0.01\ \mathrm{eV} \lesssim g_{aN} \lesssim 10\mathrm{eV}$.

All these observations and calculations provide a small window for hadronic axions to exist. Figure 7-2 summarizes all these constraints.

Although these are the best astrophysical and cosmological limits, it has to be pointed out that these bounds have a considerable uncertainty; it has not stopped research to go inside these regions to set firmer bounds.

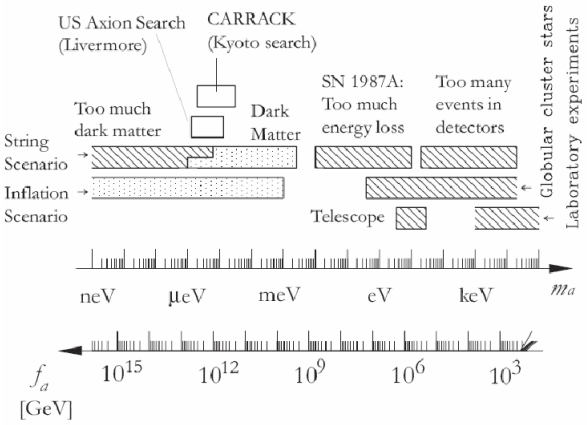

Figure 7-2: Summary of Astrophysical and cosmological exclusion regions for the axion mass, or equivalently the PQ scale. The Open-ended bars represent a rough estimate, i.e. its location is model-dependent or has not been established. Since the globular-cluster limit is derived from axion-to-photon coupling, it is model dependent. The limit from the SN 1987A depends on the axion-nucleon-coupling and thus, what is shown here is exact for KSVZ and approximately for DFSZ axions. The dotted regions indicate where axions could form the cosmic dark matter. Some experiments searching for galactic dark matter axions are also included in the figure [37].

A.4 Axion detection

The existence of visible axion, as mentioned before, was rejected due to the effects they would imply on the evolution of stars. As for the invisible axion P. Sikivie was the

first to propose experimental methods of detection; based on the Primakoff effect, axions would convert into photons, by using a strong magnetic field [50].

Microwave cavity experiments

This type of experiment uses electromagnetic cavities with a strong static magnetic field and by fine tuning the frequency of the cavity it is possible to convert resonantly axions of a given into photons [51]. Since this type of experiments searches for galactic halo axions, they are referred as haloscopes.

The first two experiments, Rochester-Brokhaven-Fermilab [52] and University of Florida [53], were able to exclude axions in the mass range $4.5\ \mu\text{eV/c}^2 < m_a < 16.3\ \mu\text{eV/c}^2$.

The following experiments ADMX [54] and LLNL [55], with a higher sensitivity, have manage to extend the search is the range $1.9\ \mu\text{eV/c}^2 < m_a < 3.3\ \mu\text{eV/c}^2$. Further improvements are expected by using superconducting quantum interference amplifiers for reducing noise.

A new experiment using Rydberg atoms, CARRACK2 [56] has been set up in Kyoto and intends to cover the region of $2\ \mu\text{eV/c}^2 < m_a < 30\ \mu\text{eV/c}^2$.

Telescope searches

The so called 'multi-eV' axions which are thermally produced can be searched with telescopes as they decay into two photons. By decaying these axions would produce an emission line. Observations done at Kitt Peak National Oservatory [49] of cluster galaxies have not shown the presence of this phenomenon, excluding de range $3\ \text{eV/c}^2 < m_a < 8\ \text{eV/c}^2$.

Radio Telescope searches done at Haystack Observatory [57], was able to rule out the expected decay of axion into photons at dwarf galaxies, in the range $298\ \mu\text{eV/c}^2 < m_a < 363\ \mu\text{eV/c}^2$.

Laser experiments

In this kind of pure laboratory searches based on the Primakoff effect, a high intensity light beam travels through a strong magnetic field, an expected beam of axions traverses a second magnetic field where detectable photons are reconverted. The regeneration type experiments of 'shining light through wall' [58] have excluded an important mass range $m_a < 10^{-3}\ \text{eV/c}^2$ for $g_{a\gamma} < 7.7 \times 10^{-9}\ \text{GeV}^{-1}$.

The same type of experiments put limits on the axion mass and coupling by assuming that the production of axions would induce changes in the polarization state of the photon beam, which would be observable by two effects: dichroism, the rotation of the polarization vector inside the first magnet and vacuum birefringence, inside the second magnet, where the beam is elliptically polarized. This type of experiment [59] has restricted for $m_a < 7 \times 10^{-4}$ eV/c^2 the coupling at $g_{a\gamma} < 2.5 \times 10^{-6}$ GeV^{-1}.

A recent experiment of this kind, PVLAS, observed a strong effect, which in the case of being interpreted as an axion like particle, would require a coupling constant around 3×10^{-6} GeV^{-1}, which has indeed been ruled out by other experiments such as CAST or the globular-cluster limit. Attempts to reconcile these results have followed [60].

A.5 Solar Axion searches

As discussed before, axions could be produced in the core of stars, thus providing an additional cooling mechanism. The Sun, our neighbouring star, has been object of study and has provided scientists important results by considering the Primakoff process.

When the Bragg condition is fulfilled [61][62], axions can interact coherently in the electric field close to the atomic nuclei of crystals. Two different groups have been looking at these effects using germanium detectors: $g_{a\gamma} < 2.7 \times 10^{-9}$ GeV^{-1} in SOLAX [63] and $g_{a\gamma} < 2.8 \times 10^{-9}$ GeV^{-1} in COSME [64].

The DAMA experiment [65] using crystals of NaI(Tl) achieved the limit of at $g_{a\gamma} < 1.7 \times 10^{-9}$ GeV^{-1}.

A second type of experiments called 'helioscopes' apply a transverse magnetic field to convert the incoming axions into detectable photons. The first experiment of this kind [66] explored two mass ranges setting the limits: $g_{a\gamma} < 3.6 \times 10^{-9}$ GeV^{-1} for $m_a <$ 0.03 eV/c^2 and $g_{a\gamma} < 7.7 \times 10^{-9}$ GeV^{-1} for 0.03 eV/c$^2 < m_a <$ 0.11 eV/c^2.

A more recent experiment of better sensitivity was performed in Tokyo [67] and has put the limits: $g_{a\gamma} < 6 \times 10^{-10}$ GeV^{-1} for $m_a <$ 0.03 eV/c^2 and $g_{a\gamma} < 6.8 - 10.9 \times 10^{-10}$ GeV^{-1} for $m_a <$ 0.3 eV/c^2.

The CAST experiment is looking into axions using the same principle and has set a remarkable improvement in the axion-to photon coupling for a broad band of masses.

Appendix B

Since we are dealing with a closed volume the number of moles of gas in the system remains constant, and it is given by the sum at its different locations:

$$n_t = \text{constant}\,, \text{ where } n_t = n_w + n_l + n_c\,. \tag{B.1}$$

Assuming that there is a fluctuation in temperature in the cold bore ΔT, the pressure in the system will have a consequent fluctuation Δp, although the amount of gas remains constant:

$$n_t = p\cdot\left(\frac{V_w}{R\cdot T_w}+\frac{V_l}{R\cdot T_l}+\frac{V_c}{R\cdot T_c}\right)=(p+\Delta p)\cdot\left(\frac{V_w}{R\cdot T_w}+\frac{V_l}{R\cdot T_l}+\frac{V_c}{R\cdot\left(T_c+\Delta T_c\right)}\right) \tag{B.2}$$

Here one can simplify the equation by:

$$p\cdot\left(\frac{V_c}{R\cdot T_c}\right)=\Delta p\cdot\left(\frac{V_w}{R\cdot T_w}+\frac{V_l}{R\cdot T_l}\right)+(p+\Delta p)\cdot\left(\frac{V_c}{R\cdot\left(T_c+\Delta T_c\right)}\right). \tag{B.3}$$

One can simplify one of the terms of the equation by eliminating the 2nd order terms on the series, as:

$$\frac{1}{T_c+\Delta T_c}\approx\frac{1}{T_c}\cdot\left(1-\frac{\Delta T_c}{T_c}+\frac{\Delta T_c^{\,2}}{T_c^{\,2}}+\ldots\right)\approx\frac{1}{T_c}\cdot\left(1-\frac{\Delta T_c}{T_c}\right). \tag{B.4}$$

And the equation (B.3) becomes

$$p\cdot\left(\frac{V_c}{R\cdot T_c}\right)=\Delta p\cdot\left(\frac{V_w}{R\cdot T_w}+\frac{V_l}{R\cdot T_l}\right)+(p+\Delta p)\cdot\left(\frac{V_c}{R\cdot T_c}\right)\cdot\left(1-\frac{\Delta T_c}{T_c}\right). \tag{B.5}$$

Rearranging the terms of the equation one gets:

$$\Delta p\cdot\left(\frac{V_w}{R\cdot T_w}+\frac{V_l}{R\cdot T_l}+\frac{V_c}{R\cdot T_c}\right)=p\cdot\left(\frac{V_c}{R\cdot T_c}\right)\cdot\left(\frac{\Delta T_c}{T_c}\right) \tag{B.6}$$

By dividing the equation by p and rearranging it comes:

$$\frac{\Delta p}{p}\cdot\left(n_w+n_l+n_c\right)=\frac{\Delta p}{p}\cdot\left(n_t\right)=n_c\cdot\frac{\Delta T_c}{T_c} \tag{B.7}$$

And finally, the relative pressure variation is:

$$\frac{\Delta p}{p} = \frac{n_c}{n_t} \cdot \frac{\Delta T_c}{T_c} \tag{B.8}$$

Now looking at the density variation in the cold bore due to a variation of temperature it comes:

$$\rho_c - \Delta\rho_c = \frac{(p + \Delta p) \cdot M}{R \cdot (T_c + \Delta T_c)} = \frac{p \cdot M}{R} \cdot \frac{\left(1 + \frac{n_c}{n_t} \cdot \frac{\Delta T_c}{T_c}\right)}{(T_c + \Delta T_c)} \tag{B.9}$$

Applying the same simplification derived in (A.4), one gets:

$$\begin{aligned} \rho_c - \Delta\rho_c &= \frac{p \cdot M}{R \cdot T_c} \cdot \left(1 + \frac{n_c}{n_t} \cdot \frac{\Delta T_c}{T_c}\right) \cdot \left(1 - \frac{\Delta T_c}{T_c}\right) = \\ &= \frac{p \cdot M}{R \cdot T_c} \cdot \left(1 + \frac{n_c}{n_t} \cdot \frac{\Delta T_c}{T_c} - \frac{\Delta T_c}{T_c}\right) \end{aligned} \tag{B.10}$$

And by making some simplifications:

$$\rho_c - \Delta\rho_c = \rho_c \cdot \left(1 + \frac{\Delta T_c}{T_c} \cdot \left(\frac{n_c}{n_t} - 1\right)\right). \tag{B.11}$$

Finally rearranging the terms: one gets:

$$\Delta\rho_c = \rho_c \cdot \left(1 - \frac{n_c}{n_t}\right) \frac{\Delta T_c}{T_c} = \rho_c \cdot \left(\frac{n_w + n_l}{n_t}\right) \frac{\Delta T_c}{T_c}. \tag{B.12}$$

And finally for the density variation as function of variation of temperature in the cold bore:

$$\frac{\Delta\rho_c}{\rho_c} = \left(\frac{n_w + n_l}{n_t}\right) \frac{\Delta T_c}{T_c}. \tag{B.13}$$

Bibliography

[1]. **K.Van Bibber, P.M. McIntyre, D.E.Morris, and G.G. Raffelt.** Design for a Practical Laboratory Detector for Solar Axions. *Phys. Rev. D. 39.* 2089, 1989.

[2]. **H.Primakoff.** *Photo-Production of Neutral Mesons in Nuclear Electric Fields and the Mean Life of Neutral Meson.* s.l. : Phys. Rev. 81 (1951)899.

[3]. **L. Di Lella, A. Pilaftsis, G. Raffelt and K. Zioutas.** *"Search for solar Kaluza-Klein axions in theories of low-scale quantum gravity".* s.l. : Phys. Rev. D 62 / 125011., (2000).

[4]. **J. N. Bahcall, W. F. Huebner, S. H. Lubow, P. D. Parker and R. K. Ulrich.** *"Standard SolarModels And The Uncertainties In Predicted Capture Rates Of Solar Neutrinos".* s.l. : Rev. Mod. Phys. 54 / 767., (1982).

[5]. **M. H. Pinsonneault and J. N. Bahcall.** *"What do we (not) know theoretically about solar neutrino fluxes?".* s.l. : Phys. Rev. Lett. 92 / 121301., (2004).

[6]. **K. Van Bibber, P. M. McIntyre, D. E. Morris, and G. G. Raffelt.** Design for a Practical Laboratory Detector for Solar Axions. *Phys. Rev. D 39, 2089.* 1989.

[7]. **P. Serpico and G. Raffelt.** *"New Calculation of Solar Axion Flux".* s.l. : CAST Internal Report, (2004).

[8]. **L. Stodolsky and G. Raffelt.** *"Mixing Of The Photon With Low Mass Particles".* s.l. : Phys. Rev. D 37 / 1237., (1988).

[9]. **S.Andriamonje et al (CAST Collaboration).** An improved limit on the axion-photon coupling from the CAST experiment. *JCAP07 04:010.* 2007.

[10]. **M. Bona et al.** *"Performance of the first CERN - INFN 10 m long superconducting dipole prototype for the LHC".* s.l. : CERN-AT-94-26-MA 4th European Particle Accelerator Conference (EPAC 94), London, England, (1994).

[11]. **D. Autiero et al.,** The CAST Time Projection Chamber. *Preprint Physics /0702190.* 2007.

[12]. **P. Abbon et al.,** The Micromegas detector of the CAST experiment. *Preprint Physics 0702190.* 2007.

[13]. **M.Kuster et al.,** The X-ray telescope of CAST. *Preprint Physics 0702188.* 2007.

[14]. **H. Egle, W. J. Altmann, J. Schwarz,.** *"ABRIXAS mirror system: mirror module testing and integration in the ABRIXAS satellite".* s.l. : in X-Ray Optics, Instruments and Missions II, R. B. Hoover and A. B. Walker eds", SPIE Conf. Proc. 3766 / 2, (1999).

[15]. **Standards, National Bureau of.** *"Compendium of the properties of materials at low temperature".* s.l. : Cryogenic Engineering Laboratory, (1960).

[16]. **A. Rott.** *Vacuum Technology.* s.l. : North Holland Publishing, 1982.

[17]. **T.Niinikoski et al.** *Thin cryogenic X-ray windows.* s.l. : ICEC22-ICMC2008 Proceedings, 2008.

[18]. **A. Devred.** *"Superconducting Development in Europe".* s.l. : Proceedings of the workshop on VLHC Magnets, FNAL, (2000).

[19]. **V. Helmholtz.** *"Verhandlungen des naturhistorisch-medizinischen Vereins zu Heindelberg".* (1863).

[20]. **G. Kirchoff.** *"Ueber Einflussder Warmeleitung in einem Gas auf die Schallbewegung".* s.l. : Ann. Phys., (1868).

[21]. **Lord J. W. Rayleigh.** *Theory of Sound 2nd ed.* (1944).

[22]. **H. Kramers.** *"Vibration of a gas column".* s.l. : Physica 15, (1949).

[23]. **N. Rott.** *"Damped and thermally driven acoustic oscillations in wide and narrow tubes".* s.l. : Z. Angew. Math. Phys., (1969).

[24]. **N. Rott.***"Thermally Driven acoustic oscillations, part II. Stability limit for helium".* s.l. : Z. Angew. Math. Phys., (1973).

[25]. **N. Rott.***"Thermoacoustics".* s.l. : Adv. in Applied Mechanics, Vol 20, (1980).

[26]. **T. Yasaki, A. Tominaga and Y. Narahara.** *"Experiments on thermally driven acoustic oscillations of gaseous helium".* s.l. : J. Low. Temp. Phys., (1980).

[27]. **T. Yasaki, S. Takashima, and F. Mizutani.** *"Complex Quasiperiodic and chaotic States Observed in Thermally Induced Oscillations in Gas Columns".* s.l. : Physics review Letters vol. 58, nr. 11, (1987).

[28]. **J. Casas, P. Gomes, K.N. Henrichsen, U. Jordung and M.A. Rodriguez Ruiz.** *Signal Conditioning for Cryogenic Thermometry in the LHC.* s.l. : Cryogenic Engineering and International Cryogenic Materials Conference (CEC-ICMC'99), 12-16 July 1999, Montreal, Canada, (1999).

[29]. **CAST Collaboration,** *Probing eV-scale axions with CAST.* arXiv:0810.4482v2 [hep-ex] 9 Jan 2009.

[30]. **N. Elias, T. Niinikoski, M. Davenport.** *Technical Design Report of the CAST 3-He Gas System.* s.l. : CERN Scientific Committee Paper, 2006.

[31]. **Ph. Gayet, R. Barillere.** *"UNICOS a framework to build industry like control systems".* s.l. : ICALEPCS'05.

[32]. **D. R. Peccei.** *"QCD, strong CP and axions".* s.l. : J. Korean Phys. Soc. 29, 1996.

[33]. **Rašin, R. N. Mohapatra and A.** Simple Supersymmetric Solution to the Strong CP Problem. *Phys. Rev. Lett. 76 3490.* 1996.

[34]. **H.Leutwyler, J. Gasser and.** Quark Masses. *Phys. Rep. 87 (1982) 77.* 1982.

[35]. **S. Eidelman et al., [Particle Data Group],.** *"Review of particle physics".* s.l. : Phys. Lett. B 592 / 1, (2004).

[36]. **H. Leutwyler.** *"The ratios of the light quark masses".* s.l. : Phys. Lett. B 378 / 313, (1996).

[37]. **G. Raffelt.** *" Stars as Laboratories for Fundamental Physics".* s.l. : Univesity of Chicago Press, (1996).

[38]. **H. R. Quinn and R. D. Peccei.** *"CP Conservation In The Presence Of Instantons".* s.l. : Phys. Rev. Lett. 38 \ 1440, 1977.

[39]. **S. Weinberg.** *"A New Light Boson?".* s.l. : Phys. Rev. Lett. 40 / 223, (1978).

[40]. **F. Wilczek.** *"Problem Of Strong P And T Invariance In The Presence Of Instantons".* s.l. : Phys. Rev. Lett. 40 / 279, (1978).

[41]. **J. E. Kim.** *"Light Pseudoscalars, Particle Physics And Cosmology".* s.l. : Phys. Rept. 150 / 1., (1987).

[42]. **J.E.Kim.** Weak interaction Singlet and CP Invariance. *Phys. Rev. Lett. 43 (1979) 103.*

[43]. **D. B. Kaplan.** *"Opening The Axion Window".* s.l. : Nucl. Phys. B 260 / 215., (1985).

[44]. **R. A. Zhitnitskiĭı.** *"On Possible Suppression of the Axion Hadron Interaction".* s.l. : Yad. Fiz. 31 / 497 [Sov. J. Nucl. Phys. 31 / 260], (1980).

[45]. **D. N. Spergel et al., [WMAP Collaboration].** *"First Year Wilkinson Microwave Anisotropy Probe (WMAP) Observations: Determination of Cosmological Parameters".* s.l. : Astrophys. J. Suppl. 148 / 175., (2003).

[46]. **E. P. S. Shellard and R. A. Battye.** *"Axion string constraints".* s.l. : Phys. Rev. Lett. 73 / 2954 [Erratum-ibid. 76 (1996) 2203]., (1994).

[47]. **D. Harari and P. Sikivie.** *"On The Evolution Of Global Strings In The Early Universe".* s.l. : Phys. Lett. B 195 / 361., (1987).

[48]. **C. Hagmann and P. Sikivie.** *"Computer Simulations Of The Motion And Decay Of Global Strings".* s.l. : Nucl. Phys. B 363 / 247., (1991).

[49]. **M. A. Bershady, T. Ressell and M. S. Turner.** *"Telescope Search For Multi-Ev Axions".* s.l. : Phys. Rev. Lett. 66 / 1398., (1991).

[50]. **P. Sikivie.** *"Experimental Tests Of The *Invisible* Axion".* s.l. : Phys. Rev. Lett. 51 / 1415 [Erratum-ibid. 52 (1984) 695]., (1983).

[51]. **R. Bradley et al.** *"Microwave cavity searches for dark-matter axions".* s.l. : Rev. Mod. Phys. 75 / 777., (2003).

[52]. **W. U. Wuensch et al.** *"Results Of A Laboratory Search For Cosmic Axions And Other Weakly Coupled Light Particles".* s.l. : Phys. Rev. D 40 / 3153., (1989).

[53]. **C. Hagmann, P. Sikivie, N. S. Sullivan and D. B. Tanner.** *"Results From A Search For Cosmic Axions".* s.l. : Phys. Rev. D 42 / 1297., (1990).

[54]. **C. Hagmann et al.** *"Results from a high-sensitivity search for cosmic axions".* s.l. : Phys. Rev. Lett. 80 / 2043., (1998).

[55]. **S. J. Asztalos et al.** *"An improved RF cavity search for halo axions".* s.l. : Phys. Rev. D 69 / 011101., (2004).

[56]. **M. Tada et al.** *"CARRACK II: A new large-scale experiment to search for axions with Rydberg-atom cavity detector".* s.l. : Nucl. Phys. Proc. Suppl. 72 / 164., (1999).

[57]. **B. D. Blout, E. J. Daw, M. P. Decowski, P. T. P. Ho, L. J. Rosenberg and D. B. Yu.** *"A radio telescope search for axions".* s.l. : Astrophys. J. 546 / 825., (2001).

[58]. **G.Ruoso et.al.,** Search for photon regeneration in a magnetic field. *Z. Phys. 56 (1992) 505.*

[59]. **Y. Semertzidis et al.** *"Limits On The Production Of Light Scalar And Pseudoscalar Particles".* s.l. : Phys. Rev. Lett. 64 / 2988., (1990).

[60]. **G.G.Raffelt.** Recent Searches and new limits. *[arXiv:hep-ph/0504152] (2005).*

[61]. **K. Zioutas and E. A. Paschos.** *"A Proposal for solar axion detection via Bragg scattering".* s.l. : Phys. Lett. B 323 / 367., (1994).

[62]. **R. J. Creswick, F. T. Avignone, H. A. Farach, J. I. Collar, A. O. Gattone, S. Nussinov and K. Zioutas.** *"Theory for the direct detection of solar axions by coherent Primakoff conversion in germanium detectors".* s.l. : Phys. Lett. B 427 / 235., (1998).

[63]. **F. T. Avignone et al. [SOLAX Collaboration].** *"Experimental search for solar axions via coherent Primakoff conversion in a germanium spectrometer".* s.l. : Phys. Rev. Lett. 81 / 5068., (1998).

[64]. **A. Morales et al. [COSME Collaboration].** *"Particle dark matter and solar axion searches with a small germanium detector at the Canfranc underground laboratory".* s.l. : Astropart. Phys. 16 / 325., (2002).

[65]. **R. Bernabei et al.** *"Search for solar axions by Primakoff effect in NaI crystals".* s.l. : Phys. Lett. B 515 / 6., (2001).

[66]. **D. M. Lazarus, G. C. Smith, R. Cameron, A. C. Melissinos, G. Ruoso, Y. K. Semertzidis and F. A. Nezrick.** *"A Search for solar axions",.* s.l. : Phys. Rev. Lett. 69 / 2333., (1992).

[67]. **S. Moriyama, M. Minowa, T. Namba, Y. Inoue, Y. Takasu and A. Yamamoto.** *"Direct search for solar axions by using strong magnetic field and X-ray detectors".* s.l. : Phys. Lett. B 434 / 147., (1998).